Fall 10-1-2021

Characterizing Photophysics of Photoconvertible-fluorescent Protein mEos3.2 for Quantitative Fluorescence Microscopy

Mengyuan Sun
Yale University Graduate School of Arts and Sciences, helensun930930@gmail.com

Abstract

Characterizing Photophysics of Photoconvertible Fluorescent Protein mEos3.2 for Quantitative Fluorescence Microscopy

Mengyuan (Helen) Sun

2021

Photoconvertible fluorescent proteins (PCFPs) are widely used in super-resolution microscopy, and studies of cellular dynamics. Their photoconversion properties have enabled single-molecule localization microscopy (SMLM) by temporally separating closely-spaced molecules. However, our understanding of their photophysics is still limited, hampering their quantitative application. For example, counting fluorescently-tagged fusion proteins from the discrete localizations of individual molecules is still difficult. The red-to-green photoconvertible fluorescent protein mEos3.2 is favored by many due to its monomeric property, high brightness, photostability, compatibility with live cells, and 1:1 labeling stoichiometry. The fluorescent protein mEos3.2 is fused to the coding sequence of a protein of interest in the genome for endogenous expression or expressed exogenously and transiently in cells. Irradiation at 405 nm photoconverts mEos3.2 molecules from their native green state with an emission peak at 516 nm to their red state with an emission peak at 580 nm. Sparsely distributed photoconverted red mEos3.2 are excited at 561 nm and then localized for SMLM imaging. Understanding the factors that affect mEos3.2 photophysics can greatly strengthen its applications in imaging and quantitative measurements. However, we still do not know

1) how the behavior of mEos3.2 in live cells compares with fixed cells, and how the imaging buffer influences mEos3.2 photophysics in fixed cells, 2) how different imaging methods and laser intensities affect the behavior of mEos3.2, and 3) if there are unknown dark states of mEos3.2 that can further complicate imaging and quantitative applications of mEos3.2.

In this body of work, I first reviewed the usage of photoconvertible fluorescent proteins in SMLM with a focus on its quantitative application. I discussed the significance, advantages, and challenges of counting molecules of interest tagged with mEos3.2 by SMLM. I highlighted how our limited understanding of mEos3.2 photophysics hampers its application in quantitative SMLM, thus requiring further investigation. Parts of this chapter are taken from Sun *et al.,* 2021.

In Chapter 2, I combined quantitative fluorescence microscopy and mathematical modeling to estimate the photophysical parameters of mEos3.2 in fission yeast cells. I measured the time-integrated fluorescence signal per cell, and rate constants for photoconversion and photobleaching by fitting a 3-state model of photoconversion and photobleaching to the time courses of the mEos3.2 fluorescence signal per cell measured by quantitative fluorescence microscopy. My method can be applied to study the photophysical properties of other photoactivatable fluorescent proteins and photoconvertible fluorescent proteins quantitatively, an approach complementary to conventional single-molecule experiments. This chapter is taken from Sun *et al.,* 2021.

In Chapter 3, I investigated how fixation affects the photophysical properties of mEos3.2, so that I could compare experiments conducted in live and fixed yeast cells with mEos3.2. Light fixation has been used to preserve cellular structures and eliminate movements of proteins to simplify the imaging and quantification process of quantitative SMLM. I discovered that formaldehyde fixation permeabilizes the *S. pombe* cells for small molecules, making the photophysical properties of mEos3.2 sensitive to the extracellular buffer conditions. To find conditions where the photophysical parameters of mEos3.2 are comparable in live and fixed yeast cells, I investigated how the pH and reducing agent in the imaging buffer affect the mEos3.2 photophysics in fixed cells. I discovered that using a buffer at pH 8.5 with 1 mM DTT to image mEos3.2 in fixed cells gave similar photophysical parameters to live cells. My results strongly suggested that formaldehyde fixation did not destroy mEos3.2 molecules but partially permeabilized the yeast cell membrane to small molecules. This chapter is taken from Sun *et al.,* 2021.

In Chapter 4, I investigated the effects of fixation and imaging buffer on mEos3.2 photophysics over a wide range of laser intensities by point-scanning and widefield microscopy, and also by SMLM. This chapter is taken from Sun *et al.,* 2021.

In Chapter 5, I alternated illumination at 405- and 561-nm to investigate the effects of 405- and 561-nm illumination separately. I discovered that 405-nm irradiation drove some of the red-state mEos3.2 molecules to enter an intermediate dark state, which can be converted back to the red fluorescent state by 561-nm illumination. I established the “positive” switching behavior (off-switching by 405-nm and on-switching by 561-nm illumination) of red mEos3.2 in addition to the previously reported “negative” switching

behavior (switching off by 561-nm and switching on by 405-nm illumination), which could potentially affect counting the number of localizations of red mEos3.2 by quantitative SMLM. This chapter is taken from Sun *et al.,* 2021.

In Chapter 6, I described my ongoing progress towards developing a method to count molecules with SMLM using internal standards tagged with mEos3.2. I summarized the preliminary data on the internal calibration standards that I have tried. Further work is needed to optimize the standards and test the robustness and the reproducibility of the standards. Ultimately, this work can be applied to count the number of molecules in diffraction-limited subcellular structures with SMLM by converting the number of localizations to the number of molecules.

Characterizing the Photophysics of Photoconvertible Fluorescent Protein mEos3.2 for Quantitative Fluorescence Microscopy

A Dissertation

Presented to the Faculty of the Graduate School

Of

Yale University

In Candidacy for the Degree of

Doctor of Philosophy

By

Mengyuan (Helen) Sun

Dissertation Directors: Thomas D. Pollard, Joerg Bewersdorf

December 2021

Table of Contents

List of Figures and Tables

List of Figures

List of Tables

List of Selected Publications

Sun, M., Hu, K., Bewersdorf, J., & Pollard, T. D. (2021). Sample preparation and imaging conditions affect mEos3.2 photophysics in fission yeast cells. *Biophysical Journal*, 120:21-34.

Bender, N., **Sun, M.,** Yılmaz, H., Bewersdorf, J., & Cao, H. (2021). Circumventing the optical diffraction limit with customized speckles. *Optica*, *8*(2), 122-129.

Acknowledgements

First and foremost, I want to express my sincerest gratitude to my PhD advisors and mentors, Dr. Thomas D. Pollard and Dr. Joerg Bewersdorf. With your mentorship and guidance, I have grown tremendously as an independent researcher and scientist. You have taught me how to conduct independent research, troubleshooting, planning experiments, presenting my work, and academic writing. Tom and Joerg have always been helpful and understanding when I encountered problems about my research and career development. I would like to thank my awesome lab mates in both the Pollard lab and the Bewersdorf lab for their help with my project. I want to specifically thank Sam Dundon and Steven Chou in the Pollard lab for helpful suggestions on troubleshooting biological problems. I also want to specifically thank Kevin Hu, Yongdeng Zhang, Zach Marin, Bennet Rollins, Michael Grace, and Andrew Barentine in the Bewersdorf lab for all the help regarding super-resolution imaging and data analysis. I next want to acknowledge my committee members, Dr. Megan King and Dr. Julien Berro, for their valuable suggestions, feedback, time, and investment in my project. I also want to thank my external reader Dr. Mike Heilemann for his suggestions, feedback, and time.

Next, I want to thank my friends, classmates, and colleagues that I have met during my time at Yale University through classes, seminars, and extra-curriculum activities. Many of you have inspired and helped me both professional and personally. I feel extremely lucky to have inspiring and nice friends and colleagues that makes living in a foreign country much easier and enjoyable.

Finally, I want to thank my parents and my boyfriend for their support. I want to thank my family for providing me with opportunities and resources for me to pursue higher education, and my boyfriend for providing me with support and encouragement through every milestone in graduate school. I am super grateful for having a loving family and significant other that are understanding and encouraging throughout graduate school.

Chapter 1: Introduction

1.1: Introduction to Single-molecule Localization Microscopy (SMLM)

1.1.1: Introduction to super-resolution fluorescence microscopy

Super-resolution fluorescence microscopy has revolutionized biomedical research by resolving diffraction limited sub-cellular structures and was awarded the Nobel Chemistry Prize in 2014 (Hell, 2015). Fluorescence microscopes have been widely used because of two major advantages: molecule-specific labeling, and compatibility with live cells (Huang, Bates, & Zhuang, 2009). Super-resolution microscopy improves the resolution of far-field lens-based fluorescence microscopes by circumventing the diffraction limit (~ 250 nm in the lateral direction and 500-700 nm in the axial direction) (Hell, 2007). There are two primary ways to achieve super-resolution (Baddeley & Bewersdorf, 2017): 1) using wave optics and image processing to sharpen the point-spread function, such as stimulated emission depletion (STED) microscopy (Hell & Wichmann, 1994; Klar & Hell, 1999), reversible saturable optically linear fluorescence transitions (RESOLFT) microscopy (Hell, Dyba, & Jakobs, 2004), and structured-illumination microscopy (SIM), and 2) turning fluorescent molecules on and off to localize individual single-molecules, such as stochastic optical reconstruction microscopy (STORM) (Rust, Bates, & Zhuang, 2006), photoactivated localization microscopy (PALM) (Betzig et al., 2006), and fluorescence photoactivation localization microscopy (FPALM) (Hess, Girirajan, & Mason, 2006). These methods have improved the spatial resolution by an order of magnitude in both the lateral and axial directions,

demonstrating great promise to resolve previously unresolved details of subcellular structures and cellular dynamics.

1.1.2: Working principle of single-molecule localization microscopy (SMLM)

Single molecule localization microscopy (SMLM) achieves super-resolution by switching fluorescent molecules that label the structure of interest “on” and “off” and localizing the centers of individual single molecules (Baddeley, Jayasinghe, Cremer, Cannell, & Soeller, 2009; Betzig et al., 2006; Folling et al., 2008; Heilemann et al., 2008; Hess et al., 2006; Lemmer et al., 2008; Rust et al., 2006). When imaging with conventional fluorescence microscopy, all the fluorophores emit simultaneously in a densely labeled structure. Each fluorescent molecule appears as a spot of ~ 250 nm in the lateral directions due to the diffraction limit of visible light. Molecules closer than ~ 250 nm apart cannot be distinguished from each other. By activating or switching “on” a small and random subset of fluorophores in a dense structure in each recorded image, the density of the fluorophores is low enough to isolate each individual molecule and to enable finding the center of the distribution of the recorded photons through computational postprocessing. Each center position is called a “localization”. To accumulate enough localizations to resolve the underlying dense structure, many frames are recorded until all the fluorophores have been stochastically switched “on”, imaged, and switched “off” (Fig 1.1). The “on” and “off” switching of the fluorescent molecules enables SMLM by keeping the density of visible molecules low in each recorded frame for localization. “On” switching can be achieved by actively turning on a random subset of fluorophores by light or passively waiting for the molecules that have

been reversibly switched to the “off” state previously to switch back to the “on” state. “Off” switching can be achieved by irreversible photobleaching of the fluorescent molecules or reversible switching the molecules to an invisible “off” state by light.

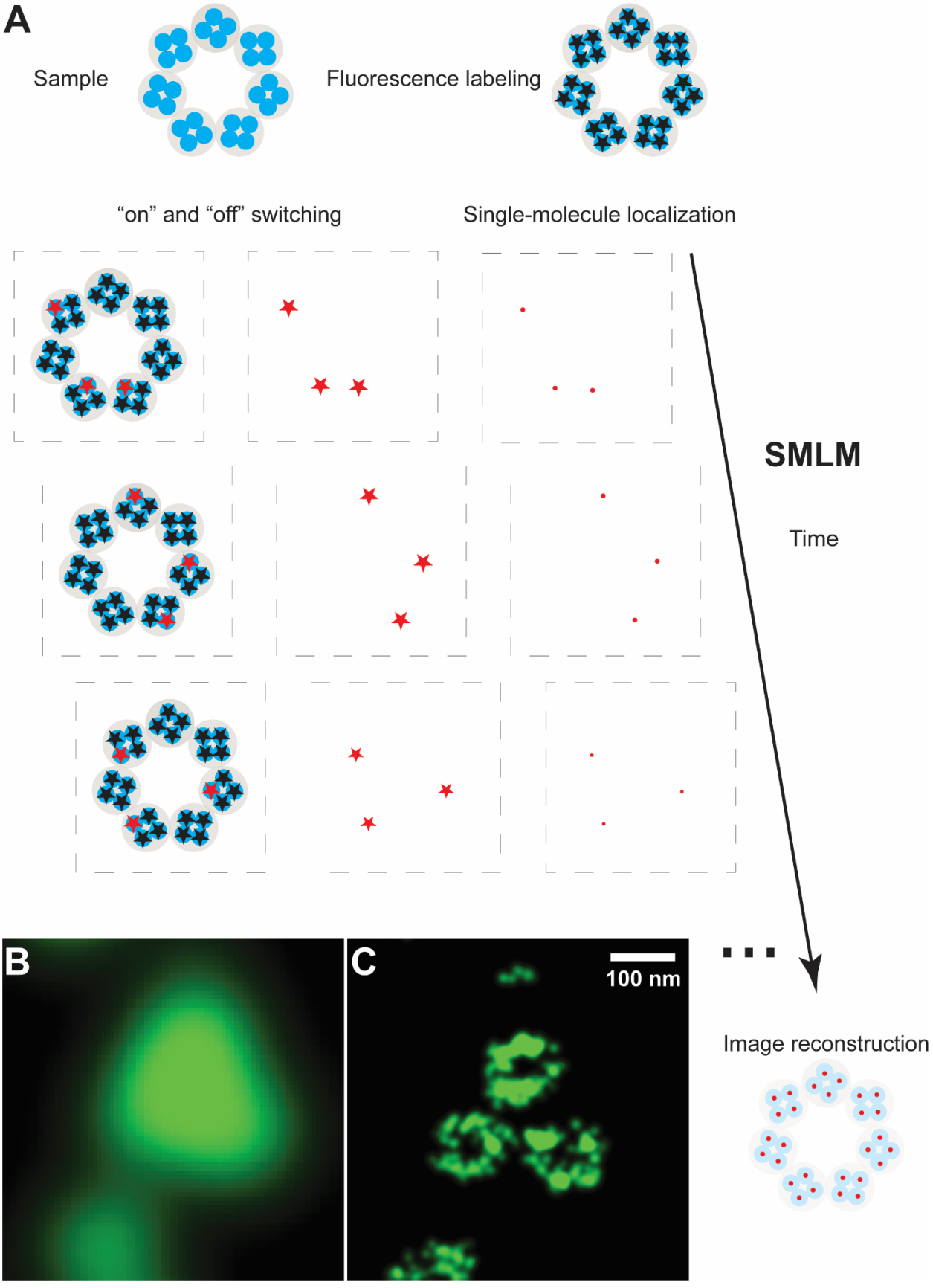
A
Sample
Fluorescence labeling
"on" and "off" switching
Single-molecule localization
SMLM
Time
B
C
100 nm
Image reconstruction

Figure 1.1: Single-molecule Localization Microscopy (SMLM)

(A) Single-molecule localization microscopy (SMLM) overcomes the diffraction limit by stochastically switching the single fluorescent molecules “on” and “off”, and then fitting the centers of images of individual fluorescent molecules. (B-C) Nuclear pore complex protein Nup107 labeled with SNAP-AF647 in fixed U2OS cells. Sample from Vilma Jimenez Sabinina at the European Molecular Biology Laboratory (EMBL) and imaged by Yongdeng Zhang in the Bewersdorf lab at Yale University. (B) Diffraction-limited image by confocal microscopy and (C) super-resolution image by 2D-SMLM.

1.1.3 The application of SMLM in biomedical research

The applications of SMLM in biomedical research has enabled visualization of previously invisible molecular details by light micrsocopy in biological systems. SMLM has been applied to answer questions involving the organization, interaction, stoichiometry, and dynamics of molecules of interest and how they integrate into the functional machinery in cells and tissues (Sigal, Zhou, & Zhuang, 2018). For example, the membrane-associated periodic skeleton of actin rings along the axon was discovered by SMLM in neurons (K. Xu, Zhong, & Zhuang, 2013). My laboratories have also investigated the molecular composition and organization of cytokinesis nodes in live fission yeast cells with SMLM (Akamatsu, Lin, Bewersdorf, & Pollard, 2017; Laplante, Huang, Tebbs, Bewersdorf, & Pollard, 2016).

1.2 Photoconvertible fluorescent protein mEos3.2

1.2.1 Photoconvertible or photoactivatable fluorescent proteins (PC or PAFPs)

Photoactivatable or photoconvertible fluorescent proteins (PAFPs or PCFPs) have enabled super-resolution imaging by temporally separating closely-spaced molecules (Betzig et al., 2006; Hess et al., 2006; Rust et al., 2006). PAFPs can be activated from a dark “off” state to a fluorescent “on” state (Fig. 1.2A), while PCFPs can be converted

from one color to another color (Fig. 1.2B) (Lippincott-Schwartz & Patterson, 2009; Karin Nienhaus & Nienhaus, 2014). The fluorescent protein is fused to the coding sequence of a protein of interest in the genome for endogenous expression or expressed exogenously and transiently through plasmids in cells. Although FPs are usually dimmer than organic dyes and therefore give lower localization precision and imaging resolution, they are favored by many due to their high labeling specificity, 1:1 labeling stoichiometry, and live-cell compatibility. PAFPs and PCFPs are highly appealing for imaging cellular dynamics in live cells and quantitative SMLM with endogenous tagging. Four properties of PAFPs and PCFPs affect SMLM imaging qualities: 1) photon counts per switching cycle, which affects the localization precision of each individual single-molecule, 2) the ratio of on- and off-switching cycles, which affects the achievable localization density, 3) tendency to dimerize or oligomerize, which could cause unwanted oligomerization of the targeted protein of interest, and 4) detection efficiency, the fraction of FPs that are folded properly and fluorescent in a cell (Wang, Moffitt, Dempsey, Xie, & Zhuang, 2014).

1.2.2 mEos3.2

The fluorescent protein EosFP (Wiedenmann et al., 2004) and its derivatives (McKinney, Murphy, Hazelwood, Davidson, & Looger, 2009; Paez-Segala et al., 2015; Wiedenmann et al., 2004; M. Zhang et al., 2012) have been widely used in single-molecule localization microscopy (SMLM) for both live (Akamatsu et al., 2017; Laplante et al., 2016; Y. Zhang, Lara-Tejero, Bewersdorf, & Galan, 2017) and fixed biological samples (Fricke, Beaudouin, Eils, & Heilemann, 2015; Puchner, Walter, Kasper, Huang,

& Lim, 2013; Shroff et al., 2007). EosFP was originally cloned from the scleractinian coral *Lobophyllia hemprichii* (Wiedenmann et al., 2004). Near-UV irradiation photoconverts EosFPs from their native green state with an emission peak at 516 nm to their red state with an emission peak at 581 nm (K. Nienhaus, Nienhaus, Wiedenmann, & Nar, 2005; Turkowyd et al., 2017; Wiedenmann et al., 2004). The photo-induced irreversible green-to-red conversion can be explained by the cleavage of the His-62-Nα-Cα bond, which creates the red chromophore in a ß-elimination reaction (Fig. 1.2C) (K. Nienhaus et al., 2005). In SMLM, sparsely distributed photoconverted red EosFPs are excited at 561 nm and then localized (Shroff et al., 2007). EosFP variants in both green and red states blink by entering one or more transient dark states and returning to the fluorescent state multiple times (Annibale, Vanni, Scarselli, Rothlisberger, & Radenovic, 2011; De Zitter et al., 2020; De Zitter et al., 2019; Endesfelder et al., 2011; Lee, Shin, Lee, & Bustamante, 2012; Thedie, Berardozzi, Adam, & Bourgeois, 2017).

EosFP is one of the best overall performing green-to-red PCFPs mainly due to its high photon output (Lippincott-Schwartz & Patterson, 2009). However, its inherent tetrameric nature has limited its application. Several monomeric forms, including mEos2, have been developed to overcome the tetrameric nature of EosFP (McKinney et al., 2009). However, monomeric mEos2 still forms oligomers at high concentration and forms aggregates when labeling membrane proteins, disrupting normal cellular function and dynamics (M. Zhang et al., 2012). Through x-ray crystallography, the key residues at the tetramerization interface by which mEos2 oligomerizes were identified and strategically mutated to generate an improved version, mEos3.2, which is truly monomeric, matures faster, has higher photon output and labeling density (Fig. 1.2C)

(M. Zhang et al., 2012). The rationally designed PCFP mEos3.2 is favored by many for both imaging and counting due to its monomeric property, fast maturation, high brightness, photostability, compatibility with live cells, and 1:1 labeling stoichiometry (Akamatsu et al., 2017; Laplante et al., 2016; M. Zhang et al., 2012; Y. Zhang, Lara-Tejero, et al., 2017).

A) Photoactivatable fluorescent protein (PAFP)

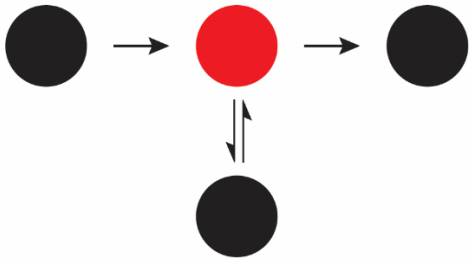

B) Photoconvertible fluorescent protein (PCFP)

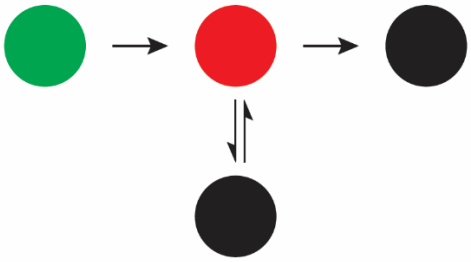

C) Crystal structure of PCFP mEos2

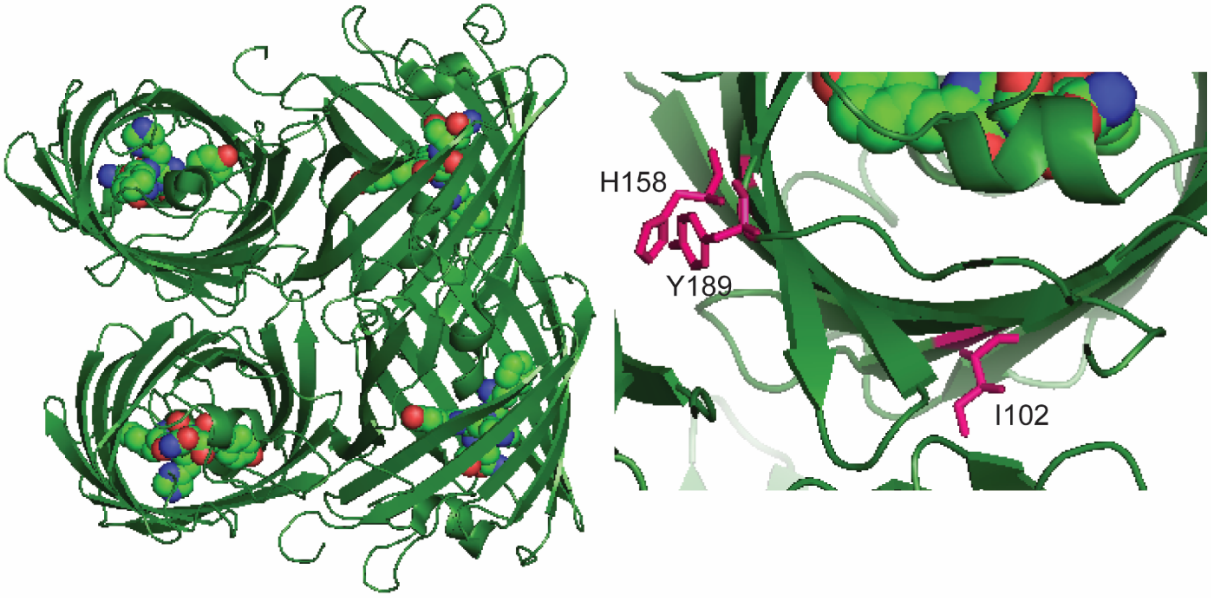

D) Green-to-red conversion of PCFP EosFP

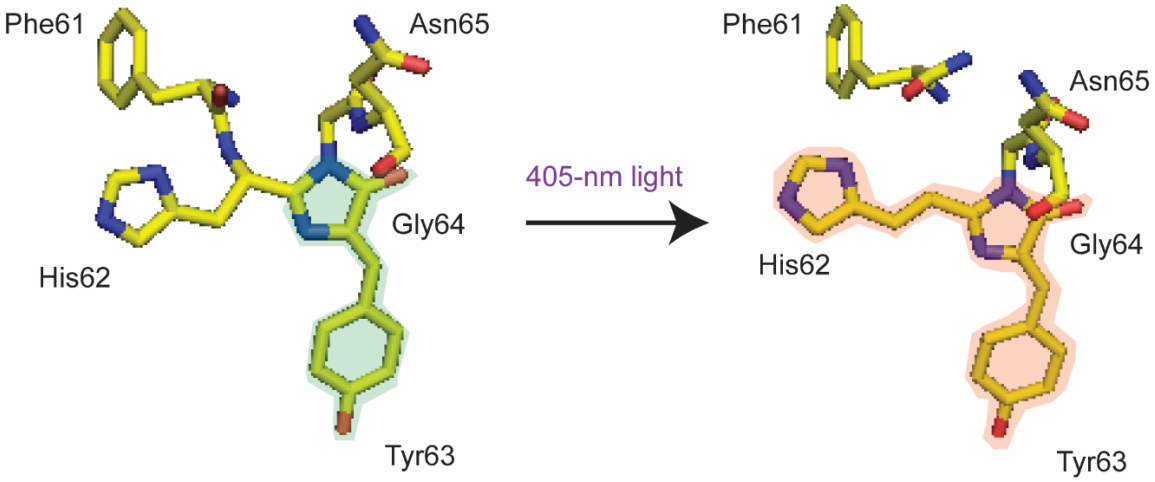

Figure 1.2: Photoconvertible or photoactivatable fluorescent protein (PC or PAFP)

(A-B) PAFPs can be activated from a dark "off" state to a fluorescent "on" state, while PCFPs are converted from one color to another color. The photoactivation or photoconversion enables the temporal separation of closely-spaced molecules for SMLM imaging. (C) Overall structure of green form PCFP mEos2. Four mEos2 protomers constitute tetrameric mEos2. Chromophore residues are highlighted with atom structures. True monomeric PCFP mEos3.2 have 3 mutations I102N, H158E, Y189A relative to the mEos2 sequence to disrupt the formation of tetramers. The three residues are labeled with stick model in magenta. (PDB ID: 3s05 (M. Zhang et al., 2012)). (D) EosFP photoconverts from the green form to the red form through the cleavage of the His-62-Nα-Cα bond. The photo-induced cleavage extends the green chromophore (PDB ID: 2btj) to form the red chromophore (PDB ID: 1zux) in a ß-elimination reaction (K. Nienhaus et al., 2005).

1.3 Quantitative application of mEos3.2 in SMLM

Understanding the factors that affect mEos3.2 photophysics strengthens its quantitative application. For example, counting fluorescently-tagged fusion proteins is a potential strength of SMLM, as the images are assembled from discrete localizations of individual molecules (Baddeley & Bewersdorf, 2017; Coffman & Wu, 2012). The total number of localizations in the SMLM images encodes the information of the total number of target molecules, which allows the measurement of important quantities in a diffraction-limited subcellular structure. Genetically encoded tagging with PCFPs or PAFPs can ensure 1:1 labeling stoichiometry, without further introducing labeling uncertainties as when using extrinsic labeling techniques (Ehmann et al., 2014; Jungmann et al., 2016; Los et al., 2005; Nieuwenhuizen et al., 2015; Stagge, Mitronova, Belov, Wurm, & Jakobs, 2013).

However, even with genetically encoded tagging, quantitative SMLM still faces several challenges that could lead to undercounting or overcounting of the molecule numbers (Fig. 1.3). Fluorescent proteins take time to mature, so an unknown fraction of the FPs is fluorescent at the time of imaging (Fig. 1.3C) (Wang et al., 2014). Some of the PA or

PCFPs might never be photoconverted or photoactivated to the active state for SMLM imaging (Durisic, Laparra-Cuervo, Sandoval-Alvarez, Borbely, & Lakadamyali, 2014). Slow maturation and incomplete photoconversion or photoactivation can lead to undercounting without proper calibration. Moreover, activated PA or PCFPs can go into a transient dark state and come back to the fluorescent state an unknown number of times (Fig. 1.3B) (Annibale et al., 2011; Lee et al., 2012; Rollins, Shin, Bustamante, & Presse, 2015), which can lead to an overcounting problem.

Several attempts have been made to correct for the overcounting problem for quantitative SMLM. Pair correlation analysis probes the distribution of points around a central point, providing insight on the organization and clustering of membrane proteins (Sengupta et al., 2011). Fourier Ring correlation analysis uses the spurious correlation between the two halves of the same imaging data to correct for the repeated photoactivations of the same fluorophore and was applied to quantify an antibody-labeled biological specimen with correction for labelling stoichiometry and photobleaching (Nieuwenhuizen et al., 2015; Nieuwenhuizen et al., 2013). The temporal threshold method groups emission bursts together through parameters calculated from a photokinetic model of the PCFP (Annibale et al., 2011; Lee et al., 2012; Rollins et al., 2015). However, none of the above methods have taken the slow maturation problem into account.

Internal calibration standards of known number of fluorescent proteins (Fricke et al., 2015; Hummer, Fricke, & Heilemann, 2016; Karathanasis et al., 2020; Puchner et al., 2013; Y. Zhang, Lara-Tejero, et al., 2017) have the potential to correct for the above

undercounting and overcounting problems. The target and calibration standards must be prepared, imaged, and analyzed in the same way (Coffman & Wu, 2012; Fricke et al., 2015; Puchner et al., 2013; Wu & Pollard, 2005). Diffusion and other movements of the fluorescent protein can complicate the imaging and quantification processes, so light chemical fixation has been used to preserve cellular structures and eliminate movements of proteins tagged with mEos2 (Fricke et al., 2015; Puchner et al., 2013). However, fixation can potentially introduce errors in the quantification process. Fixation might destroy some of the fluorescent proteins or change their photophysical properties (Ganguly, Clayton, & Chattopadhyay, 2011), which can change the average number of localizations for an individual FP. Moreover, the inconsistency in the fixation process, such as varying duration of fixation, can potentially introduce errors.

Therefore, one must understand how fixation and sample preparation affect the mEos3.2 photophysical parameters essential for its quantitative application. Photoconversion and photobleaching rates determine the density of active fluorophores in each frame for SMLM imaging, which is essential for separating closely-spaced molecules. The fluorescence signal of fluorescence fusion proteins in the structure of interest contains information about the brightness of individual molecules and the number of molecules able to fluoresce in the red channel, both aspects being important for quantification with diffraction-limited (Wu & Pollard, 2005) and super-resolution imaging (Baddeley & Bewersdorf, 2017).

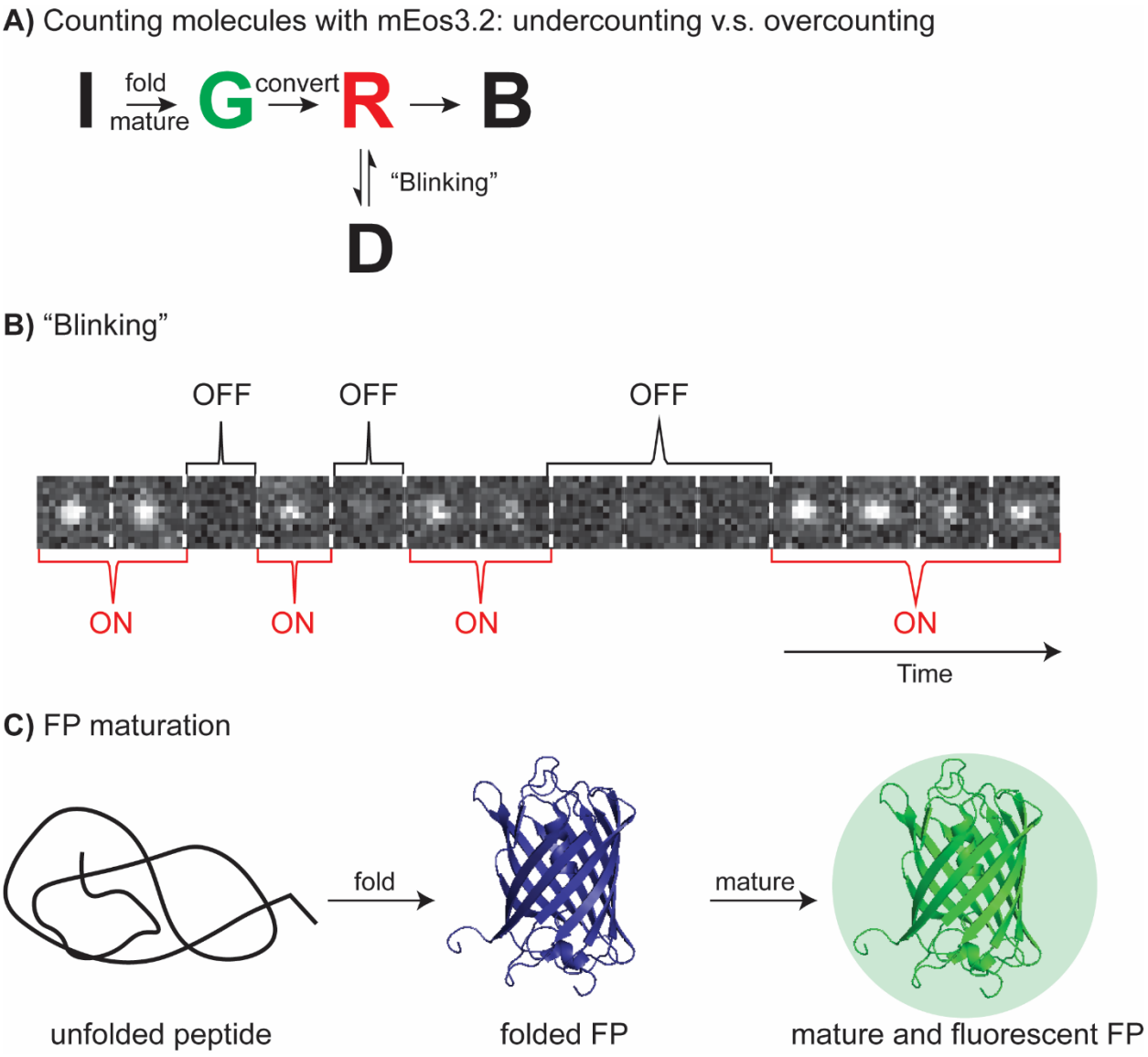

Figure 1.3: Undercounting and overcounting problems of quantitative SMLM with mEos3.2

(A) Newly expressed mEos3.2 peptide (**I**) takes time to fold and mature. The mature and fluorescent non-active green state of mEos3.2 (**G**) is irreversibly photoconverted into the red fluorescent form (**R**). The R-state mEos3.2 reversibly enters the transient dark state (**D**) and comes back to the R-state until bleached (**B**). (B) Fluorescence micrographs of a single purified red-state mEos3.2 molecule on the coverslip (10 ms per frame). Each box here is a frame. The R-state mEos3.2 shows three transitions into the dark state until bleached. (C) Fluorescent proteins take time to fold and mature. At any given time in a cell, an unknown fraction of the FPs is not properly folded and matured to be fluorescent and detectable.

1.4 Thesis objective

Photoconvertible fluorescent proteins (PCFPs) are widely used in super-resolution microscopy and studies of cellular dynamics. However, our understanding of their photophysics is still limited, hampering their quantitative application. For example, we do not know the optimal sample preparation methods or imaging conditions to count protein molecules fused to PCFPs by single-molecule localization microscopy in live and fixed cells. We also do not know how the behavior of PCFPs in live cells compares with fixed cells. Understanding the factors that affect mEos3.2 photophysics can greatly strengthen its quantitative application. Therefore, in Chapter 2, I measured the photophysical properties of mEos3.2 in fission yeast cells by fitting a 3-state model of photoconversion and photobleaching to the time course of the mEos3.2 fluorescence signal per cell measured by quantitative fluorescence microscopy. In Chapter 3, I found that formaldehyde fixation permeabilized the *S. pombe* cells to small molecules, making the photophysical properties of mEos3.2 sensitive to the extracellular buffer conditions. In Chapter 4, we investigated the effects of fixation and imaging buffer under a wide range of imaging conditions with point-scanning and widefield illumination to find conditions where the mEos3.2 photophysical parameters are comparable in live and fixed yeast cells. In Chapter 5, I also discovered that a subpopulation of red-state mEos3.2 molecules entered an intermediate state under 405-nm irradiation that is converted back to the red fluorescent state by illumination at 561-nm but not 405-nm. My data provide information on sample preparation for imaging and counting mEos3.2 in live and fixed yeast cells. My quantitative imaging assay combined with the 3-state model can be applied to study the photophysical properties of other PAFPs and PCFPs

quantitatively complementary to single-molecule experiments. Chapter 2, 3, 4, and 5 are taken from Sun *et al.*, 2021. In Chapter 6, I further summarized the preliminary data I have on using internal calibration standards to convert the number of localizations to the number of molecules in subcellular structures by SMLM and discussed the future directions.

Chapter 2: Quantitative characterization of mEos3.2 photophysics

2.1 Quantitative fluorescence microscopy

2.1.1 Plasmids and *S. pombe* strains

I cloned the open reading frame encoding mEos3.2 into the pJK148-pAct1-nmt1Term plasmid with PCR and NEB HiFi Builder Assembly. Both the newly constructed plasmid and chromosomal insertion were verified by sequencing.

2.1.2 Preparation of live *S. pombe* cells for imaging

S. pombe cells expressing mEos3.2 were grown in exponential phase at 25 °C in YE5S-rich liquid medium in 50-mL flasks in the dark before switching to EMM5S-synthetic medium ~12-18 hours before imaging to reduce the cellular autofluorescence background. Live cells were concentrated 10- to 20-fold by centrifugation at 3,000 rpm for 30 s and resuspended in EMM5S for imaging. Concentrated live cells in 2 µL were mounted on a thin layer formed from 35 µL of 25% gelatin (G-2500; Sigma-Aldrich, St. Louis, MO) in EMM5S.

2.2.2 Point-scanning confocal imaging conditions

Time lapse videos were acquired on a Zeiss Laser Scanning Microscope (LSM 880) using an alphaPlan-Apochromat 100x/NA 1.46 oil-immersion objective and an emission band path filter collecting fluorescence in the 566 - 719 nm wavelength range. Samples were illuminated by scanning a field of view (FOV) of 85 x 85 µm (512 x 512 pixels; 160 nm pixel size) with both the 405 nm (~22 µW at the sample) and 561 nm (~16 µW at the sample) lasers at constant intensities. A Z-stack of 19 slices spaced at 600-nm intervals

was acquired with a pixel dwell time of 0.85 µs. The total exposure time for each Z-stack was 4.23 s (0.85 µs x 512 x 512 x 19). An entire time lapse data set consisted of 50 or 100 Z-stacks at an acquisition rate of approximately 4 Z-stacks per minute (due to overhead in the scan process).

2.2.3 Image analysis

I viewed and analyzed images recorded by confocal microscope in Fiji (Fiji is Just ImageJ) (Schindelin et al., 2012). I made a sum projection of the 19-slice Z-stacks of the time-lapse confocal images. I manually selected a region of interest (ROI) 1 (containing typically ~50-100 cells for the confocal images) with the polygon tool and selected the background ROI 2 with the square tool (Fig. 2.1). The area and mean signal per pixel (MSPP) of both ROIs were measured and the fluorescence signal per cell at each time point was calculated based on: [Area 1 * (MSPP 1 –MSPP 2)] / number of cells in ROI 1. I calculated the weighted mean and standard deviation of the fluorescence signal per cell from all the FOVs included for each condition, weighted by the number of cells in each FOV. To correct for autofluorescence background, I subtracted the autofluorescence signal per wildtype cell at each time point from the fluorescence signal per cell expressing mEos3.2.

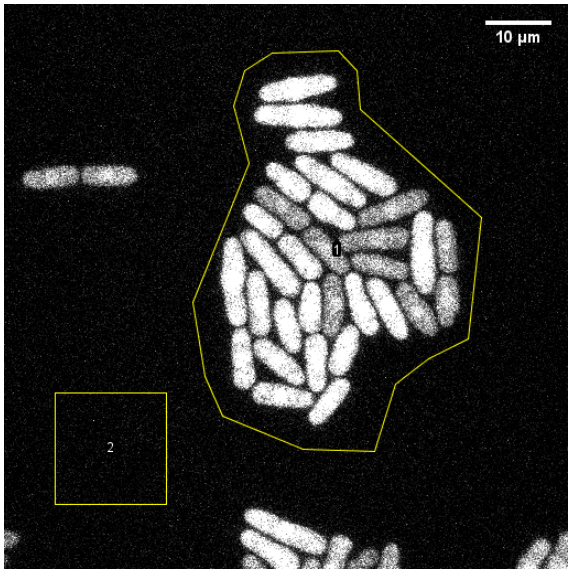

Figure 2.1: Measurement of mEos3.2 fluorescence signal per cell by quantitative fluorescence microscopy and analysis with Fiji.

Fluorescence micrograph of a field of *S. pombe* cells expressing cytoplasmic mEos3.2 at the 31st time cycles as in Fig. 1. Region of Interest (ROI) 1 containing cells was manually selected with a polygon tool, and ROI 2 was manually selected with a square tool for background subtraction. Scale bar = 10 µm.

2.2 Three-state mathematical model

My three-state model considers mEos3.2 molecules to have 3 different states: a non-activated green (G) state, an activated red (R) state, and a bleached (B) state. Photoconversion converts molecules from the G- to the R-state by an irreversible first-order reaction with a rate constant of k_{act} ($k_{activation}$). Molecules in the R-state emit red photons until they are photobleached to the B state by an irreversible first-order reaction with a rate constant of k_{bl} ($k_{bleaching}$). With illumination at 405 nm and 561 nm, the rates of change in the numbers (n) of G-, R-, and B-state mEos3.2 molecules are described by the following differential equations (Fig. 2.2):

$$\frac{dG_n(t)}{dt} = -k_{act}G_n(t) \qquad (1.1)$$

$$\frac{dR_n(t)}{dt} = k_{act}G_n(t) - k_{bl}R_n(t) \qquad (1.2)$$

$$\frac{dB_n(t)}{dt} = k_{bl}R_n(t) \qquad (1.3)$$

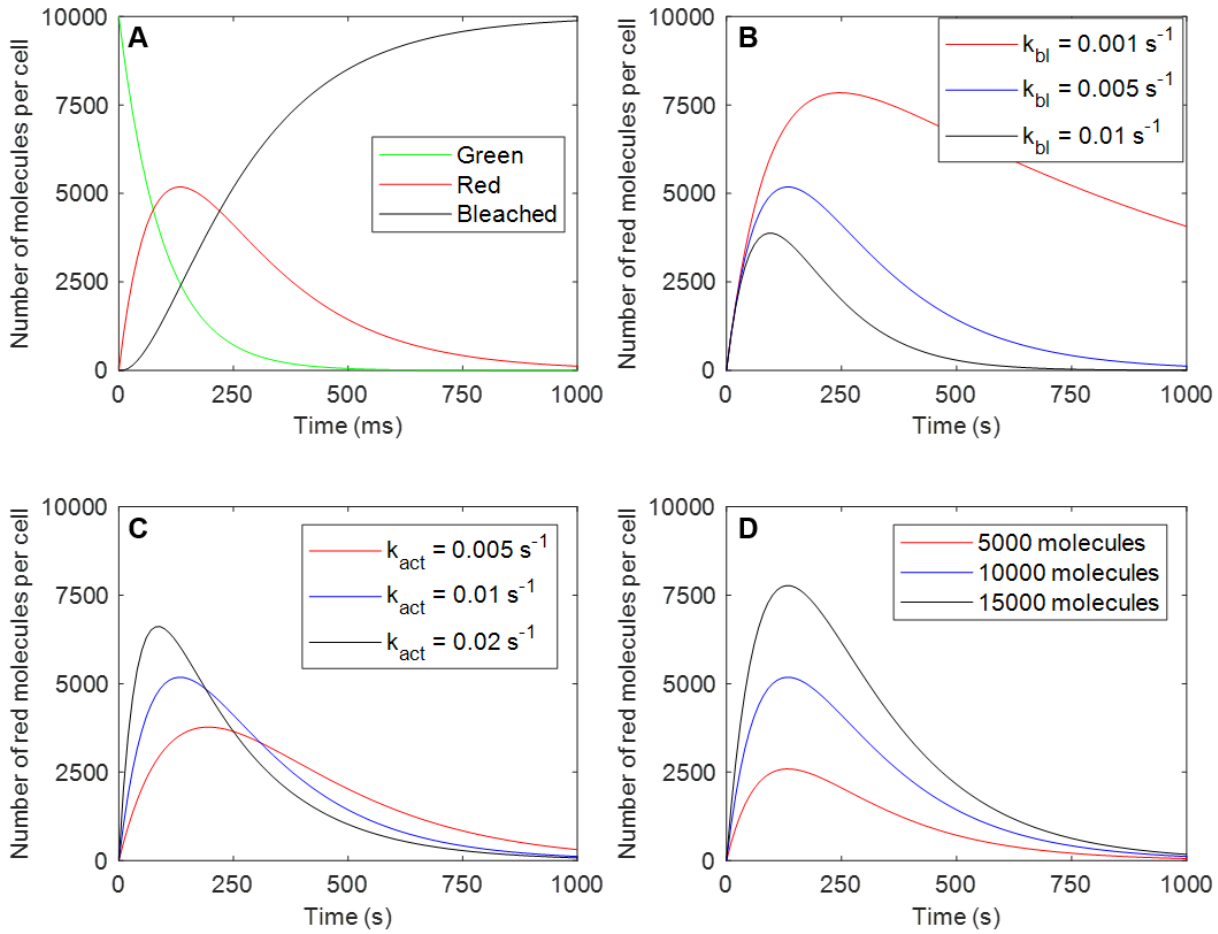

Figure 2.2: Simulations of the numbers of green, red, and bleached mEos3.2 molecules per cell over time.

(A) Evolution of the number of the green, red, and bleached mEos3.2 molecules. Conditions: 10,000 total molecules per cell, photoconversion rate constant k_{act} = 0.01 s^{-1}, photobleaching rate constant k_{bl} = 0.005 s^{-1}. (B) Vary the photobleaching rate constant. Conditions: 10,000 total molecules per cell, k_{act} = 0.01 s^{-1}. (C) Vary the photoconversion rate constant. Conditions: 10,000 total molecules, k_{bl} = 0.005 s^{-1}. (D) Vary the total number of molecules per cell. Conditions: k_{act} = 0.01 s^{-1}, k_{bl} = 0.005 s^{-1}.

I defined the total number of mEos3.2 molecules in a cell able to fluoresce in the red channel as M_n, and assumed that all mEos3.2 molecules were in the green state at the

start of the experiment, so $G_n(t = 0) = M_n$, $R_n(t = 0) = 0$, and $B_n(t = 0) = 0$. Solving the system of differential equations analytically resulted in the following equations for the number of G-, R-, and B-state molecules in a cell changing over time:

$$G_n(t) = M_n e^{-k_{act}t} \qquad (1.4)$$

$$R_n(t) = \frac{M_n k_{act}}{k_{bl} - k_{act}} (e^{-k_{act}t} - e^{-k_{bl}t}) \qquad (1.5)$$

$$B_n(t) = \frac{M_n}{k_{bl} - k_{act}} [k_{bl}(1 - e^{-k_{act}t}) - k_{act}(1 - e^{-k_{bl}t})] \qquad (1.6)$$

Eq. 1.5 describes how the number of R-state mEos3.2 molecules in a cell (R_n) changes with continuous photoconversion and photobleaching. Assuming that the signal of an R-state molecule per frame is ε_f, the fluorescence signal from the red mEos3.2 molecules per cell (R_s) at each frame recorded at a given time t is $R_s(t) = R_n(t) \times \varepsilon_f$. Multiplying both sides of Eq. 1.5 by ε_f gives Eq. 1.7 that describes how the fluorescence signal per cell in each frame $R_s(t)$ changes over time with continuous photoconversion and photobleaching:

$$R_s(t) = \frac{M_n \varepsilon_f k_{act}}{k_{bl} - k_{act}} (e^{-k_{act}t} - e^{-k_{bl}t}) \qquad (1.7)$$

I estimated $M_n \times \varepsilon_f$, k_{act}, and k_{bl} using Levenberg-Marquardt nonlinear least squares regression to fit Eq. 1.7 to the time course of fluorescence signal per cell $R_s(t)$. I calculated the 95% confidence intervals (CI) of the fitted parameters from the covariance argument of the fit. For the confocal experiments, I fit Eq. 1.7 to the weighted average time course of fluorescence signal per cell from all FOVs and report the 95% CI of the fitted parameters.

Since $R_s(t)$ is the fluorescence signal from red mEos3.2 molecules per cell in each frame, the fluorescence signal from red mEos3.2 molecules per cell per second is $R_s(t)$ x f (frame rate, fps). Integrating the function $R_s(t)$ x f with respect to time (t, second) over the interval of [0, ∞] gives the time-integrated signal $\overline{R_s}$ of mEos3.2 per cell:

$$\overline{R_s} = \int_0^\infty [f \cdot R_s(t)]dt = \int_0^\infty \frac{fM_n\varepsilon_f k_{act}}{k_{bl}-k_{act}}(e^{-k_{act}t} - e^{-k_{bl}t})dt = \frac{fM_n\varepsilon_f}{k_{bl}} \qquad (1.8)$$

I used Eq. 1.8 to calculate $\overline{R_s}$ using the parameters M_n x ε_f and k_{bl} from the previous fit of Eq. 1.7. I estimated the 95% CI or standard deviation through error propagation.

2.3 Quantitative Assessment of mEos3.2 photophysics in yeast cells by fitting a 3-state model to fluorescence microscopy data

I combined quantitative fluorescence microscopy with mathematical modeling to estimate the time-integrated signal per cell detected in the red channel ($\overline{R_s}$), and the rate constants for photoconversion and photobleaching (k_{act} and k_{bl}) of mEos3.2 in the cytoplasm of fission yeast cells (Fig. 2.3). The 3-state model assumes that illumination at 405 nm photoconverts mEos3.2 molecules irreversibly from their green (G) to their red (R) state with an activation rate constant of k_{act} and that the 561-nm illumination excites the red-state mEos3.2 with a peak emission at ~580 nm. Illumination at either 405 nm or 561 nm converts R-state mEos3.2 molecules to the bleached (B) state by an irreversible first-order reaction with a bleaching rate constant of k_{bl} (Fig. 2.3C). The 3-state model did not consider mEos3.2 photoswitching or “blinking” in its G- or R-state, where the protein enters one or multiple transient dark states and can be converted back to the fluorescent state multiple times. My model also did not consider

photobleaching from the G-state, as those molecules would not be detected in the red channel.

Fission yeast cells expressing mEos3.2 from the actin promoter in the *leu1* locus ensured a relatively high and homogenous mEos3.2 expression level in the cytoplasm (Fig. 2.3A). I used point-scanning confocal microscopy to illuminate the cells at both 405 nm and 561 nm and collected time-lapse images in the red wavelength range of 566-719 nm (Fig. 2.3A). The time course of the fluorescence signal per cell first rose as the large pool of molecules in the G-state was photoconverted to the R-state, from which I detected red photons as signal, and then declined as the pool of molecules in the G-state was depleted by photoconversion and the pool of molecules in the R-state was depleted by photobleaching (Fig. 2.3B). Simulations of the 3-state model showed how the values of the three parameters influenced the time courses of the number of R-state molecules per cell (Fig. 2.2B, C, D).

The equation (Eq. 1.7) of the 3-state model (Fig. 2.3C) fit the time course of fluorescence signal per cell very closely (Fig. 2.3B). The best fit yielded estimates of the product of total number of molecules able to fluoresce in the red channel per cell and detected signal per R-state molecule per frame (M_n x ε_f), and the rate constants for photoconversion (k_{act}) and photobleaching (k_{bl}) (shown in legend of Fig. 2.3B). I then used Eq. 1.8 to calculate the time-integrated signal per cell ($\overline{R_s}$) using fitted parameters M_n x ε_f and k_{bl}. I used this approach to measure how sample preparation and imaging conditions influence these photophysical properties as described in the subsequent chapters.

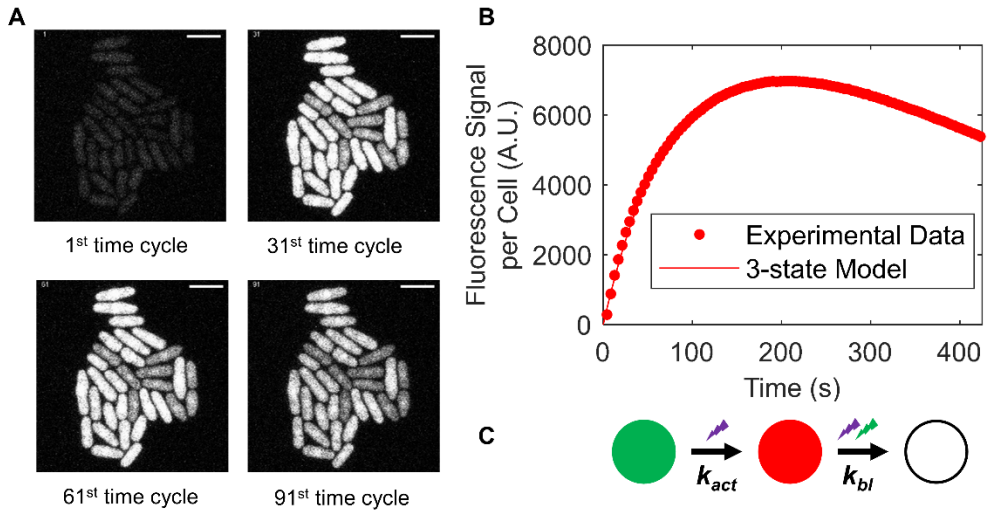

Figure 2.3: Photoconversion and photobleaching of mEos3.2.

(A) Time series of fluorescence micrographs of a field *of S. pombe* cells expressing cytoplasmic mEos3.2 at the 1st, 31st, 61st, and 91st time cycles. At each of the 100 cycles, a point-scanning confocal microscope illuminated the cells simultaneously at both 405 nm and 561 nm, 19-slices in a Z stack were imaged with a total exposure time of 4.23 s and sum-projected with the same contrast. Scale bar = 10 μm. (B) Time course of the fluorescence signal per cell at 566-719 nm (after autofluorescence subtraction). Fitting Eq. 1.7 of the 3-state model in panel C (line) to the data (dots) gave a photoconversion rate constant (k_{act}) of 1.2 x 10^{-2} s^{-1} (95% CI: 1.16 -1.24 x 10^{-2}) and a photobleaching rate constant (k_{bl}) of 1.6 x 10^{-3} s^{-1} (95% CI: 1.5-1.7 x10^{-3}). (C) Three state model for mEos3.2 photoconversion and bleaching. Illumination at 405 nm photoconverts mature mEos3.2 molecules from the green (G) state to the red (R) state with a photoconversion rate constant of k_{act}. Illumination at both wavelengths photobleaches red mEos3.2 molecules with a rate constant of k_{bl}.

2.4 The advantages and limitations of my approach

My approach complements *in vitro* single-molecule characterization of fluorophores (Lee et al., 2012; Y. Lin et al., 2015; Zanacchi et al., 2017) and has several advantages. (1) It avoids potential artifacts caused by using arbitrary photon number or localization uncertainty thresholds in single-molecule localization algorithms to separate molecules from noise. (2) It is easy to implement with conventional microscopes and whole cells. (3) Large numbers of cells can be imaged in just hours to test different sample preparation and imaging conditions, including a wide range of laser intensities. (4) It

extracts photoconversion or photoactivation rate constants from PAFPs or PCFPs in cells more easily than single-molecule methods, as photobleaching is hard to account for in single-molecule data (Durisic et al., 2014). These rate constants are useful for optimizing SMLM imaging conditions and simulating raw SMLM data.

On the other hand, given the complexity of mEos3.2 photophysics under SMLM conditions, my approach cannot replace the single-molecule measurements of the blinking kinetics of mEos variants in either their green (De Zitter et al., 2020; Thedie et al., 2017) or red states (De Zitter et al., 2019; Endesfelder et al., 2011). Blinking in the green state of mEos variants could affect photoconversion to the red state (De Zitter et al., 2020; Thedie et al., 2017). Interplay between blinking and photoconversion also affects other photoconvertible fluorescent proteins, such as SAASoti (Solovyev, Gavshina, & Savitsky, 2019) and LEA (Krueger et al., 2020). Photobleaching from the green state could decrease the number of detected red-state mEos3.2 (Thedie et al., 2017). Thus, combining my approach with single-molecule measurements will offer a more complete and quantitative understanding of the photophysics of PAFPs or PCFPs.

Chapter 3: Sample preparation affects mEos3.2 photophysics

I used the approach described in Chapter 2 to quantitatively test how sample preparation, including formaldehyde fixation and imaging buffer, affects mEos3.2 photophysics in fission yeast *S. pombe* cells.

3.1 Fixation affects mEos3.2 photophysics

I investigated how fixation affects the photophysical properties of mEos3.2 to allow us to compare experiments on live and fixed yeast cells (Fig. 3.1).

Live cells were prepared the same way as described in Chapter 2.1.1. Cells were fixed by mixing an equal volume of fresh, room temperature 4% formaldehyde aqueous solution (Electron Microscopy Sciences, Hatfield, PA) with the cell culture and shaking at 150 rpm at 25° C for 15 min or 30 min. The cells were pelleted by centrifugation at 3,000 rpm for 30 s and washed by pelleting in EMM5S 3 times, and then resuspended in EMM5S. Concentrated cells in 5 µL were mounted on a thin layer formed from 35 µL of 25% gelatin (Sigma-Aldrich; G-2500) in EMM5S. Both live cells and fixed cells were imaged as described in Chapter 2.2.2. The fluorescence micrographs were analyzed as described in Chapter 2.2.3.

Yeast cells fixed with formaldehyde in EMM5S-synthetic growth medium emitted fewer red photons than live cells imaged under the same conditions (Fig. 3.1C). Fitting Eq. 1.7 of the 3-state model (Fig. 3.1C) to the time courses of fluorescence signal per yeast cell showed that mEos3.2 in fixed cells had lower $M_n \times \varepsilon_f$ (Fig. 3.1D) and $\overline{R_s}$ (Fig. 3.1G) and

higher k_{act} (Fig. 3.1E) and k_{bl} (Fig. 3.1F) than live cells. Yeast cells fixed for 30 min had even lower fluorescence signals (Fig. 3.1D, G) and higher rate constants than cells fixed for 15 min (Fig. 3.1E, F). All the fitted parameters are described in Table 3.1.

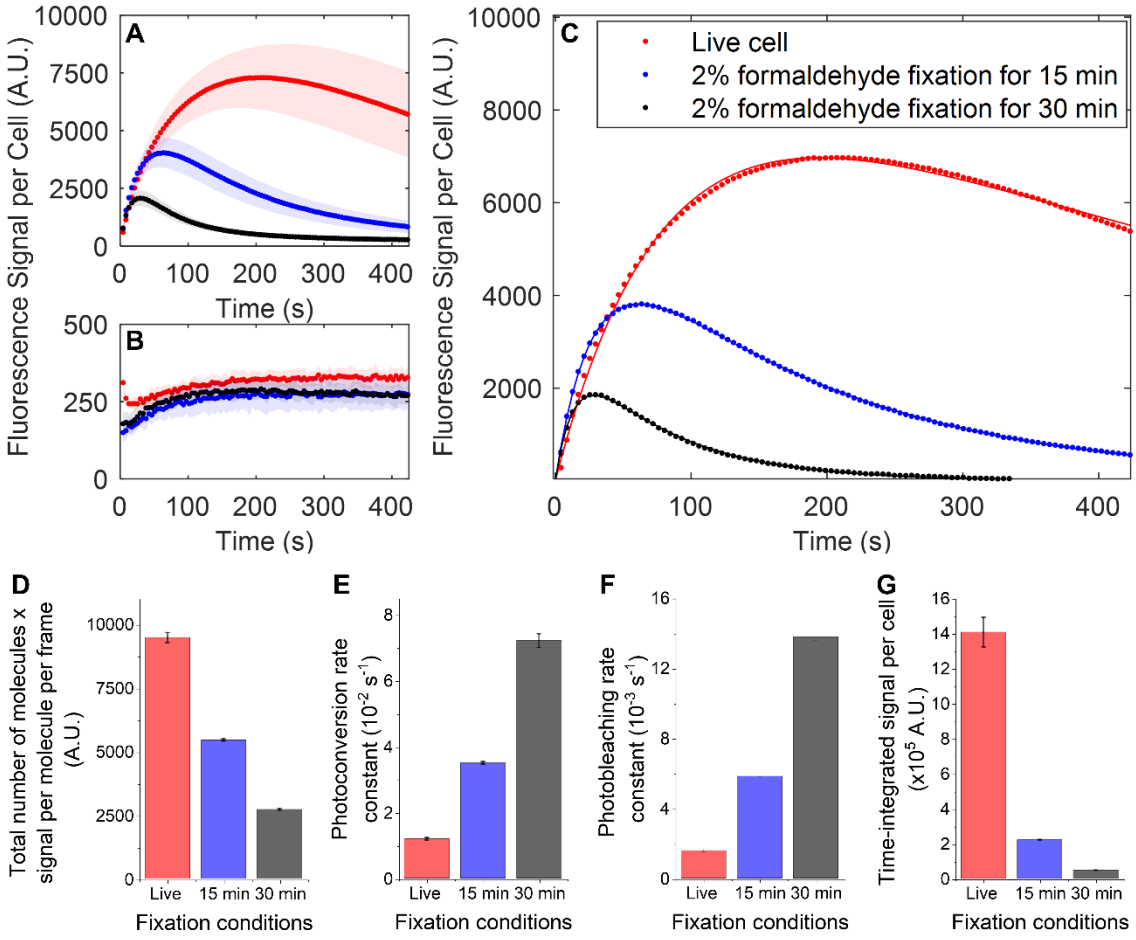

Figure 3.1: Effects of formaldehyde fixation on the fluorescence signal of mEos3.2 and rate constants for photoconversion and photobleaching.

(A) Time courses of the fluorescence signal per *S. pombe* cell expressing cytoplasmic mEos3.2 illuminated at 405 nm (22 µW) and 561 nm (15 µW) by point-scanning confocal microscopy under 3 conditions: live cells (red dots) or cells fixed with 2% formaldehyde for 15 min (blue dots) or 30 min (black dots) in EMM5S medium and imaged in EMM5S. Nine fields of view (FOV) of 85 µm x 85 µm were taken over time for each condition. Plots are weighted mean (dots) and standard deviations (shaded area) of the fluorescence signal per cell. (B) Time courses of the total autofluorescence signal per wildtype *S. pombe* cell under the same conditions as in panel A. Four FOVs of 85 µm x 85 µm over time were taken for each condition. Plots show weighted mean (dots) and standard deviations (shaded area) of the fluorescence

signal per cell. (C) Time courses of the mEos3.2 fluorescence signal per cell at 566-719 nm after autofluorescence subtraction. Eq. 1.7 of the 3-state model was fit to the experimental data (dots). The lines are theoretical curves using the parameters that best fit the data. (D-G) Comparison of parameters of live cells and cells fixed for 15 or 30 min. The error bars are 95% confidence intervals of the parameters (Table 3.1). (D) The product of total number of molecules per cell and signal of an R-state mEos3.2 molecule per frame ($M_n \times \varepsilon_f$) from the fit. (E) Photoconversion rate constant (k_{act}) from the fit. (F) Photobleaching rate constant (k_{bl}) from the fit. (G) Time-integrated signal per cell ($\overline{R_s}$) calculated using Eq. 1.8.

	Total number of molecules per cell x signal per molecule per frame (Mn x ε_f, A.U.)	Photoconversion rate constant (k_{act}, s^{-1})	Bleaching rate constant (k_{bl}, s^{-1})	Time-integrated signal per cell ($\overline{R_s}$, A.U.)
Live cells (N = 391)	9489 (9291, 9687)	1.20×10^{-2} (1.16, 1.24)	1.59×10^{-3} (1.50, 1.68)	1.41×10^{6} (1.33, 1.50)
2% formaldehyde fixed for 15 min (N = 303)	5456 (5434, 5478)	3.51×10^{-2} (3.48, 3.55)	5.84×10^{-3} (5.81, 5.88)	2.21×10^{5} (2.19, 2.22)
2% formaldehyde fixed for 30 min (N = 354)	2729 (2695, 2762)	7.23×10^{-2} (7.03, 7.44)	13.82×10^{-3} (13.60, 14.04)	4.67×10^{4} (4.57, 4.76)

Table 3.1: Effects of fixation on the fluorescence signal and photoconversion and photobleaching rate constants of mEos3.2 in *S. pombe* cells measured by point-scanning confocal microscopy.

The table lists the product of the total number of molecules per cell and the signal of the R-state mEos3.2 molecule per frame ($M_n \times \varepsilon_f$), photoconversion rate constant (k_{act}), and photobleaching rate constant (k_{bl}) from fitting Eq. 1.7 of the 3-state model to the data, and the time-integrated signal per cell ($\overline{R_s}$) calculated from Eq. 1.8 (Fig. 3.1). The 95% confidence intervals are reported in the brackets. (N = total number of the cells in the FOVs)

3.2 Fixation permeabilizes the yeast cell membrane for small molecules

I used fluorescein to test our hypothesis that formaldehyde fixation affects mEos3.2 photophysics by permeabilizing the yeast cell membrane for small molecules (Fig. 3.2).

Wildtype *S. pombe* cells were fixed for 15 min or 30 min as above. Fixed and live cells were mounted on coverslips coated with 0.5 mg/mL peanut-lectin (L0881-5MG; Sigma-Aldrich, St. Louis, MO) for 30 min. The cells were then incubated for 30 min in EMM5S medium containing 20 μM fluorescein (46960-25G-F; Sigma-Aldrich, St. Louis, MO) or

fluorescein-dextran 3,000 MW (D3305; Thermo Fisher Scientific, Waltham, MA). The live cells mixed with the dyes were imaged at room temperature (~23° C) immediately to minimize endocytosis of the dyes. Wildtype cells in EMM5S medium alone were prepared and imaged as negative controls for autofluorescence subtraction. Brightfield and confocal fluorescence images of the mid-sections of cells were acquired with the LSM880 microscope. The samples were excited at 488 nm (~22 μW at the sample) and the emitted fluorescence was collected using an emission band path filter with a 519-601 nm wavelength range. I analyzed the images in Fiji (Schindelin et al., 2012) by manually selecting ROIs of 5x5-pixel squares in the cells (~30-40 cells for each condition; 1 ROI per cell) and the extracellular environment (6~12 ROIs for each condition) (Fig. 3.2A). I measured the MSPP of all ROIs including the negative controls (for autofluorescence subtraction), quantified the cell permeability in each condition by calculating $(MSPP_{cytoplasmic} - MSPP_{negative\ control})/ MSPP_{extracellular}$, and reported the mean and standard deviation (Fig. 3.2D).

Live yeast cells excluded fluorescein (332 g/mol), but fixation with formaldehyde (without detergents or organic solvents) partially permeabilized the cell membrane, allowing the entry of fluorescein (Fig. 3.2D). Moreover, more fluorescein entered the cells fixed for 30 min than the cells fixed for 15 min (Fig. 3.2D). Thus, ions and small molecules in the imaging buffer, such as thiol DTT (154 g/mol), are likely to enter the fixed yeast cells and affect the photophysical properties of mEos3.2.

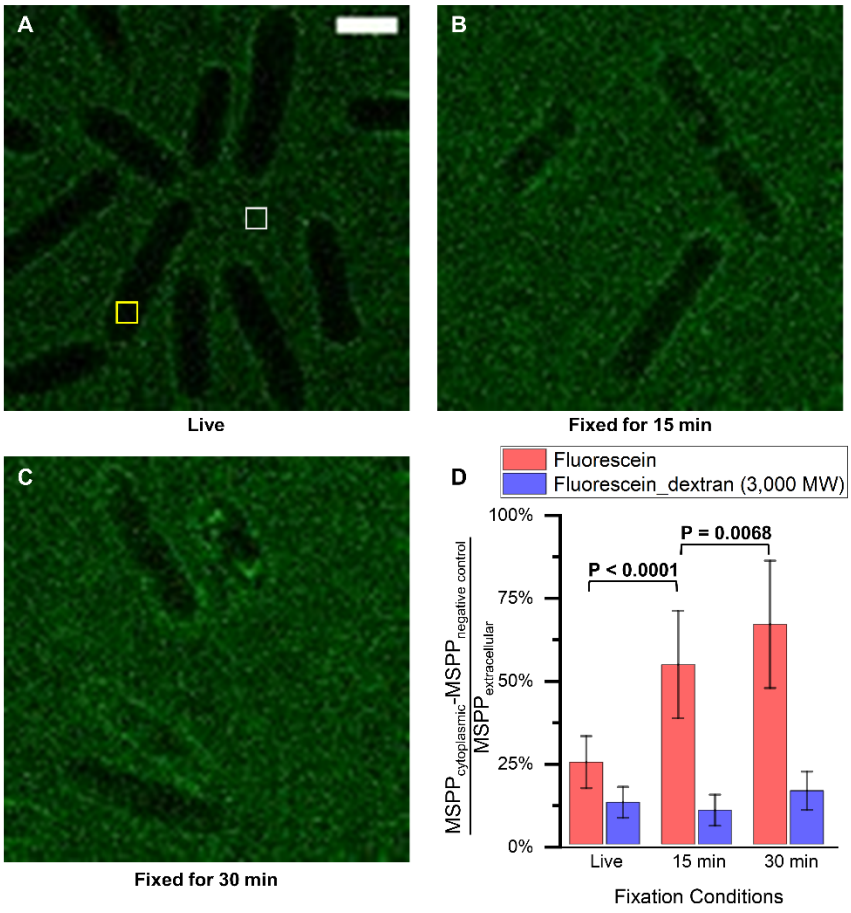

Figure 3.2: Effect of formaldehyde fixation on the permeability of *S. pombe* cells.

(A-E) Fluorescein mid-section images (green) of wild type *S. pombe* cells incubated in 20 µM fluorescein diluted in EMM5S medium. Conditions: (A) Live cell (scale bar = 5 µm, yellow box: ROI for measuring cytoplasmic mean signal per pixel (MSPP), white box: ROI for measuring extracellular mean signal per pixel); (B) cells fixed with 2% formaldehyde for 15 minutes; (C) cells fixed with 2% formaldehyde for 30 minutes. (D) Quantify cell permeability in live and fixed wildtype *S. pombe* cells using fluorescein and fluorescein_dextran (3,000 MW). Average cytoplasmic mean signal per pixel ($MSPP_{cytoplasmic}$) after autofluorescence subtraction ($MSPP_{negative\ control}$) divided by extracellular mean signal per pixel ($MSPP_{extracellular}$) were plotted. The error bars were standard deviation between cells in each condition. There was a significant percentage increase in the fluorescein signal in the cells fixed with 2% formaldehyde for 15 min compared to the live cells ($P<0.0001$). Longer fixation time (30 minutes versus 15 minutes, $P = 0.0068$) also increased the fluorescein signal in cells.

3.3 Imaging buffer affects mEos3.2 photophysics in fixed cells

Knowing that fixed *S. pombe* cells are likely permeable to small molecules, I tested how the composition of the imaging buffer influenced mEos3.2 photophysics (Fig. 3.3). I hypothesized that the photophysical changes of mEos3.2 in the fixed cells were due to the low pH (~5.5) and oxidizing environment of EMM5S relative to the live-cell cytoplasmic environment.

Therefore, to assess how pH and reducing agent affect the photophysical properties of mEos3.2, I fixed cells for 30 min as described in Chapter 3.1 and then washed and resuspended the cells in one of the following buffers: 50 mM MES (pH 5.5), 50 mM MES (pH 6.5), 50 mM Tris-HCl (pH 7.5), 50 mM Tris-HCl (pH 8.5), 50 mM Tris-HCl (pH 7.5) with 1 mM DTT, 50 mM Tris-HCl (pH 8.5) with 1 mM DTT, or 50 mM Tris-HCl (pH 8.5) with 10 mM DTT.

I found that $\overline{R_s}$ was higher (Fig. 3.3B), and k_{act} (Fig. 3.3D) and k_{bl} (Fig. 3.3E) were lower in imaging buffers with higher pH. Adding the reducing agent DTT to the imaging buffer further increased $\overline{R_s}$ (Fig. 3.3B) and decreased k_{bl} in the pH range we tested (Fig. 3.3E). A concentration of 1 mM DTT was more effective than 10 mM DTT at increasing $\overline{R_s}$ (Fig. 3.3B). Additionally, the value of $M_n \times \varepsilon_f$ from fixed cells in 50 mM Tris-HCl (pH 8.5) with 1 mM DTT (9187 A.U., 95% CI: 9024 – 9351, Table S2) was similar to that from live cells (9489 A.U., 95% CI: 9291 - 9687, Table 3.1). Values of $\overline{R_s}$ were also similar in live cells and fixed cells at pH 8.5 with 1 mM DTT (Table 3.1, 3.2).

Thus, mEos3.2 molecules survived fixation and the total number of molecules per cell able to fluoresce in the red channel (M_n) did not change, but the extracellular imaging buffer influenced the intracellular mEos3.2 signal per frame (ε_f) and other photophysical properties as photoconversion and photobleaching rates. In the following, I therefore used the imaging buffer at pH 8.5 with 1 mM DTT (called 'Tris8.5-DTT buffer') for many imaging experiments with fixed cells in Chapter 4.

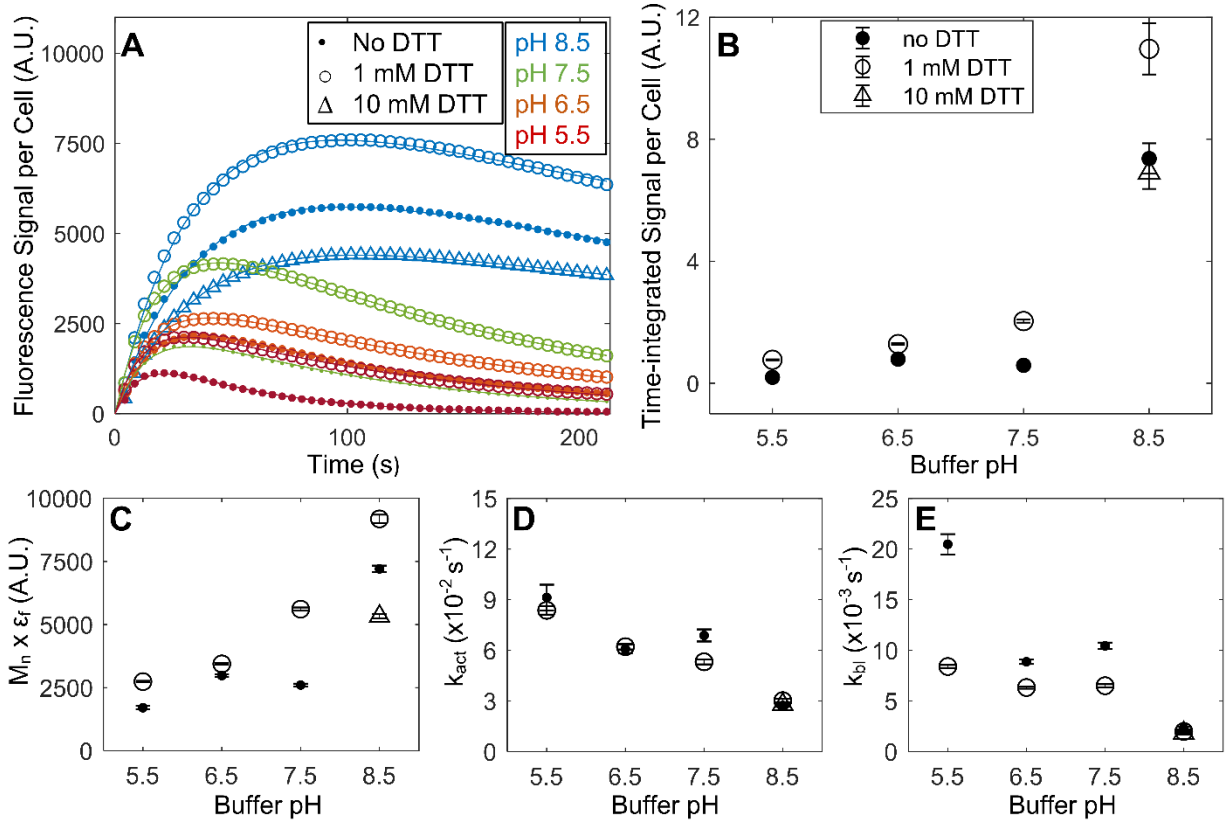

Figure 3.3: Effects of pH and DTT on the fluorescence signal and rate constants for photoconversion and photobleaching of mEos3.2 in fixed *S. pombe* cells.

(A) Time courses of the fluorescence signal per cell expressing cytoplasmic mEos3.2 (after autofluorescence subtraction). The cells were fixed with 2% formaldehyde for 30 min and illuminated at 405 nm (22 µW) and 561 nm (15 µW) by point-scanning confocal microscope under 9 different buffer conditions: (red dot) 50 mM MES (pH 5.5); (red circle) 50 mM MES (pH

5.5) with 1 mM DTT; (orange dot) 50 mM MES (pH 6.5); (orange circle) 50 mM MES (pH 6.5) with 1 mM DTT; (green dot) 50 mM Tris-HCl (pH 7.5); (green circle) 50 mM Tris-HCl (pH 7.5) with 1 mM DTT; (blue dot) 50 mM Tris-HCl (pH 8.5); (blue circle) 50 mM Tris-HCl (pH 8.5) with 1 mM DTT: (blue triangle) 50 mM Tris-HCl (pH 8.5) with 10 mM DTT. The continuous lines are best fits of Eq. 1.7 of the 3-state model to the time courses of the fluorescence signal per cell. Fig. 3.4 reports the raw data. (B-E) Dependence of the parameters on pH and DTT. The error bars are 95% confidence intervals for the parameters (Table 3.2). (B) Time-integrated signal per cell ($\overline{R_s}$) calculated using Eq. 1.8. (C) The product of total number of molecules per cell and the signal of an R-state mEos3.2 molecule per frame (M_n x ε_f) from the fit. (D) Photoconversion rate constant (k_{act}) from the fit. (E) Photobleaching rate constant (k_{bl}) from the fit.

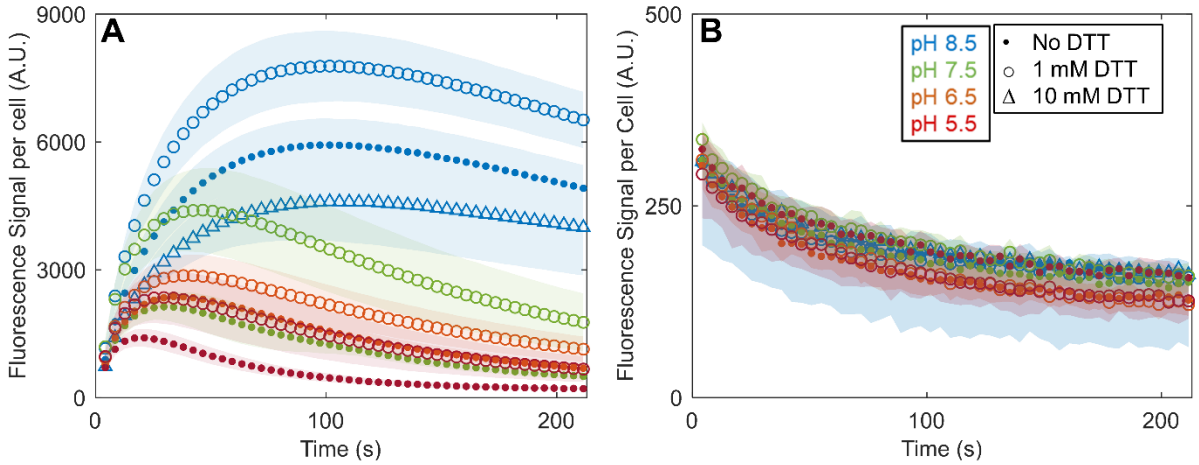

Figure 3.4: Effects of and DTT on mEos3.2 fluorescence signal in fixed *S. pombe* cells by point-scanning confocal microscopy.

Conditions: Time courses of fluorescence signal per *S. pombe* cell fixed with 2% formaldehyde in EMM5S medium for 30 min and imaged in various buffers under illumination at 405 nm (22 µW) and 561 nm (15 µW). Z-stacks with 19 slices from 8 FOVs of 85 µm x 85 µm were recorded at each time point. Plots are weighted mean (dots) and standard deviations (shaded area) of the fluorescence signal per cell. (A) *S. pombe* cells expressing cytoplasmic mEos3.2 under 9 different buffer conditions: (red dot) 50 mM MES (pH 5.5); (red circle) 50 mM MES (pH 5.5) with 1 mM DTT; (orange dot) 50 mM MES (pH 6.5); (orange circle) 50 mM MES (pH 6.5) with 1 mM DTT; (green dot) 50 mM Tris-HCl (pH 7.5); (green circle) 50 mM Tris-HCl (pH 7.5) with 1 mM DTT; (blue dot) 50 mM Tris-HCl (pH 8.5); (blue circle) 50 mM Tris-HCl (pH 8.5) with 1 mM DTT; (blue triangle) 50 mM Tris-HCl (pH 8.5) with 10 mM DTT. (B) Wild type *S. pombe* cells under the same 9 buffer conditions as panel A. Z-stacks with 19 slices from 4 FOVs of 85 µm x 85 µm were recorded at each time point and used for autofluorescence background subtraction.

	pH = 5.5 (N = 788)	pH = 6.5 (N = 695)	pH = 7.5 (N = 679)	pH = 8.5 (N = 645)	Live cell (N = 391)
Total number of molecules per cell x signal per molecule per frame (Mn x ε_f, A.U)	1706 (1641, 1771)	2979 (2929, 3030)	2605 (2550, 2661)	7207 (7076, 7338)	9489 (9291, 9687)
Photoconversion rate constant (k_{act}, s^{-1})	9.13×10^{-2} (8.38, 9.89)	6.08×10^{-2} (5.83, 6.33)	6.88×10^{-2} (6.52, 7.24)	2.73×10^{-2} (2.64, 2.82)	1.20×10^{-2} (1.16, 1.24)
Bleaching rate constant (k_{bl}, s^{-1})	20.48×10^{-3} (19.47, 21.48)	8.87×10^{-3} (8.63, 9.10)	10.44×10^{-3} (10.11, 10.77)	2.31×10^{-3} (2.16, 2.46)	1.59×10^{-3} (1.50, 1.68)
Time-integrated signal per cell ($\overline{R_s}$, A.U.)	0.20×10^{5} (0.18, 0.21)	0.79×10^{5} (0.77, 0.82)	0.59×10^{5} (0.57, 0.61)	7.36×10^{5} (6.87, 7.87)	1.41×10^{6} (1.33, 1.50)
	pH = 5.5 + 1 mM DTT (N = 654)	**pH = 6.5 + 1 mM DTT** (N = 663)	**pH = 7.5 + 1 mM DTT** (N = 789)	**pH = 8.5 + 1 mM DTT** (N = 777)	**pH = 8.5 + 10 mM DTT** (N = 660)
Total number of molecules per cell x signal per molecule per frame (Mn x ε_f, A.U)	2742 (2714, 2771)	3443 (3408, 3478)	5611 (5548, 5678)	9187 (9024, 9351)	5323 (5234, 5413)
Photoconversion rate constant (k_{act}, s^{-1})	8.37×10^{-2} (8.12, 8.63)	6.22×10^{-2} (6.05, 6.38)	5.32×10^{-2} (5.17, 5.48)	3.02×10^{-2} (2.92, 3.12)	2.79×10^{-2} (2.71, 2.89)
Bleaching rate constant (k_{bl}, s^{-1})	8.39×10^{-3} (8.26, 8.54)	6.32×10^{-3} (6.20, 6.44)	6.50×10^{-3} (6.36, 6.65)	1.98×10^{-3} (1.83, 2.13)	1.82×10^{-3} (1.69, 1.96)
Time-integrated signal per cell ($\overline{R_s}$, A.U.)	0.77×10^{5} (0.76, 0.79)	1.29×10^{5} (1.26, 1.31)	2.04×10^{5} (1.99, 2.09)	10.96×10^{5} (10.13, 11.80)	6.90×10^{5} (6.37, 7.43)

Table 3.2: Effects of pH and reducing agent on the fluorescence signal and photoconversion and photobleaching rate constants of mEos3.2 in fixed *S. pombe* cells measured by point-scanning confocal microscopy.

The table lists the product of the total number of molecules per cell and the signal of a R-state mEos3.2 molecule per frame ($M_n \times \varepsilon_f$), photoconversion rate constant (k_{act}), and photobleaching rate constant (k_{bl}) from fitting Eq. 1.7 of the 3-state model to the data, and the time-integrated signal per cell ($\overline{R_S}$) calculated from Eq. 1.8 (Fig. 3.3, Fig. 3.4). The 95% confidence intervals are reported in the brackets. (N = total number of the cells in the FOVs)

3.4 Comparison with GFP

I also measured how fixation would affect the photophysics of the most used fluorescent protein, GFP, in fission yeast cells (Fig. 3.5). Wildtype cells and cells expressing Fim1-GFP (TP347) were excited at 488 nm (~60 μW at the sample) and emission fluorescence in the range of 505-735 nm was collected. A 19-slice Z stack with 600-nm Z-step intervals covering a FOV of 85 x 85 μm (512 x 512 pixels; 160 nm pixel size) was imaged at each time point with a pixel dwell time of 0.85 μs. The entire time-lapse data set consisted of 100 Z-stacks. A single exponential decay was fit to the time course of GFP fluorescence signal per cell after autofluorescence subtraction to get the parameters giving the best fit to the data: GFP signal per cell at time 0 (without photobleaching), and the photobleaching rate constant. Fixation and the imaging buffer do not have a huge effect on GPF photophysics in fission yeast cells (Fig. 3.5).

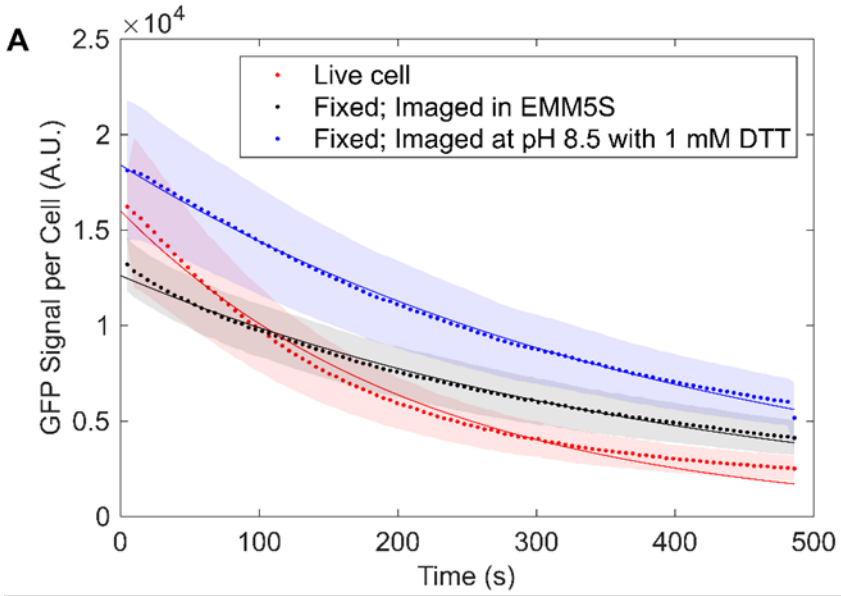

B

	GFP signal per cell (time = 0) (A.U.)	Photobleaching rate constant (s^{-1})
Live cell (N = 332)	16003 (15725, 16282)	4.60×10^{-3} (4.48, 4.72)
Fixed; Imaged in EMM5S (N = 425)	12620 (12523, 12716)	2.43×10^{-3} (2.40, 2.47)
Fixed; Imaged at pH 8.5 with 1 mM DTT (N = 444)	18407 (18322, 18493)	2.44×10^{-3} (2.42, 2.47)

Figure 3.5: Effects of fixation and imaging buffer on the fluorescence signal and photobleaching of GFP in *S. pombe* cells.

(A) Time courses of the GFP fluorescence signal per *S. pombe* cell expressing Fim1-GFP and excited at 488 nm by point-scanning confocal microscopy under 3 conditions: (red dots) live cells; (black dots) fixed with 2% formaldehyde in EMM5S for 30 min and imaged in EMM5S; (blue dots) fixed with 2% formaldehyde in EMM5S for 30 min and imaged in 50 mM Tris-HCl buffer at pH 8.5 with 1 mM DTT. Z-stacks from 4 FOVs of 85 x 85 µm were recorded for Fim1-GFP cells and 2 FOVs were recorded of wild type cells for autofluorescence background subtraction. A single exponential decay was fit to the time course of fluorescence signal (dots). The lines are theoretical curves with rate constants giving the best fit to the data. (B) Values of the GFP signal per cell at time 0 (without photobleaching) and the photobleaching rate constant from the best fit to the experimental data. The 95% confidence intervals of the fitted parameters are reported in brackets (N = total number of the cells in all FOVs).

3.5 Discussion

Preserving the fluorescence signal and structures of interest is crucial when fixing cells expressing fluorescent protein fusion proteins. I show that formaldehyde fixation does not destroy mEos3.2 molecules but likely permeabilizes yeast cells for small molecules, making the photophysical properties of mEos3.2 sensitive to the composition of the imaging buffer. The low pH of 5.5 and lack of oxygen scavenging system in the EMM5S synthetic medium affected the photophysical properties of mEos3.2 in fixed cells as expected from previous works showing that EosFP photoconverts faster (Wiedenmann et al., 2004) and mEos3.2 emits fewer red photons at acidic pH (M. Zhang et al., 2012). Photooxidation can increase the photobleaching rate (Greenbaum, Rothmann, Lavie, & Malik, 2000). Oxygen in the solution can also affect the fluorescence signal by promoting intersystem crossing (Mclean, Mcgarvey, Truscott, Lambert, & Land, 1990) and convert the excited molecules to the non-fluorescent triplet state.

My experiments also show that fixation conditions should be tested and optimized for each fluorescent protein. For example, mEos3.2 had even lower $\overline{R_s}$ and higher k_{act} and k_{bl} in cells fixed for 30 min rather than 15 min under the tested imaging condition (Fig. 3.1E-G). On the other hand, GFP was far less sensitive to fixation, as formaldehyde treatment had little effect on its fluorescence signal and photobleaching rate (Fig. 3.5).

The photophysics of mEos3.2 was similar in live cells and fixed cells in the Tris8.5-DTT buffer under low laser intensities (Fig. 3.3). Imaging buffers with a pH equal to or slightly higher than the cytoplasmic pH of fission yeast at ~7.3 (Y. Zhang, Shen, et al., 2017) increased $\overline{R_s}$ and reduced k_{act} and k_{bl} (Fig. 3.3B, D, E). Interestingly, the pH-

dependence of red mEos3.2 signal in fixed yeast cells differs from the known pH response of purified red mEos3.2 with a pKa of 5.8 (M. Zhang et al., 2012), as the big rise in signal occurs at pH 7.5 - 8.5 instead of pH 5.5 - 6.5 (Fig. 3.3C). I suspect that the cytoplasmic environment of fixed cells contributes to the observed difference. Adding a reducing agent DTT to the imaging buffer further increased $\overline{R_s}$ (Fig. 3.3B).

Chapter 4: Imaging conditions affect mEos3.2 photophysics

In Chapter 3, I showed that imaging mEos3.2 molecules in fixed fission yeast cells in the “Tris8.5-DTT” buffer gives photophysical parameters similar to live cells. Next, in this chapter I used laser-scanning confocal microscopy and widefield fluorescence microscopy to test the effects of a wide range of laser intensities on mEos3.2 photophysics in fixed *S. pombe* cells in the ‘Tris8.5-DTT’ buffer. I also characterized how the photophysics of mEos3.2 is affected by fixation and the imaging buffer by single-molecule localization microscopy (SMLM).

4.1 Effects of the 405-nm and 561-nm laser intensities on photophysical properties of mEos3.2 in live and fixed fission yeast cells

4.1.1 Laser-scanning confocal microscopy conditions

To test different imaging conditions, I used different pairs of 405-nm and 561-nm laser intensities on the laser scanning confocal microscope. I illuminated the samples simultaneously at 405-nm and 561-nm. The 405 nm laser power at the sample was set constant ranging from 16 to 56 μW and the 561 nm laser power constant ranging from 11 to 37 μW. To compare with widefield illumination conditions, I estimated the average intensity and the peak intensity of point-scanning illumination. The average intensities in the FOV (power at the sample divided by the FOV area) were 0.22 to 0.78 W/cm^2 at 405 nm and 0.15 to 0.51 W/cm^2 at 561 nm. The peak intensities (power at the sample divided by the size of the point spread function) were ~80 to 240 kW/cm^2 at 405 nm and

~20 to 80 kW/cm^2 at 561 nm. The raw data and parameters of the best fits are shown in Fig. 4.1 and Table 4.1.

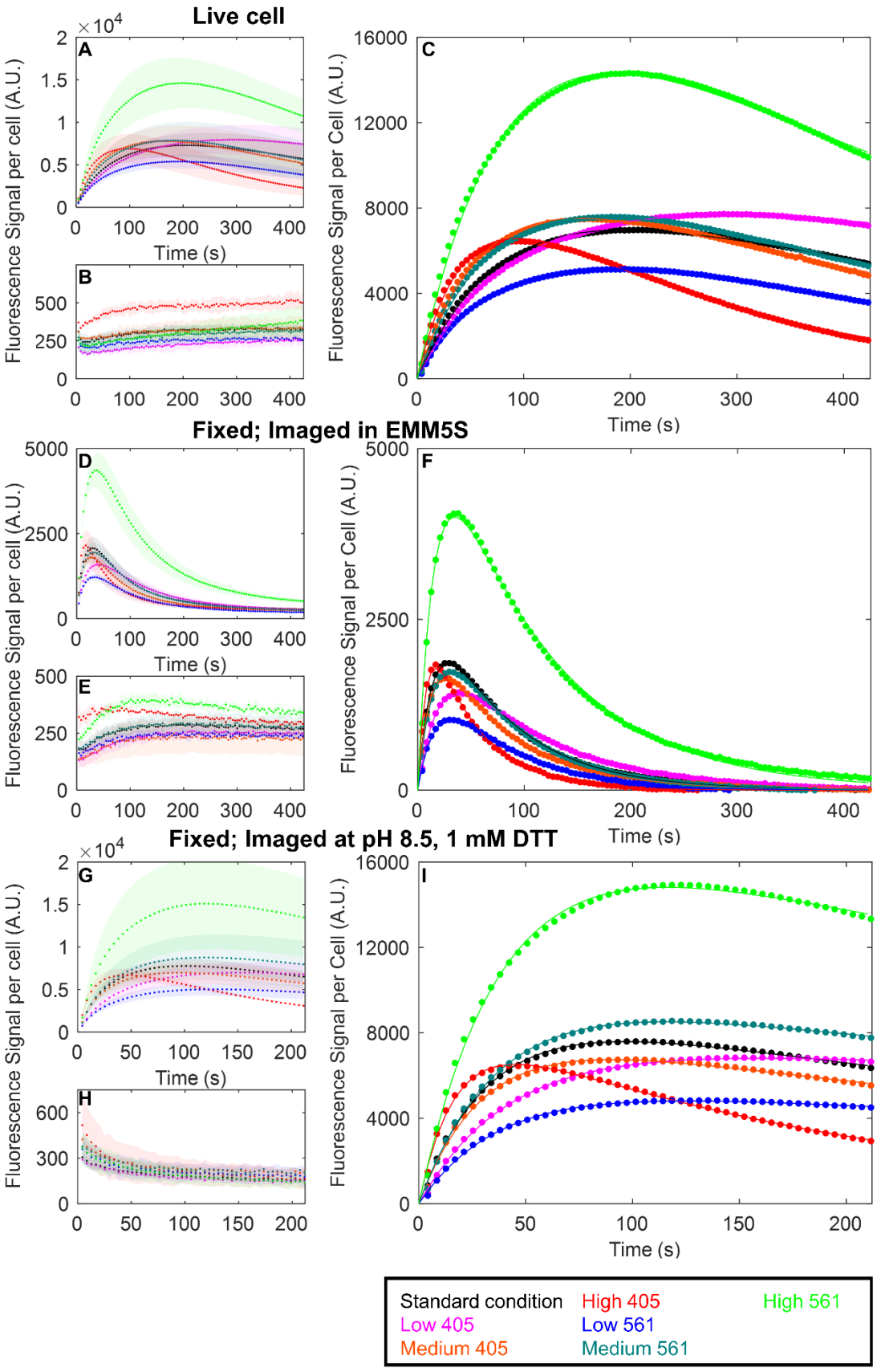
Live cell
Fixed; Imaged in EMM5S
Fixed; Imaged at pH 8.5, 1 mM DTT
A
B
C
D
E
F
G
H
I
Fluorescence Signal per cell (A.U.)
Fluorescence Signal per Cell (A.U.)
Time (s)
×10^4
Standard condition
High 405
High 561
Low 405
Low 561
Medium 405
Medium 561

Figure 4.1: Effects of 405-nm and 561-nm intensities on mEos3.2 fluorescence signal in live and fixed *S. pombe* cells by point-scanning confocal microscopy.

(A) Time courses of the fluorescence signal per live cell expressing cytoplasmic mEos3.2 under 7 different laser intensities. Conditions: (black dot) standard conditions: 405 nm laser power at 22 μW, and 561 laser power at 15 μW; (magenta dot) low 405 nm laser power at 16 μW; (orange dot) medium 405 laser power at 28 μW; (red dot) high 405nm laser power at 56 μW; (blue dot) low 561 nm laser power at 11 μW; (cyan dot) medium 561 nm laser power at 19 μW; (green dot) high 561 nm laser power at 37 μW. Z-stacks with 19 slices from 4 FOVs of 85 μm x 85 μm were recorded at each time point. Plots are weighted mean (dots) and standard deviation (shaded area) of the fluorescence signal per cell. (B) Time course of the autofluorescence signal per live wild type *S. pombe* cells under 7 different laser intensities. Z-stacks from two FOVs of 85 μm x 85 μm were recorded at each time point and used for autofluorescence background subtraction. Plots are weighted mean (dots) and standard deviation (shaded area) of the fluorescence signal per cell. (C) Eq. 1.7 of the 3-state model was fit to the time courses of mEos3.2 fluorescence signal per cell after autofluorescence background subtraction (dots). The lines are theoretical curves with fitted parameters giving the best fit to the data. (D-F) *S. pombe* cells fixed with 2% formaldehyde in EMM5S medium for 30 min and imaged in EMM5S medium under the same 7 laser intensities as in Panel A. (G-I) *S. pombe* cells fixed with 2% formaldehyde for 30 min in EMM5S and imaged in 50 mM Tris-HCl buffer at pH 8.5 with 1 mM DTT under the same 7 laser intensities as in Panel A.

Live cell	Standard (N = 391)	Low 405 (N = 370)	Medium 405 (N = 354)	High 405 (N = 300)	Low 561 (N = 377)	Medium 561 (N = 405)	High 561 (N = 257)
Total number of molecules per cell x signal per molecule per frame (Mn x ε_f)	9489 (9291, 9687)	8970 (8770, 9170)	10232 (10058, 10407)	9929 (9770, 10087)	7424 (7231, 7618)	10610 (10410, 10810)	20555 (20076, 21034)
Photoconversion rate constant ($k_{act,}$ s^{-1})	1.20 x 10^{-2} (1.16, 1.24)	1.10 x 10^{-2} (1.06, 1.14)	1.53 x 10^{-2} (1.48, 1.58)	2.13 x 10^{-2} (2.06, 2.19)	1.20 x 10^{-2} (1.15, 1.25)	1.31 x 10^{-2} (1.27, 1.35)	1.16 x 10^{-2} (1.12, 1.20)
Bleaching rate constant ($k_{bl,}$ s^{-1})	1.59 x 10^{-3} (1.50, 1.68)	0.57 x 10^{-3} (0.49, 0.66)	2.02 x 10^{-3} (1.94, 2.10)	4.43 x 10^{-3} (4.32, 4.54)	2.08 x 10^{-3} (1.96, 2.20)	1.96 x 10^{-3} (1.87, 2.05)	1.96 x 10^{-3} (1.85, 2.06)
Time-integrated signal per cell ($\overline{R_s}$, A.U.)	1.41 x 10^6 (1.33, 1.50)	3.72 x 10^6 (3.13, 4.31)	1.20 x 10^6 (1.15, 1.25)	0.53 x 10^6 (0.51, 0.55)	0.84 x 10^6 (0.79, 0.89)	1.28 x 10^6 (1.22, 1.34)	2.48 x 10^6 (2.34, 2.62)
Fixed and imaged in EMM5S	**Standard (N = 354)**	**Low 405 (N = 375)**	**Medium 405 (N = 391)**	**High 405 (N = 277)**	**Low 561 (N = 390)**	**Medium 561 (N = 403)**	**High 561 (N = 258)**
Total number of molecules per cell x signal per molecule per frame (Mn x ε_f)	2729 (2696, 2762)	2160 (2141, 2178)	2320 (2291, 2348)	2586 (2533, 2639)	1732 (1661, 1804)	2692 (2655, 2728)	5595 (5517, 5672)
Photoconversion rate constant ($k_{act,}$ s^{-1})	7.23 x 10^{-2} (7.03, 7.44)	5.00 x 10^{-2} (4.91, 5.10)	8.39 x 10^{-2} (8.13, 8.65)	12.34 x 10^{-2} (11.71, 12.96)	5.32 x 10^{-2} (4.90, 5.73)	6.14 x 10^{-2} (5.96, 6.32)	6.43 x 10^{-2} (6.19, 6.66)
Bleaching rate constant ($k_{bl,}$ s^{-1})	13.82 x 10^{-3} (13.60, 14.04)	10.73 x 10^{-3} (10.62, 10.85)	13.89 x 10^{-3} (13.66, 14.11)	21.99 x 10^{-3} (21.40, 22.58)	15.82 x 10^{-3} (15.01, 16.63)	14.34 x 10^{-3} (14.09, 14.59)	9.69 x 10^{-3} (9.51, 9.87)
Time-integrated signal per cell ($\overline{R_s}$, A.U.)	4.67 x 10^4 (4.57, 4.76)	4.76 x 10^4 (4.69, 4.83)	3.95 x 10^4 (3.87, 4.03)	2.78 x 10^4 (2.69, 2,87)	2.59 x 10^4 (2.69, 2.87)	4.44 x 10^4 (4.34, 4.54)	13.65 x 10^4 (13.34, 13.97)
Fixed; imaged at pH 8.5 with 1 mM DTT	**Standard (N = 777)**	**Low 405 (N = 383)**	**Medium 405 (N = 325)**	**High 405 (N = 366)**	**Low 561 (N = 335)**	**Medium 561 (N = 362)**	**High 561 (N = 267)**
Total number of molecules per cell x signal per molecule per frame (Mn x ε_f)	9187 (9024, 9351)	7451 (7288, 7614)	8081 (7938, 8225)	8286 (8191, 8382)	5482 (5364, 5599)	9950 (9752, 10148)	17653 (17193, 18112)
Photoconversion rate constant ($k_{act,}$ s^{-1})	3.02 x 10^{-2} (2.92, 3.12)	2.38 x 10^{-2} (2.29, 2.47)	3.31 x 10^{-2} (3.19, 3.43)	5.85 x 10^{-2} (5.67, 6.03)	2.69 x 10^{-2} (2.59, 2.80)	2.74 x 10^{-2} (2.64, 2.84)	2.60 x 10^{-2} (2.48, 2.73)
Bleaching rate constant ($k_{bl,}$ s^{-1})	1.98 x 10^{-3} (1.83, 2.13)	0.56 x 10^{-3} (0.41, 0.72)	2.00 x 10^{-3} (1.85, 2.15)	5.28 x 10^{-3} (5.16, 5.41)	1.05 x 10^{-3} (0.88, 1.21)	1.35 x 10^{-3} (1.19, 1.50)	1.51 x 10^{-3} (1.31, 1.71)
Time-integrated signal per cell ($\overline{R_s}$, A.U.)	1.10 x 10^6 (1.01, 1.18)	3.15 x 10^6 (2.30, 3.99)	0.96 x 10^6 (0.88, 1.03)	0.37 x 10^6 (0.36, 0.38)	1.23 x 10^6 (1.03, 1.44)	1.74 x 10^6 (1.53, 1.95)	2.76 x 10^6 (2.39, 3.14)

Table 4.1: Effects of laser intensities on the fluorescence signal and photoconversion and photobleaching rate constants of mEos3.2 in live and fixed *S. pombe* cells measured by point-scanning confocal microscopy.

The table lists the product of the total number of molecules per cell and the signal of the R-state mEos3.2 molecule per frame (M_n x ε_f), photoconversion rate constant (k_{act}), and photobleaching rate constant (k_{bl}) from fitting Eq. 1.7 of the 3-state model to the data, and the time-integrated signal per cell ($\overline{R_s}$) calculated from Eq. 1.8 (Fig. 4.1, 4.3). The 95% confidence intervals are reported in the brackets. (N = total number of the cells in the FOVs)

4.1.2 Widefield fluorescence microscopy conditions

For widefield fluorescence imaging, time lapse videos were acquired with a custom-built single-molecule localization microscope (SMLM) based on a Leica DMi8 stand with widefield illumination, a 63x/1.47 NA oil-immersion objective, and a band pass filter to collect emission fluorescence in the 584-676 nm wavelength range. Samples were illuminated at both 405 nm and 561 nm and imaged with an sCMOS camera (Hamamatsu ORCA-Flash4.0 V2) at 50 frames per second (fps) for 15,000 frames. To test different imaging conditions, I tested different pairs of 405-nm and 561-nm laser intensities. The 405-nm laser intensity was set constant in a range from 0.5 to 2 W/cm^2, and the 561-nm laser intensity from 1 W/cm^2 to 1 kW/cm^2. I manually selected a region of interest (ROI) 1 (~ 25 cells for the widefield images) with the polygon tool and selected the background ROI 2 with the square tool (Fig. 1.1). I fit Eq. 1.7 individually to the time courses of fluorescence signal per cell (after autofluorescence background subtraction) from each FOV. I calculated the mean fitted parameters and standard deviation weighted by the number of cells in each FOV. The raw data and parameters of the best fits are shown in Fig. 4.2 and Table 4.2.

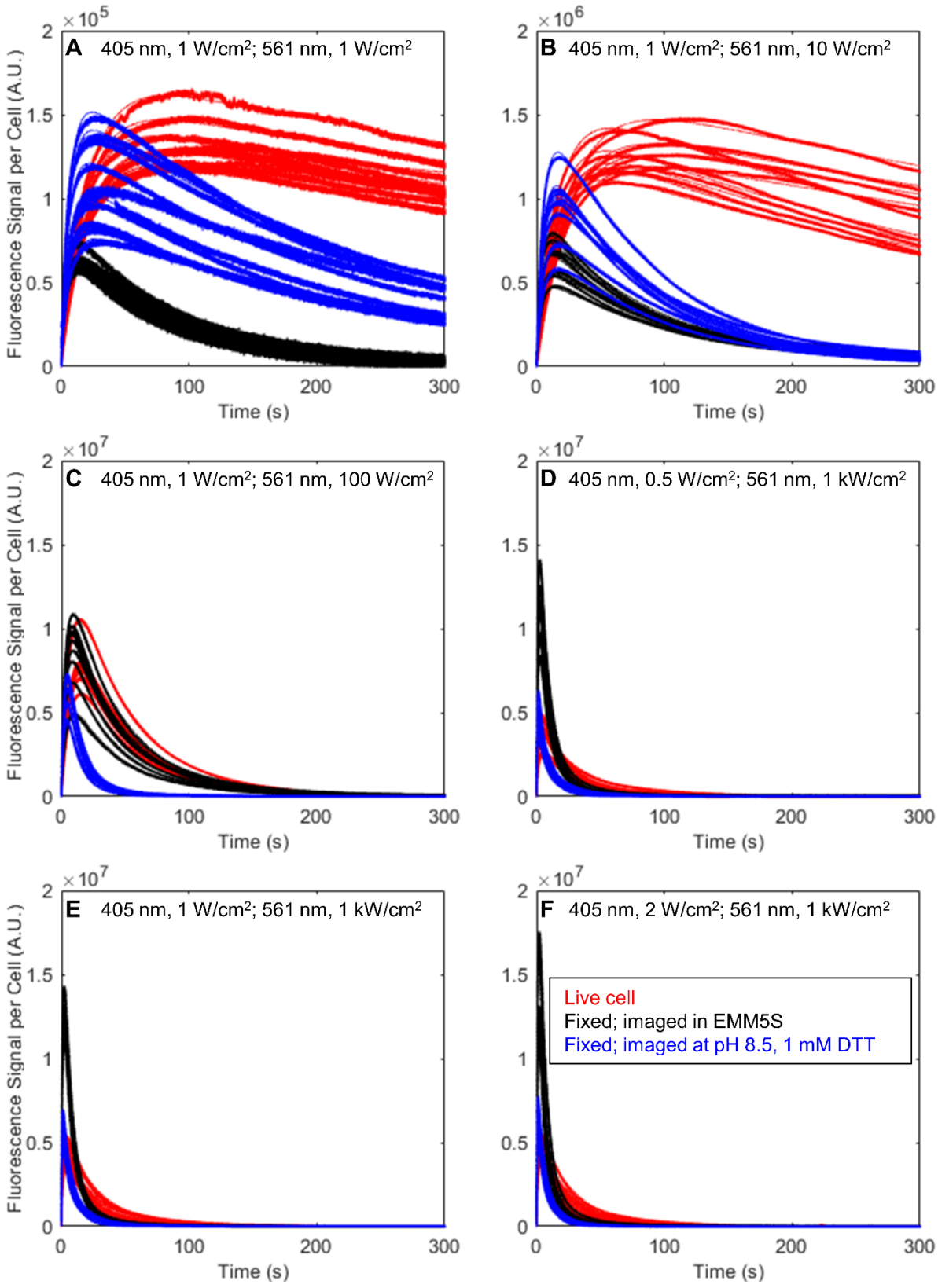
A 405 nm, 1 W/cm²; 561 nm, 1 W/cm²
B 405 nm, 1 W/cm²; 561 nm, 10 W/cm²
C 405 nm, 1 W/cm²; 561 nm, 100 W/cm²
D 405 nm, 0.5 W/cm²; 561 nm, 1 kW/cm²
E 405 nm, 1 W/cm²; 561 nm, 1 kW/cm²
F 405 nm, 2 W/cm²; 561 nm, 1 kW/cm²
Live cell
Fixed; imaged in EMM5S
Fixed; imaged at pH 8.5, 1 mM DTT
Fluorescence Signal per Cell (A.U.)
Time (s)

Figure 4.2: The effects of the 405-nm and 561-nm laser intensities on mEos3.2 fluorescence signal from live and fixed *S. pombe* cells by epi-fluorescence microscopy.

Time courses of the fluorescence signal per cell expressing cytoplasmic mEos3.2 in each FOV (after autofluorescence background subtraction): live cells (red dots) and cells fixed with 2% formaldehyde in EMM5S medium for 30 min and imaged in EMM5S (black dots) or imaged in 50 mM Tris-HCl buffer at pH 8.5 with 1 mM DTT (blue dots). Cells were illuminated continuously at 405 nm and 561 nm and imaged at 50 fps with 20-ms exposure time. The continuous lines are best fits of Eq. 1.7 of the 3-state model to the data (dots). Conditions: (A) 405 nm laser intensity at 1 W/cm^2, 561 nm laser intensity at 1 W/cm^2; (B) 405 nm laser intensity at 1 W/cm^2, 561 nm laser intensity at 10 W/cm^2; (C) 405 nm laser intensity at 1 W/cm^2, 561 nm laser intensity at 100 W/cm^2; (D) 405 nm laser intensity at 0.5 W/cm^2, 561 nm laser intensity at 1 kW/cm^2; (E) 405 nm laser intensity at 1 W/cm^2, 561 nm laser intensity at 1 kW/cm^2; (F) 405 nm laser intensity at 2 W/cm^2, 561 nm laser intensity at 1 kW/cm^2. Multiple curves of the same color are data collected from different FOVs and samples.

Live cell	561 nm laser intensity (W/cm^2)				405 nm laser intensity (W/cm^2)		
	1	10	100	1000	0.5	1	2
	(N = 249)	(N = 261)	(N = 270)	(N = 261)	(N = 262)	(N = 261)	(N = 232)
Total number of molecules per cell x signal per molecule per frame (Mn x ε_f)	1.42 x 10^5 (1.52 x 10^4)	1.42 x 10^6 (1.22 x 10^5)	1.05 x 10^7 (1.50 x 10^6)	4.86 x 10^6 (7.38 x 10^5)	4.49 x 10^6 (9.22 x 10^5)	4.86 x 10^6 (7.38 x 10^5)	5.39 x 10^6 (8.04 x 10^5)
Photoconversion rate constant ($k_{act,}$ s^{-1})	5.08x10^{-2} (0.24)	5.22 x10^{-2} (1.17)	15.20 x10^{-2} (0.89)	109.22x10^{-2} (27.57)	83.49x10^{-2} (14.72)	109.22x10^{-2} (27.57)	103.28x10^{-2} (11.65)
Bleaching rate constant ($k_{bl,}$ s^{-1})	0.92x10^{-3} (0.17)	1.68x10^{-3} (0.53)	22.2 x10^{-3} (0.84)	42.09x10^{-3} (5.62)	39.8 x10^{-3} (7.01)	42.09x10^{-3} (5.62)	49.72x10^{-3} (9.21)
Time-integrated signal per cell ($\overline{R_s}$, A.U.)	7.72 x 10^9 (1.62)	4.23 x 10^{10} (1.38)	2.36 x 10^{10} (0.35)	5.78 x 10^9 (1.17)	5.64 x 10^9 (1.53)	5.78 x 10^9 (1.17)	5.42 x 10^9 (1.29)

Fixed and imaged in EMM5S	561 nm laser intensity (W/cm^2)				405 nm laser intensity (W/cm^2)		
	1	10	100	1000	0.5	1	2
	(N = 246)	(N = 222)	(N = 248)	(N = 238)	(N = 250)	(N = 238)	(N = 250)
Total number of molecules per cell x signal per molecule per frame (Mn x ε_f)	7.22 x 10^4 (4.89 x 10^3)	6.99 x 10^5 (1.24 x 10^5)	1.04 x 10^7 (2.27 x 10^6)	1.60 x 10^7 (1.56 x 10^6)	1.39 x 10^7 (2.14 x 10^6)	1.60 x 10^7 (1.56 x 10^6)	1.71 x 10^7 (3.18 x 10^6)
Photoconversion rate constant ($k_{act,}$ s^{-1})	25.94x10^{-2} (2.67)	28.57x10^{-2} (2.22)	33.95x10^{-2} (2.68)	115.51x10^{-2} (9.60)	100.40x10^{-2} (6.29)	115.51x10^{-2} (9.60)	125.62x10^{-2} (8.39)
Bleaching rate constant ($k_{bl,}$ s^{-1})	11.76x10^{-3} (1.73)	9.54x10^{-3} (1.22)	23.58x10^{-3} (0.88)	121.85x10^{-3} (8.77)	104.32x10^{-3} (2.93)	121.85x10^{-3} (8.77)	148.50x10^{-3} (16.94)
Time-integrated signal per cell ($\overline{R_s}$, A.U.)	3.07 x 10^8 (0.50)	3.67 x 10^9 (0.83)	2.20 x 10^{10} (0.49)	6.55 x 10^9 (0.80)	6.64 x 10^9 (1.05)	6.55 x 10^9 (0.80)	5.76 x 10^9 (1.26)

Fixed; imaged at pH 8.5 with 1 mM DTT	561 nm laser intensity (W/cm^2)				405 nm laser intensity (W/cm^2)		
	1	10	100	1000	0.5	1	2
	(N = 277)	(N = 230)	(N = 210)	(N = 224)	(N = 222)	(N = 224)	(N = 261)
Total number of molecules per cell x signal per molecule per frame (Mn x ε_f)	1.20 x 10^5 (2.84 x 10^4)	1.11 x 10^6 (2.62 x 10^5)	8.03 x 10^7 (1.42 x 10^6)	6.49 x 10^6 (9.07 x 10^5)	5.16 x 10^6 (1.06 x 10^6)	6.49 x 10^6 (9.07 x 10^5)	6.58 x 10^6 (1.12 x 10^6)
Photoconversion rate constant ($k_{act,}$ s^{-1})	15.83x10^{-2} (1.47)	18.16x10^{-2} (0.75)	474.56x10^{-2} (0.95)	2417.70x10^{-2} (14.07)	2401.09x10^{-2} (21.29)	2417.70x10^{-2} (14.07)	2642.25x10^{-2} (18.51)
Bleaching rate constant ($k_{bl,}$ s^{-1})	4.04x10^{-3} (0.55)	10.95x10^{-3} (1.13)	80.05x10^{-3} (6.76)	118.56x10^{-3} (9.57)	101.69x10^{-3} (14.70)	118.56x10^{-3} (9.57)	132.86x10^{-3} (12.08)
Time-integrated signal per cell ($\overline{R_s}$, A.U.)	1.49 x 10^9 (0.41)	5.06 x 10^9 (1.30)	5.01 x 10^9 (0.98)	2.73 x 10^9 (0.44)	2.54 x 10^9 (0.64)	2.73 x 10^9 (0.44)	2.48 x 10^9 (0.48)

Table 4.2: Effects of laser intensities on the fluorescence signal and photoconversion and photobleaching rate constants of mEos3.2 in live and fixed *S. pombe* cells measured by widefield fluorescence microscopy.

The table lists the product of the total number of molecules per cell and the signal of the R-state mEos3.2 molecule per frame (M_n x ε_f), photoconversion rate constant (k_{act}), and photobleaching rate constant (k_{bl}) from fitting Eq. 1.7 of the 3-state model to the data, and the time-integrated signal per cell ($\overline{R_s}$) calculated from Eq. 1.8 (Fig. 4.2, 4.3). The 95% confidence intervals are reported in the brackets. (N = total number of the cells in the FOVs)

4.1.3 Effects of laser intensities and illumination methods on mEos3.2 photophysics

I used laser-scanning confocal microscopy and widefield fluorescence microscopy to test the effects of a wide range of laser intensities on mEos3.2 photophysics in fixed *S. pombe* cells in Tris8.5-DTT buffer (Fig. 4.3). The products of total mEos3.2 molecules per cell and signal per R-state molecule per frame ($M_n \times \varepsilon_f$) were similar in live cells and fixed cells in Tris8.5-DTT buffer (Fig. 4.3A-D). This was true for low-power laser-scanning confocal microscopy conditions as well as widefield SMLM imaging conditions with a 405-nm laser intensity of 0.5-2 W/cm^2 and a 561-nm laser intensity of 1 kW/cm^2 (Fig. 4.3C). However, at widefield 561-nm laser intensities of 10 and 100 W/cm^2, the time-integrated signal per cell ($\overline{R_s}$) differed in live cells and fixed cells in Tris8.5-DTT buffer (Fig. 4.3P). Fixation and the imaging buffer had different effects on $M_n \times \varepsilon_f$ (Fig. 4.3D), k_{act} (Fig. 4.3H), k_{bl} (Fig. 4.3L) and $\overline{R_s}$ (Fig. 4.3P) of mEos3.2 depending on the 561-nm laser intensities.

To compare imaging conditions quantitatively, I explored the effects of laser intensities on mEos3.2 photophysics by point-scanning illumination (Fig. 4.3, left 2 columns, Fig. 4.1, Table 4.1). $\overline{R_s}$ decreased (Fig. 4.3M), and both rate constants (Fig. 4.3E, I) increased with higher 405-nm laser intensity. The time-integrated signal per cell $\overline{R_s}$ increased with higher 561-nm laser intensity (Fig. 4.3N), but the 561-nm laser intensity had only modest effects on both rate constants (Fig. 4.3F, J) in the range we tested.

I used widefield illumination to explore the effects of a wider range of 561-nm laser intensities on mEos3.2 photophysics, including the high 561-nm laser intensity of ~1

kW/cm^2 often used in SMLM (Fig. 4.3, right 2 columns, Fig. 4.2, Table 4.2). Values of k_{bl} increased with higher 405-nm laser intensity (Fig. 4.3K), as observed with point-scanning illumination (Fig. 4.3I), but the 405-nm laser intensity had remarkably little impact on k_{act} (Fig. 4.3G) under SMLM conditions, which was likely caused by the high 561-nm laser intensity of 1 kW/cm^2 driving some photoconversion (Thedie et al., 2017). The time-integrated signal per cell $\overline{R_s}$ increased with higher 561-nm laser intensity and then plateaued and dropped (Fig. 4.3P). Both k_{act} and k_{bl} increased dramatically with 561-nm laser intensities (Fig. 4.3H, L) above the intensities used for point-scanning illumination (Fig. 4.3F, J). The discussion section considers these differences between the confocal and widefield imaging conditions.

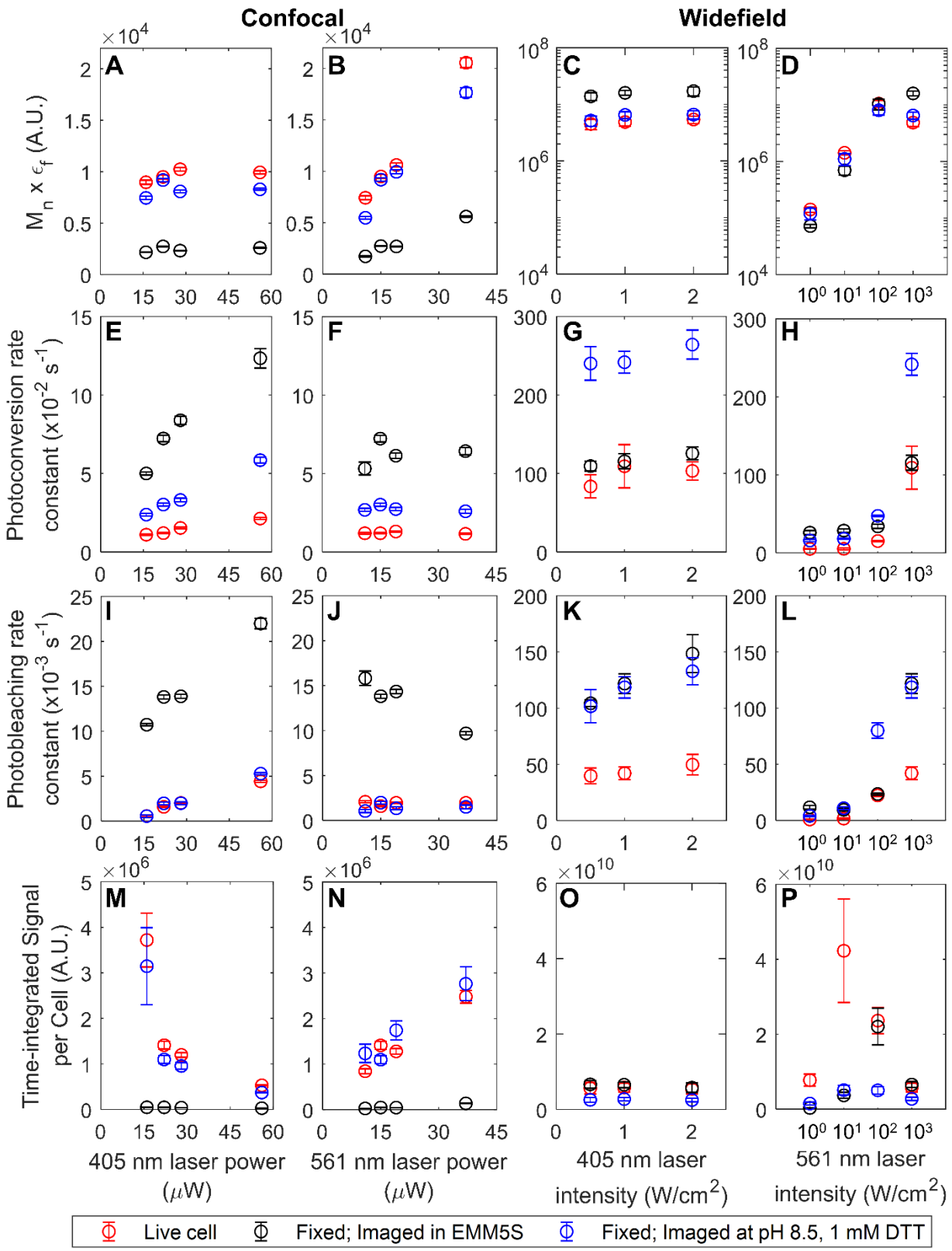
Confocal
Widefield
A
B
C
D
E
F
G
H
I
J
K
L
M
N
O
P
M_n x ϵ_f (A.U.)
Photoconversion rate constant (x10^{-2} s^{-1})
Photobleaching rate constant (x10^{-3} s^{-1})
Time-integrated Signal per Cell (A.U.)
405 nm laser power (μW)
561 nm laser power (μW)
405 nm laser intensity (W/cm^2)
561 nm laser intensity (W/cm^2)
Live cell
Fixed; Imaged in EMM5S
Fixed; Imaged at pH 8.5, 1 mM DTT

Figure 4.3: The effects of 405-nm and 561-nm laser intensities on the fluorescence signal and rate constants for photoconversion and photobleaching of mEos3.2 in live and fixed *S. pombe* cells.

Cells expressing cytoplasmic mEos3.2 were imaged live (red circles) or fixed with 2% formaldehyde for 30 min in EMMS5 medium and mounted in EMM5S medium (black circles) or Tris8.5-DTT buffer (blue circles). Cells were imaged with 7 different laser intensities by confocal microscope and 6 different laser intensities by widefield microscope. For confocal imaging, the laser powers and corresponding average intensities were set as follows: Panels A, E, I and M, the 561 nm laser power was set at 15 μW (~ 0.3 W/cm^2) and the 405 nm laser intensity ranged from ~ 0.2 - 0.8 W/cm^2; Panels B, F, J, and N, the 405 nm laser power was set at 22 μW (~ 0.2 W/cm^2) and the 561 nm laser intensity ranged from ~ 0.15 - 0.5 W/cm^2. Four FOVs were taken for each condition with cells expressing mEos3.2. Two FOVs were taken for each condition with wildtype cells. For widefield imaging, 561 nm laser intensity was set at 1 kW/cm^2 for panels C, G, K, O; 405 nm laser intensity was set at 1 W/cm^2 for panels D, H, L, P. Eight to ten FOVs were taken for each condition with cells expressing mEos3.2. Three or four FOVs were taken for each condition with wildtype cells. Eq. 1.7 of the 3-state model was fit to the time courses of fluorescence signal to determine the parameters giving the best fit: (A-D) The product of total number of molecules per cell and the signal of an R-state mEos3.2 molecule per frame (M_n x ε_f); (E-H) photoconversion rate constant (k_{act}); and (I-L) photobleaching rate constant (k_{bl}) (Table 4.1, Table 4.2). (M-P) Time-integrated signal per cell ($\overline{R_s}$) calculated using Eq. 1.8 (Table 4.1, Table 4.2). The error bars in the left 2 columns are 95% confidence intervals of the fit. The error bars in the right 2 columns are the weighted standard deviations among different FOVs. Fig. 4.1 and Fig. 4.2 report the raw data.

4.1.4 Discussion

I compared the photophysical properties of mEos3.2 with point-scanning and widefield illumination. With point-scanning illumination, each area of the sample was illuminated for a very short time at high peak intensity (e.g. ~80 kW/cm^2, Fig. 4.3), while the other pixels were kept in the dark. Thus, the average intensity of the laser power over the entire field of view was ~10^4 times lower than the peak intensity (e.g. ~0.5 W/cm^2, Fig. 4.3).

Despite huge differences in the instantaneous peak intensities in point-scanning and widefield microscopy, the rate constants for photoconversion and photobleaching in live cells were similar at similar average intensities (Table 4.1, 4.2). For example, with average intensities of ~ 0.5 to 1.1 W/cm^2 for both lasers, confocal and widefield imaging

of live cells gave similar values for k_{act} (~1.5 x 10^{-2} s^{-1} vs. ~5 x 10^{-2} s^{-1}) and k_{bl} (~2 x 10^{-3} s^{-1} vs. ~1 x 10^{-3} s^{-1}). Moreover, the photophysical parameters of mEos3.2 trended similarly with illumination intensities by both point-scanning confocal and widefield microscopy. For example, k_{bl} increased with higher 405-nm intensity (Fig. 4.3I, K) and M_n x ε_f increased with higher 561-nm laser intensity (Fig. 4.3B, D). However, these trends diverged at higher 561-nm laser intensities of 100 and 1000 W/cm^2 above the range of the confocal microscope. For example, k_{act} increased dramatically with 561-nm laser intensity (Fig. 4.3H), but only increased slightly with 405-nm laser intensity (Fig. 4.3G, 561-nm laser intensity = 1 kW/cm^2).

I conclude that the 561-nm laser contributed strongly to photoconversion at high intensities. My results differ from Thedie *et al.* (Thedie et al., 2017), who reported that high 561-nm laser intensities (1.2 – 4.8 kW/cm^2) slow the photoconversion of single mEos2 molecules embedded in PVA under weak 405-nm illumination (0.03 W/cm^2). Their interpretation was that 561-nm illumination pushes green-state mEos2 molecules into a transient off state that cannot be photoconverted. Both the sample conditions and illumination intensities differ between the experiments. For example, their mEos2 molecules were immobilized in PVA with restricted access to oxygen rather than being in a physiological environment in cells. Additionally, I used more intense 405-nm illumination (1 W/cm^2) and less intense 561-nm laser intensity (0.001 – 1 kW/cm^2) where green molecules in the transient off state may convert back to the fluorescent state, thus promoting photoconversion to the red-state.

The effects of the fixation and imaging buffer on mEos3.2 photophysics is also consistent under different illumination methods. For example, under comparable, low average 405-nm and 561-nm laser intensities (~1 W/cm^2), the time-integrated signal per cell $\overline{R_s}$ (Fig. 4.3N, P) was lower and photoconversion (Fig. 4.3F, H) and photobleaching rates constants (Fig. 4.3J, L) were higher in fixed cells in EMM5S compared to live cells and fixed cells in the Tris8.5-DTT buffer. However, fixation and imaging buffer affect mEos3.2 photophysics differently at higher 561-nm laser intensities of 100 and 1000 W/cm^2, above the range of confocal microscope. For example, $\overline{R_s}$ was lower in fixed cells in EMM5S (pH 5.5) than in live cells under low 561-nm laser intensity in the range of 1-10 W/cm^2, while for a high 561-nm laser intensity of 1 kW/cm^2 the trend was the opposite (Fig. 4.3P). The $\overline{R_s}$ in the fixed cells was only higher in the Tris8.5-DTT buffer than in EMM5S under low 561-nm laser intensities of 1-10 W/cm^2 (Fig. 4.3P). Moreover, under low 561-nm laser intensities both k_{act} (Fig. 4.3E, H) and k_{bl} (Fig. 4.3I, L) in fixed cells in EMM5S were higher than in live cells and fixed cells in Tris8.5-DTT buffer, while under higher 561-nm laser intensities some measurements of the rates were lower than in the Tris8.5-DTT buffer (Fig. 4.3H, L). Oxygen in the environment could promote intersystem crossing and convert the excited fluorophores to the non-fluorescent triplet state, where the molecules could return to the fluorescent state through laser excitation. The laser intensity could potentially affect the probability that the triple state molecules return to the fluorescent state. Therefore, the redox environment in the imaging buffer for fixed cells may affect mEos3.2 photophysics differently depending on the 561-nm laser intensity.

4.2 Single-molecule characterization of mEos3.2 in live and fixed yeast cells

4.2.1 Single-molecule localization

I acquired data on single R-state mEos3.2 molecules with our custom-built SMLM using a 405-nm laser intensity of 1 W/cm^2, a 561-nm laser intensity of 1 kW/cm^2, and a frame rate of 50 fps. We localized single molecules with the Python Microscopy Environment (PYME) package (R. Lin, Clowsley, Jayasinghe, Baddeley, & Soeller, 2017), using a threshold of 0.6 for event detection computed from the estimated pixel signal-to-noise ratio (SNR). I corrected pixel-dependent noise with maps generated from dark camera frames. I measured the number of photons from single R-state mEos3.2 molecules in each 20-ms frame between frames 5,000 and 10,000 only, since the R-state molecules before frame 5,000 were too dense for localization and most were bleached after frame 10,000.

4.2.2 Photon counts from single red-state mEos3.2 molecules in and fixed *S. pombe* cells

To assess the effects of fixation and the imaging buffer on mEos3.2 photophysics under SMLM conditions, I compared the photon counts of single R-state mEos3.2 molecules per frame in live and fixed yeast cells (Fig. 4.4) under SMLM imaging conditions with a frame rate of 50 fps and a 561-nm laser intensity of 1 kW/cm^2. I localized the single R-state molecules in each frame and measured their photon counts when the density of the R-state molecules was sparse enough for localization. The mean photon counts per frame from single R-state mEos3.2 molecules in live cells and fixed cells imaged in the Tris8.5-DTT buffer were identical (P = 1.000), and higher than the counts in fixed cells

imaged in the EMM5S medium at pH 5.5 (P = 0.007, Fig.4.4, inset). Therefore, the higher brightness per frame of R-state mEos3.2 molecule in the fixed cells in Tris8.5-DTT buffer can improve localization precision (Deschout et al., 2014).

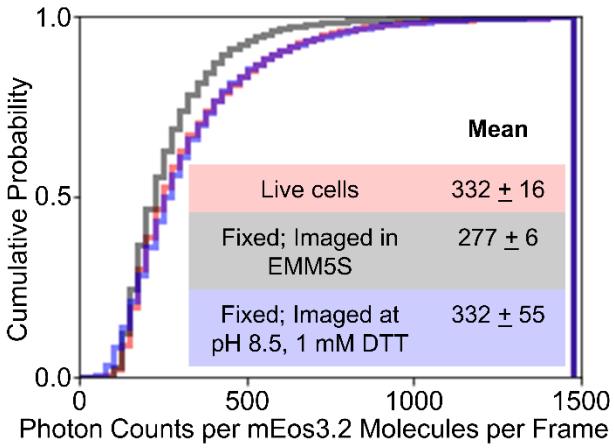

Figure 4.4: The effect of fixation and imaging buffer on photon counts from mEos3.2 by single molecule localization microscopy (SMLM).

SMLM imaging of cytoplasmic mEos3.2 in *S. pombe* cells with continuous illumination at 405 nm (1 W/cm^2) and 561 nm (1 kW/cm^2) under 3 conditions: live cells (red), cells fixed with 2% formaldehyde in EMM5S medium for 30 min and mounted in EMM5S synthetic medium (black) or mounted in Tris8.5-DTT buffer (blue). Four FOVs of 40 µm x 40 µm were taken over time at 50 fps for 15,000 frames for each condition. All emission bursts between frame 5,000 and 10,000 were localized to measure the photon counts from single red mEos3.2 molecules in each 20-ms frame, when the mEos3.2 molecules were sparse enough for Gaussian center fitting. The curves show the cumulative probability distribution of the photon counts of single mEos3.2 molecules in each 20-ms frame under all three conditions. Inset: The table reports the mean number of photons (± standard deviation between the 4 FOVs) emitted by single mEos3.2 molecules in each 20-ms frame under the three conditions. About 2 – 5 x 10^5 emission bursts were recorded for the histogram.

4.3.2 Discussion

The Tris8.5-DTT buffer not only maintained the photon counts of single R-state mEos3.2 molecules in each frame (Fig. 4.4) but also reduced the cellular autofluorescence compared with fixed cells in EMM5S medium (Fig. 4.1E, H). This is crucial for SMLM imaging, where the signal-to-noise ratio is important for obtaining high

localization precision and consequently resolution (Y. Lin et al., 2015). Thus, we recommend using the Tris8.5-DTT buffer for imaging fixed yeast cells with mEos3.2 and conducting more single-molecule experiments for SMLM applications.

4.3 Insights for optimizing laser intensities to image mEos3.2

My quantitative measurements provide guidance for selecting laser intensities to image proteins tagged with mEos3.2. Maximizing the red fluorescence signal of mEos3.2 while maintaining a relatively low level of autofluorescence background is the key to optimize imaging quality. Higher signal-noise-ratios can increase localization precision and thus the resolution in SMLM (Deschout et al., 2014). For SMLM, it is crucial to control the density of active fluorophores, so that they are sparse enough for localization but also dense enough to image quickly. The density of active fluorophores can be regulated by changing the rates of photoconversion and photobleaching. High laser intensities are usually used for fast SMLM imaging in fixed samples (Y. Lin et al., 2015).

Higher 405-nm illumination intensity had four effects on SMLM image quality: (1) it decreased $\overline{R_s}$ under low average 561-nm laser intensity of ~ 0.3 W/cm^2 (Fig. 4.3M), but the effect was not obvious under high 561-nm laser intensity of 1 kW/cm^2 (Fig. 4.3O); (2) it increased background autofluorescence (Fig. 4.1B, E, H), especially in live cells (Fig. 4.1B); (3) it increased k_{act} (Fig. 4.3E); and (4) it increased k_{bl} (Fig. 4.3I, K). One may ramp up 405-nm laser intensity while imaging a field of view to increase k_{act} and compensate for the loss of bleached molecules. However, high 405-nm laser intensities can potentially decrease SMLM imaging quality in two ways: increasing

autofluorescence can compromised accurate localization; and rapid photobleaching decreases $\overline{R_s}$, potentially decreasing total number of localizations.

The time-integrated signal $\overline{R_s}$ increased with 561-nm laser intensity (Fig. 4.3N), reached a maximum and decreased (Fig. 4.3P) with the peaks for live and fixed cells at different 561-nm laser intensities. The 561-nm laser intensity had less impact on $\overline{R_s}$ from fixed cells in the imaging buffer at pH 8.5 with 1 mM DTT than live cells and fixed cells in EMM5S. Therefore, imaging fixed cells in the alkaline imaging buffer with DTT will be faster with higher 561-nm laser intensity, while the imaging quality is maintained as $\overline{R_s}$ will be largely unchanged. For time-lapse imaging of dynamics in live cells, low 561-nm laser intensity can avoid rapid photobleaching and a huge decrease in $\overline{R_s}$, which can avoid reducing the total number of localizations and tracking times of molecules of interest. The photoconversion (Fig. 4.3H) and photobleaching rates (Fig. 4.3L) also increased at high 561-nm laser intensities. Thus, one might need to use a lower 405-nm laser intensity to achieve an optimal molecule density when using a higher 561-nm laser intensity.

4.4 Insights for quantitative SMLM application of mEos3.2

Several variants of EosFP fluorescent proteins are used for SMLM in live and fixed cells (Fricke et al., 2015; Puchner et al., 2013; Y. Zhang, Lara-Tejero, et al., 2017). My work provides insight on comparing quantitative SMLM measurements in live and fixed yeast cells. The time-integrated signal ($\overline{R_s}$) contains information of both the brightness per single fluorescent molecule and the total number of molecules able to fluoresce in the

structure of interest. The single-molecule brightness also affects the number of mEos3.2 localizations, as only molecules emitting more than a threshold number of photons in each frame are counted (R. Lin et al., 2017). Under SMLM imaging conditions (Fig. 4.3O), $\overline{R_s}$ measurements differed in live cells and fixed cells in the Tris8.5-DTT buffer, so they cannot be used for direct comparisons. However, the photon counts from single mEos3.2 emission bursts in each SMLM frame were similar in live cells and fixed cells (Fig. 4.4), so the same analysis thresholds can be used for single-molecule localizations. Combining the time-integrated signal $\overline{R_s}$ (Fig. 4.3O) and photon counts (Fig. 4.4, inset) suggests that fixation and the imaging buffer likely affect the photophysics of single R-state mEos3.2, likely due to the oxidation-reduction environment. Adding reducing thiol MEA and removing oxygen from the imaging buffer have been reported to increase the number of blinking cycles of R-state mEos2 in fixed mammalian cells (Endesfelder et al., 2011) and of purified mEos3.2 (Baldering et al., 2019).

Chapter 5: New intermediate dark state of mEos3.2

To investigate the effects of 405-nm and 561-nm illumination separately, I alternated periods of 405-nm and 561-nm illumination for multiple cycles.

5.1 Experimental set-up

For experiments with alternating 405 and 561-nm laser illumination on point-scanning confocal microscopy, the 561-nm laser scanned the FOV for 10 cycles followed by 405-nm laser illumination for 5 cycles with either no break or a 2 min break between the 405-nm period and the following 561-nm illumination period. The laser powers at the sample were 56 μW at 405 nm and 37 μW at 561 nm. This procedure was repeated 7 times. I increased the temporal resolution by reducing the pixel number in the 85 x 85 μm FOV to 128 x 128 (640 nm pixel size) with a pixel dwell time of 3.39 μs. This approach reduced the total exposure time for each Z-stack to 1.05 s (3.39 μs x 128 x 128 x 19). These 3D stacks were collected with 40 cycles of 561-nm illumination followed by 20 cycles of 405-nm irradiation without breaks between the 405-nm and 561-nm illumination periods. The Z-stacks were acquired at a rate of approximately 5 Z-stacks per minute due to the scanning overhead. This procedure was repeated 7 times.

For widefield fluorescence imaging, a custom-written LABVIEW program (credit to Kevin Hu in the Bewersdorf lab) was used to control the lasers for alternating 405-nm and 561-nm illumination.

5.2 Surprising transient increases of the red mEos3.2 fluorescence signal with only 561-nm illumination

Surprisingly, the signal during the 561-nm illumination period (except for the first one without prior 405-irradiation) rose transiently above the initial value despite the 405-nm illumination being switched off (Fig. 5.1A). After peaking during the fifth cycle of each 561 nm illumination period, the signal decreased due to photobleaching (Fig. 5.1A, B). The signal during each 561-nm illumination period (except for the first one without prior 405-nm illumination) followed similar time courses (Fig. 5.1B). These transient increases in the fluorescence signal also occurred using alternating widefield illumination conditions (Fig. 5.2).

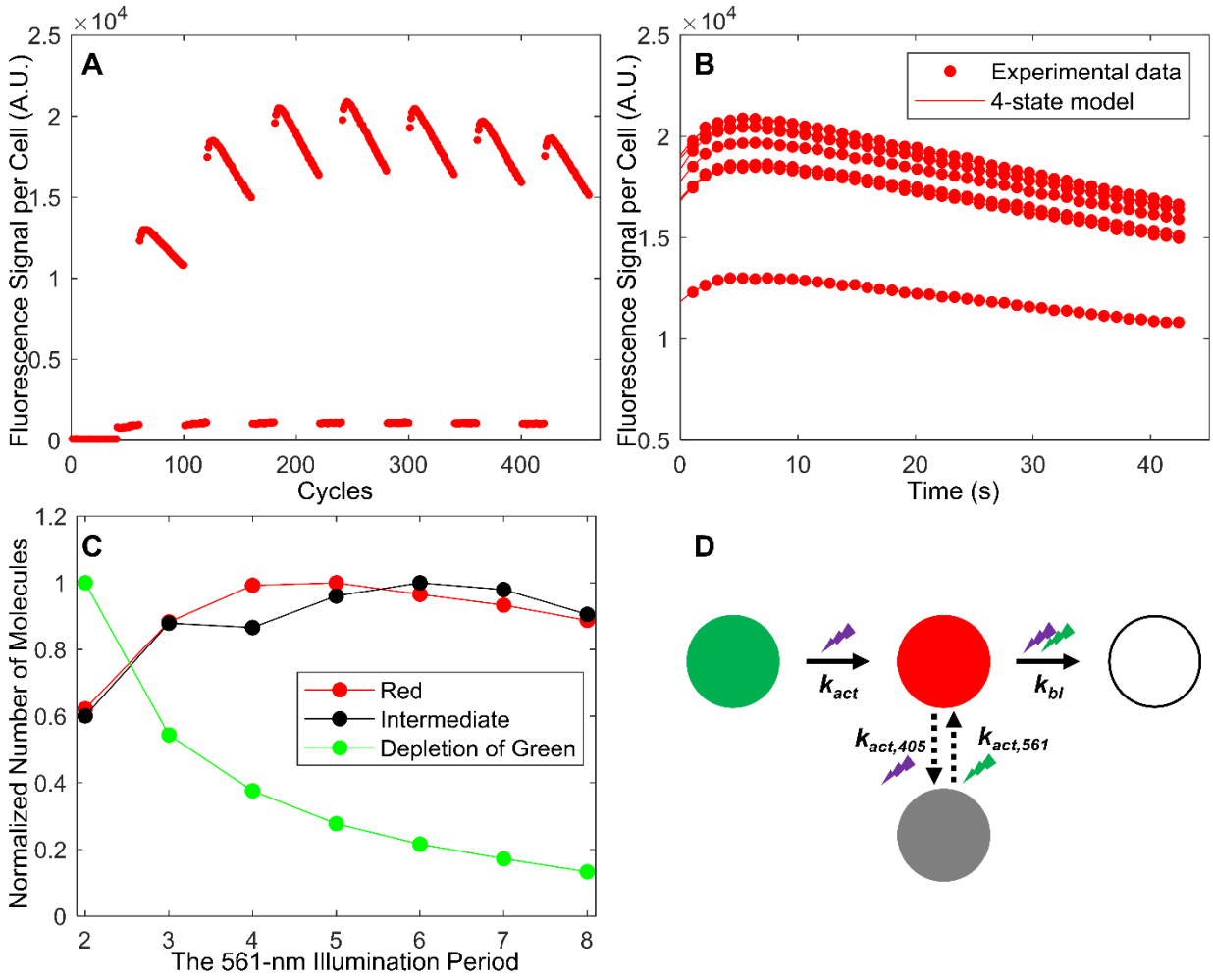

Figure 5.1: Intermediate-state mEos3.2 converts from red-state by 405-nm irradiation and back to red-state by 561-nm illumination

(A) Time courses of the fluorescence signal per live *S. pombe* cell expressing mEos3.2 and subjected to alternating illumination by point-scanning confocal microscopy at 561 nm (37 μW) for 40 cycles followed by illumination at 405 nm (56 μW) for 20 cycles. Illumination at 561 nm increased the fluorescence signal beyond the start of the 561-nm illumination period after each period of 405-nm illumination. (B) Comparisons of the time courses of the fluorescence signals during 7 periods with 40 cycles of 561-nm illumination (not including the first 561-nm illumination period before any 405-nm irradiation) from panel A. Eq. 5.7 of the 4-state model in panel D (lines) was fit to these time courses (dots) to determine rate constants giving the best fit. The mean activation rate constant ($k_{act,561}$) from the I-state to the R-state is 0.34 s^{-1} (SD: 0.02). (C) Normalized number of red (red), intermediate (black) and green molecules (green) at the beginning of each 561-nm illumination period. The normalized number of red and intermediate molecules were estimated from fitting the Eq. 5.7 of the 4-state model to the time courses of fluorescence signal during the 7 periods of 561-nm illumination in Panel B. The depletion of green molecules was estimated from subtracting the fluorescence signal at the last cycle of the previous 561-nm illumination period from the signal at the first cycle of the previous 561-nm

illumination period. (D) Four-state model for mEos3.2 photoconversion and bleaching. Illumination at 405 nm photoconverts mature mEos3.2 molecules from the G-state to the R-state with a photoconversion rate constant of. A subpopulation of the R-state molecules enters an intermediate dark state (gray circle) by 405-nm irradiation, and 561-nm illumination converts the I-state mEos3.2 molecules to the R-state with a rate constant of $k_{act,561}$. Illumination at both wavelengths photobleaches red mEos3.2 molecules with a rate constant of k_{bl}.

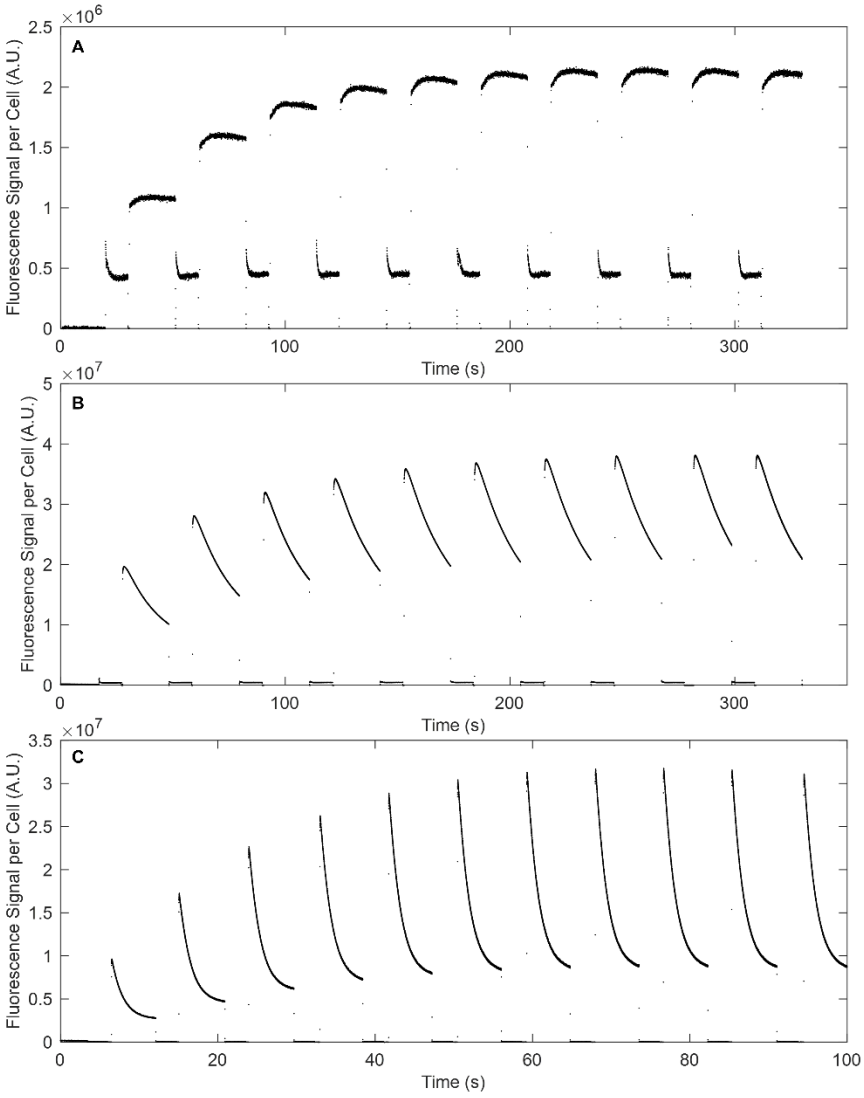

Figure 5.2: The intermediate state that converts to the red fluorescent state under widefield illumination at 561 nm.

Time courses of the fluorescence signal per live *S. pombe* cell expressing mEos3.2 and subjected to alternating widefield illumination by at 561 nm followed by illumination at 405 nm at 1 W/cm^2. Illumination at 561 nm increased the fluorescence signal beyond the start of the 561-

nm illumination period after each period of 405-nm illumination. Conditions: (A) 561 nm laser intensity = 1 W/cm^2, 50 fps; 20 s for each 561-nm illumination period, followed by 10 s for each 405-nm illumination period (B) 561 nm laser intensity = 10 W/cm^2, 50 fps; 20 s for each 561-nm illumination period, followed by 10 s for each 405- nm illumination period (C) 561 nm laser intensity = 100 W/cm^2, 500 fps; 5 s for each 561-nm illumination period, followed by 2.5 s for each 405- nm illumination period.

5.3 Four hypotheses to explain the transient increases

I considered four hypotheses to explain these transient increases in the fluorescence signal. First, illumination at 561 nm might photoconvert G-state mEos3.2 to the R-state directly, but I failed to observe comparable activation with the same 561-nm illumination intensity at ~ 0.5 W/cm^2 alone (Fig. 5.3B, and first 40 cycles of 561-nm irradiation in Fig. 5.1A). A second hypothesis is that the first-order photoconversion reaction is slow after absorption of 405-nm photons, delaying accumulation of R-state molecules. I ruled out this mechanism by adding a 2-min pause between each 405-nm illumination period and the following 561-nm illumination period. The transient increase in the fluorescence signal was still observed, ruling out this hypothesis as a dominant effect (Fig. 5.3A). Similarly, I could rule out a third hypothesis that the observed increase in the fluorescence signal over the course of 561-nm illumination was related to protein maturation or similar live-cell phenomena by observing the same effect in fixed cells (Fig. 5.3C).

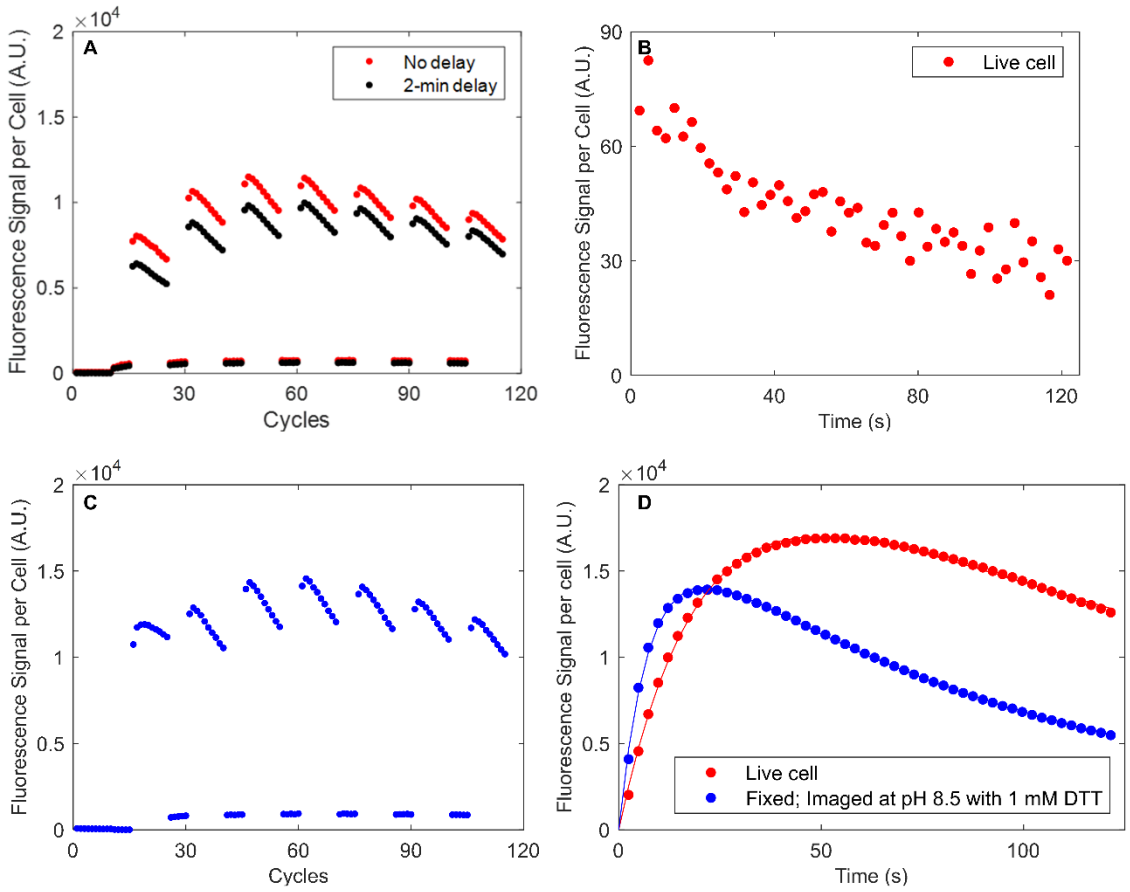

***Figure 5.3: The intermediate state that converts to the red fluorescent state by 561-nm illumination.**

(A) Time courses of the fluorescence signal per live *S. pombe* cell expressing mEos3.2 and subjected to alternating illumination by point-scanning confocal microscopy at 561 nm (37 μW) for 10 cycles followed by illumination at 405 nm (56 μW) for 5 cycles. Illumination at 561 nm increased the fluorescence signal beyond the start of the 561-nm illumination period after each period of 405-nm illumination. The red dots are data collected from live cells with no delay between the periods of illumination at 405 nm and 561 nm, while the black dots are data collected from live cells with a 2-min break after each period of 405-nm illumination before the following period of 561-nm illumination. Fitting Eq. 5.7 of the 4-state model in panel D fit to these time courses of the fluorescence signals during 7 periods with 10 cycles of 561-nm illumination gave the mean activation rate constant ($k_{act,561}$) from the I-state to the R-state of 0.27 s^{-1} (SD: 0.03) for the experiment with no delay between the 405-nm and 561-nm illumination cycle (red), and of 0.28 s^{-1} (SD: 0.03) for the experiment with 2-min breaks (black). (B) Time course of the fluorescence signal per cell expressing mEos3.2 and illuminated only at 561 nm (37 μW). (C) Time course of the fluorescence signal per cell expressing mEos3.2, fixed with 2% formaldehyde for 30 min, and imaged in the buffer at pH 8.5 with 1 mM DTT under alternating illumination by point-scanning confocal microscopy at 561 nm (37 μW) for 10 cycles followed by illumination at 405 nm (56 μW) for 5 cycles. The mean activation rate ($k_{act,561}$) of mEos3.2 from the I-state to the R-state is 0.27 s^{-1} (SD: 0.03). (D) Time courses of the fluorescence signal per cell from live *S. pombe* cells and cells fixed with 2% formaldehyde in

EMM5S medium for 30 min and imaged in 50 mM Tris-HCl buffer at pH 8.5 with 1 mM DTT and illuminated simultaneously at 405 nm (56 μW) and 561 nm (37 μW). Eq. 1.7 of the 3-state model (line) was fit to the time courses of the fluorescence signal per cell (red or blue dots). The rate constants of photoconversion from the G-state to the R-state (k_{act}) were 0.050 s^{-1} (95% CI: 0.048-0.051) for live cells (red) and 0.131 s^{-1} (95% CI: 0.127-0.134) for fixed cells (blue).

The fourth hypothesis is that 405-nm illumination leaves a subpopulation of mEos3.2 molecules in an intermediate (I) state that requires 561-nm illumination to convert to the fluorescent R-state. To test this hypothesis, I added a fourth I-state to the model (Fig. 5.1D) and built a 4-state mathematical model to test this hypothesis.

5.4 Four-state mathematical model

Experiments with alternating illumination at 405 nm and 561 nm revealed a potential fourth intermediate (I) state of mEos3.2 molecules (Fig. 5.1). Illumination at 405 nm converts mEos3.2 molecules in the G-state into the R-state and molecules in the G- and/or R-state into the I-state. Irradiation at 561 nm converts the mEos3.2 molecules from the I-state to R-state with an activation rate constant of $k_{act,561}$. R-state molecules are photobleached with a bleaching rate constant of k_{bl}. During a 561-nm illumination period after a previous 405-nm illumination period, I assumed that no mEos3.2 molecules in the G- and/or R-state converted to the I-state and I-states molecules were not photobleached. The rates of change in the numbers (n) of I-, R-, and B-state mEos3.2 molecules are described by the following differential equations:

$$\frac{dI_n(t)}{dt} = -k_{act,561} I_n(t) \qquad (5.1)$$

$$\frac{dR_n(t)}{dt} = k_{act,561} I_n(t) - k_{bl} R_n(t) \qquad (5.2)$$

$$\frac{dB_n(t)}{dt} = k_{bl}R_n(t) \qquad (5.3)$$

I defined the total number of mEos3.2 molecules, i.e. the sum of molecules in the I-, R- and B-states in a cell, after the previous 405-nm irradiation as S_n. I further defined t = 0 as the time at which 561-nm illumination starts and assumed that S_n is constant during the 561-nm illumination period, since the 405-nm laser was off and conversion of molecules to the I-state by 561-nm light is negligible. I further assume that the number of molecules in the different states at the beginning of the 561-nm illumination period is $R_n(t = 0) = R_{n,0}$, $I_n(t = 0) = S_n - R_{n,0}$, and $B_n(t = 0) = 0$. Solving the system of differential equations analytically resulted in the following equations for the number of I-, R-, B-state molecules changing over time:

$$I_n(t) = \left(S_n - R_{n,0}\right)e^{-k_{act,561}t} \qquad (5.4)$$

$$R_n(t) = \frac{1}{k_{bl}-k_{act,561}}\left[\left(S_n - R_{n,0}\right)k_{act,561}e^{-k_{act,561}t} - \left(S_n k_{act,561} - R_{n,0}k_{bl}\right)e^{-k_{bl}t}\right] \qquad (5.5)$$

$$B_n(t) = \frac{S_n}{k_{bl}-k_{act,561}}\left[k_{bl}(1 - e^{-k_{act,561}t}) - k_{act,561}(1 - e^{-k_{bl}t})\right]$$

$$+ \frac{R_{n,0}k_{bl}}{k_{bl}-k_{act,561}}(e^{-k_{act,561}t} - e^{k_{bl}t}) \qquad (5.6)$$

Eq. 5.5 describes how the number of red mEos3.2 molecules in a cell (R_n) changes during the period of 561-nm illumination. Multiplying both sides of Eq. 5.5 by ε_f gives Eq. 5.7 that describes how the fluorescence signal per cell changes over time during this period:

$$R_s(t) = \frac{1}{k_{bl}-k_{act,561}}\left[\left(S_n\varepsilon_f - R_{n,0}\varepsilon_f\right)k_{act,561}e^{-k_{act,561}t} - \left(S_n\varepsilon_f k_{act,561} - R_{n,0}\varepsilon_f k_{bl}\right)e^{-k_{bl}t}\right]$$

(5.7)

I estimated S_n x ε_f, $R_{n,0}$ x ε_f, $k_{act,561}$, and k_{bl} using Levenberg-Marquardt nonlinear least squares regression to fit Eq. 5.7 to the time courses of the fluorescence signal per cell during the 561-nm illumination period. We calculated the mean and standard deviation of the activation rate constant ($k_{act,561}$) for converting mEos3.2 molecules from I- to R-state by 561-nm irradiation from averaging the 7 periods of 561-nm irradiation for each condition.

5.5 New intermediate dark state of red-state mEos3.2

Whether this I-state is populated from the R-state or G-state mEos3.2 molecules does not affect Eqs. 5.1-5.7, which only considers the period of 561-nm illumination when conversion into the I-state is negligible. Eq. 5.7 of my 4-state model fits closely the time courses of mEos3.2 fluorescence signal during each 561-nm illumination period (Fig. 5.1B). The best fits gave an average activation rate constant for conversion from the I-state to R-state by 561-nm irradiation $k_{act,561}$ = 0.34 s^{-1} (SD: 0.02 s^{-1}) (Fig. 5.1B), which is 4-fold higher than the rate constant for photoconversion from the G- to R-state k_{act} = 0.050 s^{-1} (95% CI: 0.048- 0.051 s^{-1}), as measured with simultaneous 405-nm and 561-nm illumination (Fig. 5.3D).

I compared the number of I-state molecules changing over time with the respective G- and R-state populations (Fig. 5.1C). The normalized time course of the I-state

molecules was similar to R-state molecules and distinctly different from the G-state molecules, strongly suggesting that the I-state is populated from the R-state molecules.

Overall, these experiments revealed that a subpopulation of the R-state molecules is converted to the I-state by 405-nm illumination but can be converted back to the R-state by 561-nm illumination (Fig. 5.1D). I did not detect any spontaneous conversion from I- to R-state or R- to I-state over the 2-minute breaks (Fig. 5.3A). However, for experiments with simultaneous illumination at both 405 nm and 561 nm, Eq. 1.7 of my simplified 3-state model (without considering the I-state) fully accounted for the time courses of fluorescence signal per cell under all the conditions (Fig. 2.1B, 3.1C).

5.6 Discussion

My alternating illumination experiments (Fig. 5.1) revealed that 405-nm irradiation drives some R-state molecules into the I-state ("off-switching"), which can be reconverted back to the R-state ("on-switching") by 561-nm illumination. De Zitter *et al.* reported a similar observation, describing that 561-nm illumination converts the mEos3.2 derivative mEos4b from a long-lived dark state to the red state in response to 561-nm illumination (De Zitter et al., 2019). The rate of this conversion increased with 561-nm laser intensity and this conversion could also be induced by 405-nm irradiation (De Zitter et al., 2019). The newly discovered mEos3.2 I-state is unlikely to be the long-lived dark state as described for mEos4b (De Zitter et al., 2019), as only illumination at 561 nm (but not at 405 nm) converts our I-state molecules to the R-state (Fig. 5.1, Fig. 5.2). Our results established the "positive" switching behavior (off-switching by 405-nm and on-switching by 561-nm illumination) of red mEos3.2 in addition to the previously reported "negative"

switching behavior (off-switching by 561-nm and on-switching by 405-nm illumination) (De Zitter et al., 2019; Lee et al., 2012). Further structural studies and analysis of the pH-dependence of the switching behavior should provide insight into the nature of this intermediate state.

The “positive” switching behavior could potentially affect the number of detected blinks of red mEos3.2 during SMLM, thus affecting counting. For example, ramping up 405-nm laser intensity to compensate for bleached molecules during SMLM imaging might decrease the on-time and induce more blinking of R-state mEos3.2. To simplify the switching photophysics, one might use a pulsed 405-nm illumination for photoconversion followed by a period of 561-nm excitation to minimize off-switching induced by 405-nm irradiation.

Chapter 6: Quantitative SMLM and future work

In this chapter, I summarized the progress I have made using homo-oligomeric protein clusters fused to mEos3.2 with known numbers of molecules per cluster as internal standards for counting molecules with SMLM. I aim to use the internal calibration standards to generate a calibration curve that can convert the number of localizations to the number of mEos3.2-fused proteins in subcellular structures, so that SMLM can be a quantitative tool to count molecules in cells. Once established, the calibration curve can automatically correct for the undercounting problem due to slow FP maturation and the overcounting problem due to “blinking”.

6.1 Experimental and analysis pipeline

I aim to measure the number of localizations per mEos3.2 tagged proteins in well-defined stable structures with SMLM, using standard protein oligomers with a known number of mEos3.2 molecules as internal calibration standards.

6.1.1 Construction of fluorescent fusion proteins

I used the pFA6a-mEos3.2-KanMX6 plasmid to integrate the coding sequence of mEos3.2 such that it would reside at the C-termini of proteins expressed from their endogenous loci. For standard proteins with exogenous origin, I generated pJK148-p41nmt1-mEos3.2-ADHterm1, pJK148-P3nmt1-mEos3.2-AHDterm1, and pFA6a-NatMX6-p41nmt1-mEos3.2-ADHterm1 plasmids. I used PCR to amplify the coding sequence of mEos3.2 to replace the mEGFP coding sequence using NEBuilder Assembly. Coding sequences of these calibration proteins were inserted into the above

plasmids with NEBuilder Assembly. Strains were constructed by PCR-based or linearized plasmid based gene targeting (Bähler et al., 1998) and confirmed by PCR, sequencing, and microscopy. Fusion proteins are either expressed from their chromosomal loci or from the *leu1* locus with a *nmt1* promoter. All the plasmids and strains are listed in Table 6.1 and Table 6.2.

6.1.2 Sample preparation for SMLM imaging

S. pombe cells expressing standard proteins fused to mEos3.2 were grown to the exponential phase at 25 °C in YE5S-rich liquid medium in 50-mL flasks in the dark before switching to EMM5S-synthetic medium ~12-18 hours before imaging to induce expression of the fusion proteins from the *nmt1* promoter and to reduce the cellular autofluorescence background. Cells were fixed by mixing an equal volume of fresh, room temperature 4% formaldehyde aqueous solution (Electron Microscopy Sciences, Hatfield, PA) with the cell culture and shaking at 150 rpm at 25° C for 15 min. The cells were pelleted by centrifugation at 3,000 rpm for 30 s and washed by pelleting in PBS or the 'Tris8.5-DTT' buffer, and then resuspended in the PBS or 'Tris8.5-DTT' buffer. Concentrated cells in 5 µL were mounted on a thin layer formed from 35 µL of 25% gelatin (Sigma-Aldrich; G-2500) in the PBS or the Tris8.5 buffer. The slides were sealed with Valap or dental glue for imaging.

6.1.3 SMLM data acquisition and analysis

SMLM imaging was performed with a custom-built single-molecule localization microscope (SMLM) based on a Leica DMi8 stand with widefield epi-illumination, a 63x/1.47 NA oil-immersion objective, and a band pass filter to collect emission

fluorescence in the 584-676 nm wavelength range. Samples were illuminated at both 405 nm and 561 nm and imaged with an sCMOS camera (Hamamatsu ORCA-Flash4.0 V2). The 405-nm laser intensity was ramped up manually from ~0.1 to 0.5 W/cm^2 to compensate for bleached molecules. I used 100 fps as the frame rate and ~ 1 kW/cm^2 as the 561-nm laser intensity. I localized single molecules with the Python Microscopy Environment (PYME) package (R. Lin et al., 2017), using a threshold of 0.7 for event detection computed from the estimated pixel signal-to-noise ratio (SNR). I corrected pixel-dependent noise with maps generated from dark camera frames. To aid the visualization of the 2D histogram image of 5-nm pixels, I convolved the images with a 2D Gaussian kernel (σ = 1.5*localization error in the x direction).

6.1.4 Localization measurements

Localizations separated by <50 nm and temporally separated by 1< frame are assumed to stem from the same emission burst and were combined together. I used DBSCAN clustering (X. W. Xu, Ester, Kriegel, & Sander, 1998) and manual segmentation to find the cluster of standard proteins in the yeast cells and measured the number of localizations per cluster.

6.1.5 Geometric distribution and negative binomial distribution for the blinking events

After photoconversion, the red-state EosFP and its derivatives can enter the transient dark state and come back to the fluorescent state again, which is commonly referred as “blinking” (Lee et al., 2012; Rollins et al., 2015). Fricke *et al.* showed that the number of times a single FP blinks after photoconversion resembles a geometric distribution

$P_p(N_{blinks,i}) = p(1-p)^{N_{blinks}}$ (Fricke et al., 2015). Here, p is the probability that the FP does not blink, which means that the red-state FP does not go into the transient dark state after photoconversion but photobleaches after it was detected in the red channel. N_{blinks} equals the number of localizations per FP minus one, as a FP with only 1 localization does not blink. In the case of oligomerization, the number of molecules able to fluoresce in the cluster N is larger than one. The distribution of blinking events follows a negative binomial distribution $P_{N,p}(N_{blinks}) = \binom{N+N_{blinks}-1}{N-1} p^N (1-p)^{N_{blinks}}$ (Fricke et al., 2015).

6.2 Tested internal calibration standards

The key to generating a good calibration curve is to choose and establish a series of robust and reproducible calibration standards that can cover a wide range of number of molecules per well-defined cluster. The calibration standards I tested follow the following criteria: 1) The proteins can self-assemble into stable structures with known number of molecules characterized by electron microscopy or X-ray crystallography, 2) the proteins localize in the cytoplasm, so that the mEos3.2 FPs fused to the calibration standards and the target are in similar microenvironment, 3) there is little or no exchange and interaction between the standards and the cytoplasm, so that the number of the molecules per cluster has low biological variation , and 4) the calibration standards can be expressed and applied to other organisms, so that the calibration curve can a more universally applicable method for counting molecules with SMLM (Fig. 6.1).

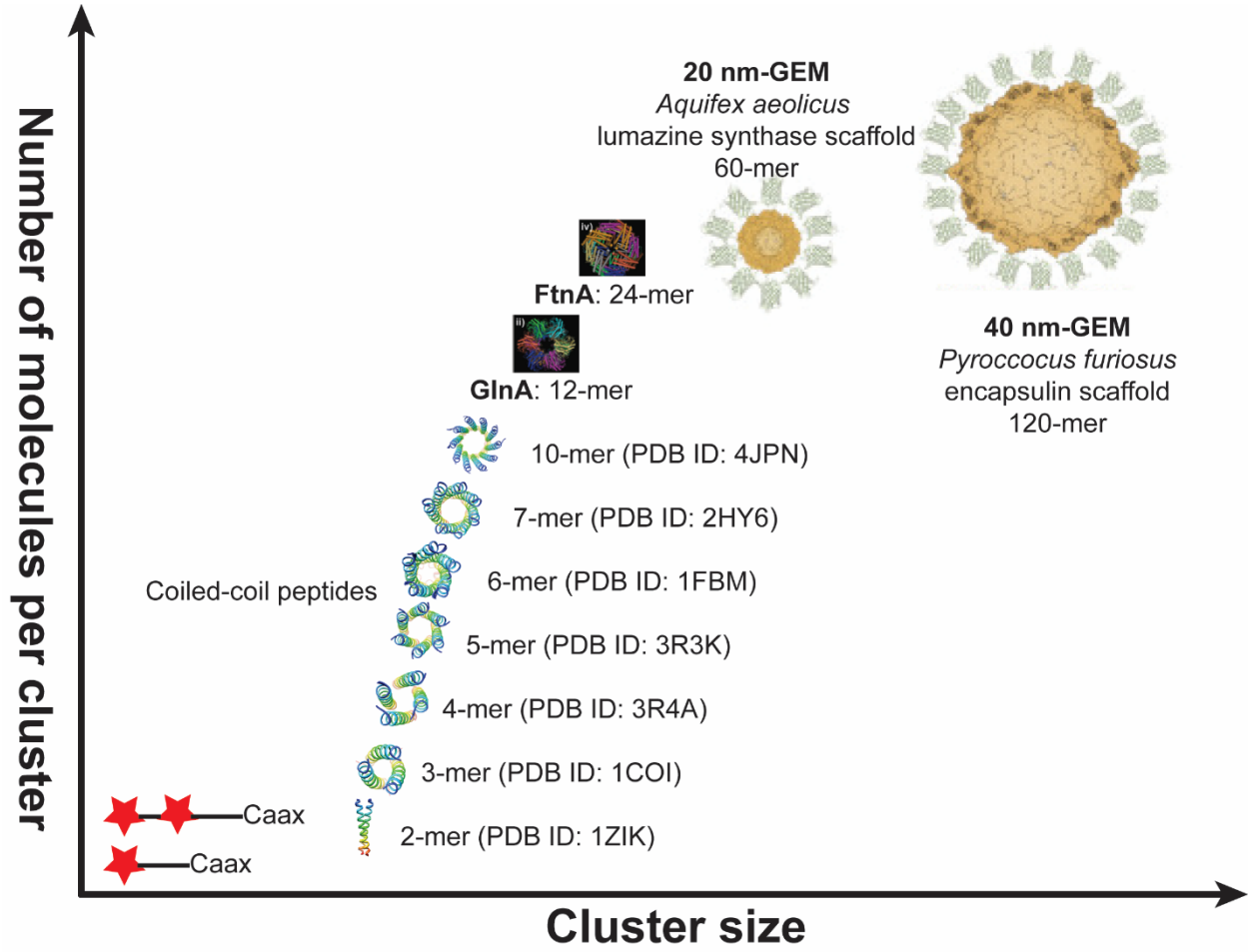

Figure 6.1 Summary of the tested internal calibration standards

The figure lists all the internal calibration standards that I have tested in *S. pombe* cells, including single molecules of mEos3.2 (n = 1), concatenated mEos3.2 dimers (n = 2), and mEos3.2 molecules fused to a series of coiled-coil peptides (n = 2, 3, 4, 5, 6, 7, 10) (Gonzalez, Woolfson, & Alber, 1996; Guo et al., 1998; Liu et al., 2006; Malashkevich, Kammerer, Efimov, Schulthess, & Engel, 1996; O'Shea, Klemm, Kim, & Alber, 1991; Ogihara, Weiss, Degrado, & Eisenberg, 1997; Sun et al., 2014; Zaccai et al., 2011) and anchored to the plasma membrane by a CAAX sequence (Hancock, Cadwallader, Paterson, & Marshall, 1991), and protein oligomers fused to mEos3.2: *E. coli* glutamine synthetase GlnA (n =12) and ferritin FntA (n = 24) (Finan, Raulf, & Heilemann, 2015), and two engineered proteins called GEMs (Delarue et al., 2018), *Aquifex aeolicus* lumazine synthetase scaffold (n = 60) and *Pyroccocus furiosus* encapsulin scaffold (n = 120).

6.2.1 Nucleoporin nup85 (n=24)

I first attempted to use the endogenous nucleoporin protein Nup85 as the internal calibration standard (Fig. 6.2). Nuclear pore complexes (NPCs) have been used

reference standards for quantitative SMLM in mammalian cells and budding yeast cells (Thevathasan et al., 2019). Based on the cryo-EM structure, NPC structure in fission yeast *S. pombe* is asymmetric with two concentric Y-complex rings (each contains 8 Y-complexes) on the nuclear side and 8 individual cytoplasmic Y-complex on the cytoplasmic side (Zimmerli et al., 2020). Each Y-complex contains a copy of the Nup85 protein, thus each *sp*NPC contains 24 copies of Nup85 in total. I endogenously tagged the Nup85 with mEos3.2 in fission yeast (strain sHMS037) and imaged the fixed cells expressing Nup85-mEos3.2 on SMLM. However, imaging and finding well-separated individual NPCs in *S. pombe* is challenging because it is hard to capture a focal plan in which the NPCs are en face. The spherical nucleus in the fission yeast cells lacks a flat surface to focus on. I tried to create a flat surface for focusing by digesting the cell wall to create protoplasts and then flattening the yeast protoplasts, but the autofluorescence in the cells increased dramatically, presumably due to stress. Next, I attempted to create a more elongated cell to make the NPCs more spread out by incorporating the *cdc25-22* mutation in the genome (strain sHMS044), but the result was still not ideal (Fig. 6.2A). My preliminary clustering analysis using manual segmentation and DBSCAN clustering revealed the mean number of localizations from Nup85-mEos3.2 per *sp*NPC cluster to be ~ 22 (Fig. 6.2B). Therefore, the separation and identification of individual *sp*NPCs makes it challenging to establish the nucleoporin Nup85 in fission yeast cells as a robust calibration standard.

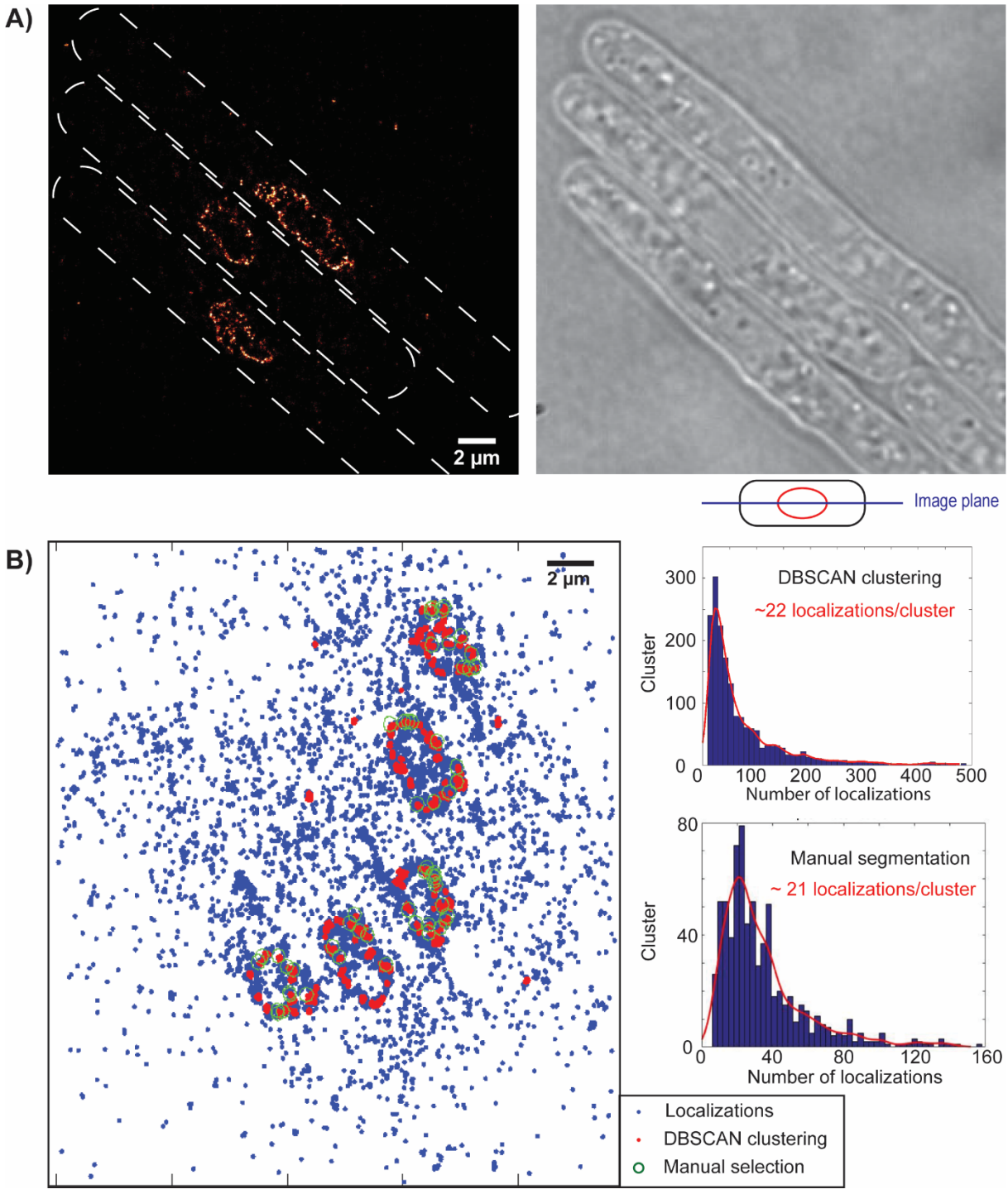

Figure 6.2: Nucleoporin Nup85 as an internal calibration standard for counting molecules in SMLM

(A) 2D-SMLM (100 fps, 561 nm laser intensity at 1 kW/cm^2) and brightfield image of nup85-mEos3.2 in fission yeast cells (sHMS44). (B) Measuring the number of localizations per cluster

using manual segmentation (a circle ROI with ~300 nm radius) or DBSCAN clustering (search radius = 30 nm, minimum cluster size = 8). The mean number of localizations per cluster is ~22.

6.2.2 mEos3.2 monomers (n = 1) and concatenated dimers (n = 2)

I generated strains with a single molecules of mEos3.2 (n = 1, strain sHMS039) and a concatenated mEos3.2 dimers (n = 2, strain sHMS045) targeted and anchored to the plasma membrane through a CCAAX sequence (Hancock et al., 1991). The coding sequences mEos3.2-CCAAX and 2xmEos3.2-CCAAX fusion proteins were integrated into the fission yeast genome at the *leu1* locus and expressed from a medium strength thiamine-repressible promoter *P41nmt1*. SMLM images showed that both the mEos3.2 monomers and dimers localized to the plasma membrane (Fig. 6.3 A, B). Using the preliminary datasets, I generated distributions for the number of blinks (= localizations – 1) of spatially clustered mEos3.2 (distance < 50 nm) for both strains. For mEos3.2-CCAAX, the distribution of blinking events is well described by a geometric distribution $P_p\left(N_{blinks,i}\right) = p(1-p)^{N_{blinks}}$ with the blinking parameter p = 0.85 $\pm$ 0.02 (Fig. 6.3C). For the 2xmEos3.2-CCAAX, the distribution of blinking events follows a negative binomial distribution with N = 1.83 $\pm$ 0.63 when using p = 0.85 as a fixed fit parameter (Fig. 6.3D). As expected, the oligomerization state N of 2xmEos3.2-CCAAX is less than 2, because some mEos3.2 molecules were not mature (Wang et al., 2014) and their photoconversion was incomplete (Avilov et al., 2014).

The preliminary results demonstrated the promise of mEos3.2-CCAAX and 2xmEos3.2-CCAAX as calibration standards. However, the expression level of the mEos3.2-CCAAX and 2xmEos3.2-CCAAX needed to be further repressed to assure that the molecules were well-separated on the membrane. Further, more datasets need to be collected to

validate the robustness and reproducibility of the calibration standards and the fitting of the blinking event distribution.

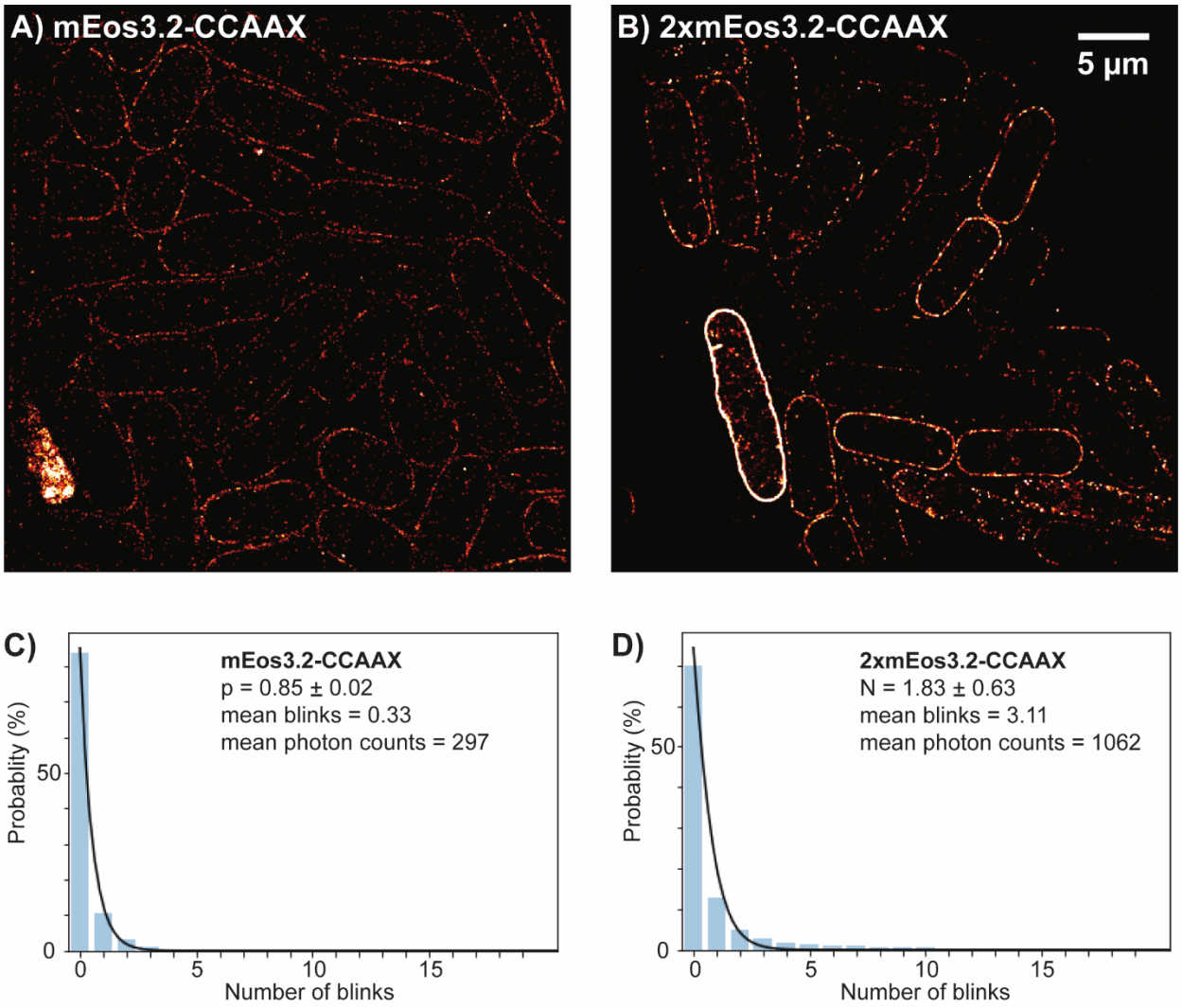

Figure 6.3 mEos3.2 monomers and concatenated mEos3.2 dimers as internal calibration standards

(A) 2D-SMLM images of mEos3.2-CCAAX at the plasma membrane of fixed fission yeast cells sHMS39. (B) 2D-SMLM images of 2xmEos3.2-CCAAX at the plasma membrane of fixed fission yeast cells sHMS45. (C) For mEos3.2-CCAAX the distribution is well approximated by a geometric distribution and yields p = 0.85 $\pm$ 0.02 as the blinking parameter. (D) For 2xmEos3.2-CCAAX, the distribution fits to a negative binomial distribution with N = 1.83 $\pm$ 0.63 as the oligomerization parameter.

6.2.3 *E. coli* ferritin FtnA (n = 24) and glutamine synthetase GlnA (n = 12)

I generated strains expressing mEos3.2 fused to the N-termini of the *E. coli* proteins ferritin FtnA (24-mer) and glutamine synthetase GlnA (12-mer) (Finan et al., 2015). I first attempted to express the fusion proteins from the medium strength promoter *P41nmt1*. However, I did not see any visible expression of either fusion protein. Then I switched to the strong promoter *P3nmt1* to express both fusion proteins. mEos3.2-FtnA was successfully expressed but did not form clear clusters (Fig. 6.4). The localizations are dispersed in the cytoplasm, and no clear clustering of the localizations were observed. Therefore, mEos3.2-FtnA and mEos3.2-GlnA do not seem to be promising internal calibration standards in fission yeast.

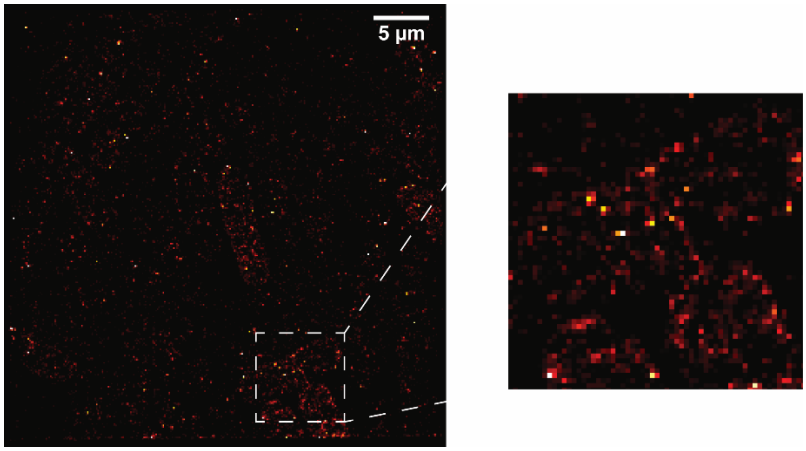

Figure 6.4: mEos3.2-FtnA as internal calibration standard for SMLM in fission yeast cells
2D-SMLM images of mEos3.2-FtnA in fixed fission yeast cells sHMS091. The cells were grown in EMM5S + 1 µM thiamine for 20 hours for expression.

6.2.4 Genetically-encoded multimeric particles (GEMs) (n= 60 or 120)

Genetically encoded multimeric particles (GEMs) can self-assemble into bright, stable fluorescent particles of defined shape and size and were originally designed to probe

cytoplasmic crowding in unperturbed living cells by measuring their diffusion coefficients by single particle tracking (Delarue et al., 2018). GEMs were developed from natural homomultimeric scaffolding domains that self-assembles into icosahedral geometries, including the encapsuling protein from the hyperthermophilic archaeon *Pyrococus furiosus* that assembles into a ~ 40-nm 120-mer and the lumazine synthase enzyme complex from the hyperthermophilic bacterium *Aquifex aeolicus* that assembles into a ~ 20-nm 60-mer (Delarue et al., 2018). I generated fission yeast strains expressing GEM scaffold domains fused with mEos3.2 from the *P41nmt1* promoter. The DNA sequences encoding P41nmt1-GEM-mEos3.2 were inserted at the *leu1* locus in the fission yeast genome through DNA-based gene targeting. Both 40-nm and 20-nm GEMs fused with mEos3.2 form nice clusters, but some higher-order clustering of the single GEM clusters can also be observed (Fig. 6.5). Further clustering and statistical analysis need to be performed to measure the number of localizations per GEM particles for calibration purposes.

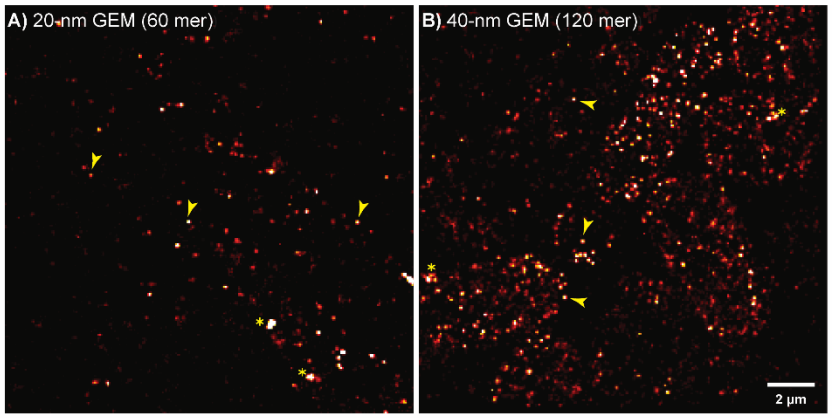

Figure 6.5: 20-nm and 40-nm GEMs as internal calibration standard for SMLM in fission yeast cells

2D-SMLM images of 20-nm GEM (sHMS68) and 40-nm GEMs (sHMS72) fused to mEos3.2 in fixed fission yeast cells. The cells were grown in EMM5S for 24 hours for expression. The arrowheads indicate single GEM particles, while the asterisks indicate higher-order clustering of GEMs.

6.2.5 Coiled-coil peptides (n = 2, 3, 4, 5, 6, 7, 10)

I found a series of coiled-coil peptides that can self-oligomerize parallelly with defined stoichiometries, including the transcription factor GCN4 leucine zipper (n = 2, called "CC2mer") (O'Shea et al., 1991), designed trimeric peptide coil-V_aL_d (n = 3, called "CC3mer") (Ogihara et al., 1997), designed tetrameric peptide CC-Tet based on the GCN4 leucine zipper (n = 4, called "CC4mer") (Zaccai et al., 2011), the oligomerization domain in the cartilage oligomeric matrix protein (COMP) (n = 5, called "CC5mer") (Guo et al., 1998; Malashkevich et al., 1996), a designed hexametric peptide CC-Hex based on CC-Tet (n = 6, called "CC6mer") (Zaccai et al., 2011), a designed heptameric peptide GCN4-pAA based on the GCN4 leucine zipper (n = 7, called "CC7mer") (Liu et al., 2006), and the bacteriophage ΦX174 DNA pilot protein H (n = 10, called "CC10mer") (Sun et al., 2014). I designed constructs with 1 copy (N-terminus), 2 copies (N-terminus), 3 copies (2 copies at N-terminus and 1 copy at C-terminus) or 4 copies (2 copies at N-terminus and 2 copies at C-terminus) of mEos3.2 per peptide and the C-terminal CAAX sequence (Hancock et al., 1991) fused to the coiled-coil peptides (Fig. 6.6A). The fusion proteins were expressed from the *P41nmt1* promoter and the coding sequence of the fusion proteins were inserted at the *leu1* locus in the fission yeast genome. The fusion proteins were successfully expressed and form clusters. However, the lack of cysteine residue before the CAAX sequence prevented the fusion proteins to be anchored successfully to the plasma membrane in some of the strains (Fig. 6.6B). One or two cysteine residues upstream of the CAAX motif can be tagged with palmitic

acid via a labile thioester bond, enable the anchoring to the plasma membrane. Moreover, I could not observe a clear correlation between the expected number of molecules per cluster and the number of localizations per cluster based on preliminary manual analysis (Fig. 6.6C). I suspect that the expression level is too high to resolve single clusters formed by the coiled-coil peptides. I plan to titrate with thiamine to regulate the expression levels. Further clustering and statistical analysis will be needed to measure the number of localizations per cluster.

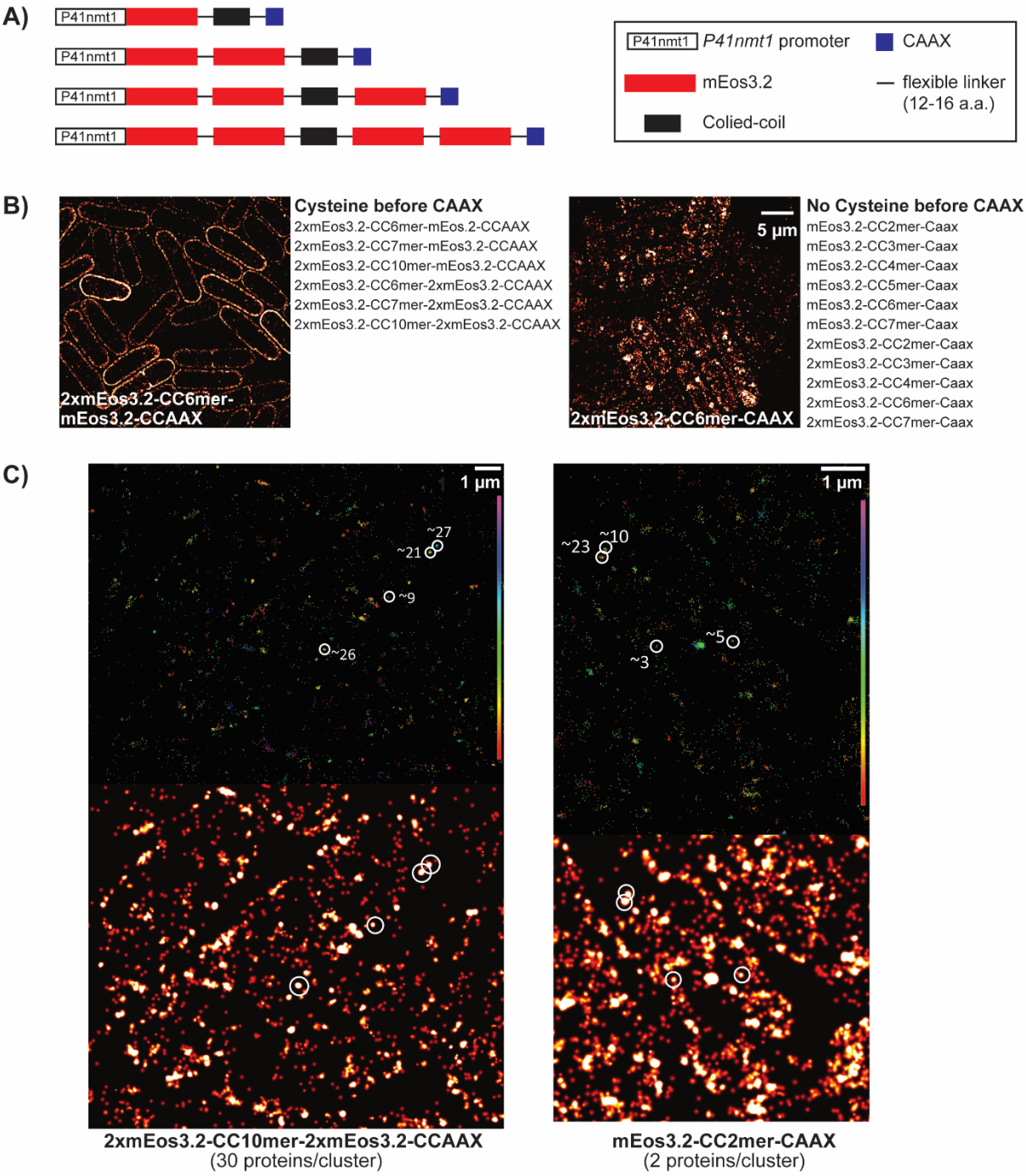

Figure 6.6: Coiled-coli peptides as internal calibration standard for SMLM in fission yeast cells

(A) DNA sequences encoding P41nmt1 promoter, the mEos3.2 FP, coiled-coil peptides, and CAAX sequence were inserted into the Leu locus of fission yeast genome. (B) 2D-SMLM images of fixed fission yeast cells expressing 2xmEos3.2-CC6mer-2xmEos3.2-CCAAX (n= 24) and expressing 2xmEos3.2-CC6mer-CAAX (n= 12). The cysteine residue before CAAX sequence is required for correct anchoring of the fusion proteins to the plasma membrane. The

strains with or without cysteine residue before CAAX-sequence were listed accordingly. The cells were grown in EMM5S for 24 hours for expression. (C) 2D-SMLM images of fixed fission yeast cells expressing 2xmEos3.2-CC10mer-2xmEos3.2-CCAAX (n= 30) and expressing 2xmEos3.2-CC6mer-CAAX (n= 2). The cells were grown in EMM5S for 24 hours for expression. The localizations in the SMLM images were color-coded based the time the localization appeared during image acquisition with red being the earliest and magenta being the latest (top panels). To aid the visualization of the 2D histogram image of 5-nm pixels, the images were convolved with a 2D Gaussian kernel of σ = 1.5*localization error in the x direction (bottom panels). The single clusters were manually picked (white circles) and the number of localizations of each cluster were also manually counted.

6.3 Future work

Based on the preliminary data, the monomeric and tandem dimeric mEos3.2, the coiled-coil oligomers, and the GEMs appear to be promising internal calibration standards for counting molecules with SMLM in fixed *S. pombe* cells. However, optimization and more work are still needed to establish the robustness and reproducibility of the standards. First, the expression level of the calibration standards need to be optimized through thiamine titration to suppress the expression from the *P41nmt1* promoter (Nakamura, Arai, Takebe, & Masuda, 2011). Expressing the calibration standard proteins at lower levels will prevent the higher-order clustering of the single clusters and increase the fraction of single clusters. Second, the imaging conditions, laser intensity and frame rate, need to be optimized to ensure the best signal-to-noise ratio for more precise localization of the individual molecules. Third, the parameters for finding the clusters need to be optimized based on the known structures. Once these optimizations are done, one can measure the number of localizations per cluster of the calibration standards and generate the calibration curve spanning across a wide range of molecules numbers from 1 to 120. One can use the calibration curve to count molecules in diffraction-limited subcellular structures, such as the cytokinesis nodes (Laplante et al., 2016).

Plasmid	Genotype	Source
pHMS009/SDB056	pFA6a mEos3.2:KanMX6	C. Laplante (NC State)
pHMS010	pFA6a NatMX6 p41nmt1 mEos3.2-CAAX	this study
pHMS011	pFA6a NatMX6 p41nmt1 2xmEos3.2-CAAX	this study
pHMS028	pJK148-P41nmt1-mEos3.2-FtnA-ADH1Term	this study
pHMS029	pJK148-P41nmt1-AqLS-mEos3.2-ADH1Term	this study
pHMS030	pJK148-P41nmt1-pfv-mEos3.2-ADH1Term	this study
pHMS031	pJK148-P41nmt1-Vuldi-mEos3.2-ADH1Term	this study
pHMS032	pJK148-P41nmt1-mEos3.2-GlnA-ADH1Term	this study
pHMS040	pJK148-P3nmt1-mEos3.2-FtnA-ADH1Term	this study
pHMS041	pJK148-P3nmt1-mEos3.2-GlnA-ADH1Term	this study
pHMS042	pFA6a NatMX6 p41nmt1-mEos3.2-CC2mer(1ZIK)-CAAX-ADHTerm1	this study
pHMS043	pFA6a NatMX6 p41nmt1-mEos3.2-CC3mer(1COI)-CAAX-ADHTerm1	this study
pHMS044	pFA6a NatMX6 p41nmt1-mEos3.2-CC4mer(3R4A)-CAAX-ADHTerm1	this study
pHMS045	pFA6a NatMX6 p41nmt1-mEos3.2-CC5mer(1FBM)-CAAX-ADHTerm1	this study
pHMS046	pFA6a NatMX6 p41nmt1-mEos3.2-CC6mer(3R3K)-CAAX-ADHTerm1	this study
pHMS047	pFA6a NatMX6 p41nmt1-mEos3.2-CC7mer(2HY6)-CAAX-ADHTerm1	this study
pHMS048	pFA6a NatMX6 p41nmt1-mEos3.2-CC10mer(4JPN)-CAAX-ADHTerm1	this study
pHMS049	pFA6a NatMX6 p41nmt1-2xmEos3.2-CC2mer(1ZIK)-CAAX-ADHTerm1	this study
pHMS050	pFA6a NatMX6 p41nmt1-2xmEos3.2-CC3mer(1COI)-CAAX-ADHTerm1	this study
pHMS051	pFA6a NatMX6 p41nmt1-2xmEos3.2-CC4mer(3R4A)-CAAX-ADHTerm1	this study
pHMS052	pFA6a NatMX6 p41nmt1-2xmEos3.2-CC5mer(1FBM)-CAAX-ADHTerm1	this study
pHMS053	pFA6a NatMX6 p41nmt1-2xmEos3.2-CC6mer(3R3K)-CAAX-ADHTerm1	this study
pHMS054	pFA6a NatMX6 p41nmt1-2xmEos3.2-CC7mer(2HY6)-CAAX-ADHTerm1	this study
pHMS055	pFA6a NatMX6 p41nmt1-2xmEos3.2-CC10mer(4JPN)-CAAX-ADHTerm1	this study
pHMS056	pFA6a NatMX6 p41nmt1-2xmEos3.2-CC6mer(3R3K)-mEos3.2-CAAX-ADHTerm1	this study
pHMS057	pFA6a NatMX6 p41nmt1-2xmEos3.2-CC7mer(2HY6)-mEos3.2-CAAX-ADHTerm1	this study

pHMS058	pFA6a NatMX6 p41nmt1-2xmEos3.2-CC10mer(4JPN)-mEos3.2-CAAX-ADHTerm1	this study

Table 6.1 Plasmids used in this study

Strain	Genotype	Source
sHMS037	*h+ nup85-mEos3.2::KanR ade6-M216 his3-D1 leu1-32 ura4-D18*	this study
sHMS044	*nup85-mEos3.2::KanR cdc25-22 ade6-M210 his3-D1 leu1-32 ura4-D18*	this study
sHMS039	*h+ Leu1::Nat:P41nmt1 mEos3.2-Caax ade6-M216 his3-D1 leu1-32 ura4-D18*	this study
sHMS045	*h+ Leu1::Nat:P41nmt1 2xmEos3.2-Caax ade6-M216 his3-D1 leu1-32 ura4-D18*	this study
sHMS061/SDP016	*h- ade6-M210 leu1-32 ura4-Δ18*	Sam Dundon
sHMS062/SDP017	*h+ ade6-M216 his3-Δ1 leu1-32 ura4-Δ18*	Sam Dundon
sHMS065	*h- Leu1::Leu1+:P41nmt1 mEos3.2-FtnA-ADH1term ade6-M216 his3-D1 leu1-32 ura4-D18*	this study
sHMS066	*h+ Leu1::Leu1+:P41nmt1 mEos3.2-FtnA-ADH1term ade6-M216 his3-D1 leu1-32 ura4-D18*	this study
sHMS067	*h- Leu1::Leu1+:P41nmt1 pfv-mEos3.2-ADH1term ade6-M216 his3-D1 leu1-32 ura4-D18*	this study
sHMS068	*h+ Leu1::Leu1+:P41nmt1 pfv-mEos3.2-ADH1term ade6-M216 his3-D1 leu1-32 ura4-D18*	this study
sHMS069	*h- Leu1::Leu1+:P41nmt1 Vuldi-mEos3.2-ADH1term ade6-M216 his3-D1 leu1-32 ura4-D18*	this study
sHMS070	*h+ Leu1::Leu1+:P41nmt1 Vuldi-mEos3.2-ADH1term ade6-M216 his3-D1 leu1-32 ura4-D18*	this study
sHMS071	*h- Leu1::Leu1+:P41nmt1 AqLS-mEos3.2-ADH1term ade6-M216 his3-D1 leu1-32 ura4-D18*	this study
sHMS072	*h+ Leu1::Leu1+:P41nmt1 AqLS-mEos3.2-ADH1term ade6-M216 his3-D1 leu1-32 ura4-D18*	this study
sHMS073	*h- Leu1::Leu1+:P41nmt1 mEos3.2-GlnA-ADH1term ade6-M216 his3-D1 leu1-32 ura4-D18*	this study
sHMS074	*h+ Leu1::Leu1+:P41nmt1 mEos3.2-GlnA-ADH1term ade6-M216 his3-D1 leu1-32 ura4-D18*	this study
sHMS091	*h- Leu1::Leu1+:P3nmt1 mEos3.2-FtnA-ADH1term ade6-M216 his3-D1 leu1-32 ura4-D18*	this study
sHMS092	*Leu1::Leu1+:P4nmt1 mEos3.2-CC2mer(81)-Caax ade6-M216 his3-D1 leu1-32 ura4-D18*	this study
sHMS093	*Leu1::Leu1+:P4nmt1 mEos3.2-CC3mer(82)-Caax ade6-M216 his3-D1 leu1-32 ura4-D18*	this study
sHMS094	*Leu1::Leu1+:P4nmt1 mEos3.2-CC4mer(83)-Caax ade6-M216 his3-D1 leu1-32 ura4-D18*	this study
sHMS095	*Leu1::Leu1+:P4nmt1 mEos3.2-CC5mer(84)-Caax ade6-M216 his3-D1 leu1-32 ura4-D18*	this study
sHMS096	*Leu1::Leu1+:P4nmt1 mEos3.2-CC6mer(85)-Caax ade6-M216 his3-D1 leu1-32 ura4-D18*	this study
sHMS097	*Leu1::Leu1+:P4nmt1 mEos3.2-CC7mer(86)-Caax ade6-M216 his3-D1 leu1-32 ura4-D18*	this study
sHMS099	*Leu1::Leu1+:P4nmt1 2xmEos3.2-CC2mer(81)-Caax ade6-M216 his3-D1 leu1-32 ura4-D18*	this study

sHMS100	*Leu1::Leu1+:P4nmt1 2xmEos3.2-CC3mer(82)-Caax ade6-M216 his3-D1 leu1-32 ura4-D18*	this study
sHMS101	*Leu1::Leu1+:P4nmt1 2xmEos3.2-CC4mer(83)-Caax ade6-M216 his3-D1 leu1-32 ura4-D18*	this study
sHMS102	*Leu1::Leu1+:P4nmt1 2xmEos3.2-CC5mer(84)-Caax ade6-M216 his3-D1 leu1-32 ura4-D18*	this study
sHMS103	*Leu1::Leu1+:P4nmt1 2xmEos3.2-CC6mer(85)-Caax ade6-M216 his3-D1 leu1-32 ura4-D18*	this study
sHMS104	*Leu1::Leu1+:P4nmt1 2xmEos3.2-CC7mer(86)-Caax ade6-M216 his3-D1 leu1-32 ura4-D18*	this study
sHMS106	*Leu1::Leu1+:P4nmt1 2xmEos3.2-CC6mer(85)-mEos3.2-Caax ade6-M216 his3-D1 leu1-32 ura4-D18*	this study
sHMS107	*Leu1::Leu1+:P4nmt1 2xmEos3.2-CC7mer(86)-mEos3.2-Caax ade6-M216 his3-D1 leu1-32 ura4-D18*	this study
sHMS108	*Leu1::Leu1+:P4nmt1 2xmEos3.2-CC10mer(87)-mEos3.2-Caax ade6-M216 his3-D1 leu1-32 ura4-D18*	this study
sHMS110	*Leu1::Leu1+:P4nmt1 2xmEos3.2-CC7mer(86)-2xmEos3.2-Caax ade6-M216 his3-D1 leu1-32 ura4-D18*	this study

Table 6.2 *S. pombe* strains used in this study

References

Akamatsu, M., Lin, Y., Bewersdorf, J., & Pollard, T. D. (2017). Analysis of interphase node proteins in fission yeast by quantitative and superresolution fluorescence microscopy. *Mol Biol Cell, 28*(23), 3203-3214. doi: 10.1091/mbc.E16-07-0522

Annibale, P., Vanni, S., Scarselli, M., Rothlisberger, U., & Radenovic, A. (2011). Quantitative photo activated localization microscopy: unraveling the effects of photoblinking. *PLoS One, 6*(7), e22678. doi: 10.1371/journal.pone.0022678

Avilov, S., Berardozzi, R., Gunewardene, M. S., Adam, V., Hess, S. T., & Bourgeois, D. (2014). In cellulo evaluation of phototransformation quantum yields in fluorescent proteins used as markers for single-molecule localization microscopy. *PLoS One, 9*(6), e98362. doi: 10.1371/journal.pone.0098362

Baddeley, D., & Bewersdorf, J. (2017). Biological Insight from Super-Resolution Microscopy: What We Can Learn from Localization-Based Images. *Annu Rev Biochem*. doi: 10.1146/annurev-biochem-060815-014801

Baddeley, D., Jayasinghe, I. D., Cremer, C., Cannell, M. B., & Soeller, C. (2009). Light-induced dark states of organic fluochromes enable 30 nm resolution imaging in standard media. *Biophys J, 96*(2), L22-24. doi: 10.1016/j.bpj.2008.11.002

Bähler, J., Wu, J.-Q., Longtine, M. S., Shah, N. G., McKenzie Iii, A., Steever, A. B., . . . Pringle, J. R. (1998). Heterologous modules for efficient and versatile PCR-based gene targeting inSchizosaccharomyces pombe. *Yeast, 14*(10), 943-951. doi: 10.1002/(sici)1097-0061(199807)14:10<943::aid-yea292>3.0.co;2-y

Baldering, T. N., Dietz, M. S., Gatterdam, K., Karathanasis, C., Wieneke, R., Tampe, R., & Heilemann, M. (2019). Synthetic and genetic dimers as quantification ruler for single-molecule counting with PALM. *Mol Biol Cell, 30*(12), 1369-1376. doi: 10.1091/mbc.E18-10-0661

Betzig, E., Patterson, G. H., Sougrat, R., Lindwasser, O. W., Olenych, S., Bonifacino, J. S., . . . Hess, H. F. (2006). Imaging intracellular fluorescent proteins at nanometer resolution. *Science, 313*(5793), 1642-1645. doi: 10.1126/science.1127344

Coffman, V. C., & Wu, J. Q. (2012). Counting protein molecules using quantitative fluorescence microscopy. *Trends Biochem Sci, 37*(11), 499-506. doi: 10.1016/j.tibs.2012.08.002

De Zitter, E., Ridard, J., Thedie, D., Adam, V., Levy, B., Byrdin, M., . . . Bourgeois, D. (2020). Mechanistic Investigations of Green mEos4b Reveal a Dynamic Long-Lived Dark State. *J Am Chem Soc, 142*(25), 10978-10988. doi: 10.1021/jacs.0c01880

De Zitter, E., Thedie, D., Monkemoller, V., Hugelier, S., Beaudouin, J., Adam, V., . . . Bourgeois, D. (2019). Mechanistic investigation of mEos4b reveals a strategy to reduce track interruptions in sptPALM. *Nat Methods, 16*(8), 707-710. doi: 10.1038/s41592-019-0462-3

Delarue, M., Brittingham, G., Pfeffer, S., Surovtsev, I., Pinglay, S., Kennedy, K., . . . Poterewicz, G. (2018). mTORC1 controls phase separation and the biophysical properties of the cytoplasm by tuning crowding. *Cell, 174*(2), 338-349. e320.

Deschout, H., Cella Zanacchi, F., Mlodzianoski, M., Diaspro, A., Bewersdorf, J., Hess, S. T., & Braeckmans, K. (2014). Precisely and accurately localizing single emitters in fluorescence microscopy. *Nat Methods, 11*(3), 253-266. doi: 10.1038/nmeth.2843

Durisic, N., Laparra-Cuervo, L., Sandoval-Alvarez, A., Borbely, J. S., & Lakadamyali, M. (2014). Single-molecule evaluation of fluorescent protein photoactivation efficiency using an in vivo nanotemplate. *Nat Methods, 11*(2), 156-162. doi: 10.1038/nmeth.2784

Ehmann, N., van de Linde, S., Alon, A., Ljaschenko, D., Keung, X. Z., Holm, T., . . . Kittel, R. J. (2014). Quantitative super-resolution imaging of Bruchpilot distinguishes active zone states. *Nat Commun, 5*, 4650. doi: 10.1038/ncomms5650

Endesfelder, U., Malkusch, S., Flottmann, B., Mondry, J., Liguzinski, P., Verveer, P. J., & Heilemann, M. (2011). Chemically induced photoswitching of fluorescent probes--a general concept for super-resolution microscopy. *Molecules, 16*(4), 3106-3118. doi: 10.3390/molecules16043106

Finan, K., Raulf, A., & Heilemann, M. (2015). A set of homo-oligomeric standards allows accurate protein counting. *Angew Chem Int Ed Engl, 54*(41), 12049-12052. doi: 10.1002/anie.201505664

Folling, J., Bossi, M., Bock, H., Medda, R., Wurm, C. A., Hein, B., . . . Hell, S. W. (2008). Fluorescence nanoscopy by ground-state depletion and single-molecule return. *Nat Methods, 5*(11), 943-945. doi: 10.1038/nmeth.1257

Fricke, F., Beaudouin, J., Eils, R., & Heilemann, M. (2015). One, two or three? Probing the stoichiometry of membrane proteins by single-molecule localization microscopy. *Sci Rep, 5*, 14072. doi: 10.1038/srep14072

Ganguly, S., Clayton, A. H., & Chattopadhyay, A. (2011). Fixation alters fluorescence lifetime and anisotropy of cells expressing EYFP-tagged serotonin1A receptor. *Biochem Biophys Res Commun, 405*(2), 234-237. doi: 10.1016/j.bbrc.2011.01.016

Gonzalez, L., Jr., Woolfson, D. N., & Alber, T. (1996). Buried polar residues and structural specificity in the GCN4 leucine zipper. *Nat Struct Biol, 3*(12), 1011-1018. doi: 10.1038/nsb1296-1011

Greenbaum, L., Rothmann, C., Lavie, R., & Malik, Z. (2000). Green fluorescent protein photobleaching: a model for protein damage by endogenous and exogenous singlet oxygen. *Biological chemistry, 381*(12), 1251-1258.

Guo, Y., Bozic, D., Malashkevich, V. N., Kammerer, R. A., Schulthess, T., & Engel, J. (1998). All-trans retinol, vitamin D and other hydrophobic compounds bind in the axial pore of the five-stranded coiled-coil domain of cartilage oligomeric matrix protein. *EMBO J, 17*(18), 5265-5272. doi: 10.1093/emboj/17.18.5265

Hancock, J. F., Cadwallader, K., Paterson, H., & Marshall, C. J. (1991). A CAAX or a CAAL motif and a second signal are sufficient for plasma membrane targeting of ras proteins. *EMBO J, 10*(13), 4033-4039.

Heilemann, M., van de Linde, S., Schuttpelz, M., Kasper, R., Seefeldt, B., Mukherjee, A., . . . Sauer, M. (2008). Subdiffraction-resolution fluorescence imaging with conventional fluorescent probes. *Angew Chem Int Ed Engl, 47*(33), 6172-6176. doi: 10.1002/anie.200802376

Hell, S. W. (2007). Far-field optical nanoscopy. *Science, 316*(5828), 1153-1158.

Hell, S. W. (2015). Nanoscopy with Focused Light (Nobel Lecture). *Angew Chem Int Ed Engl, 54*(28), 8054-8066. doi: 10.1002/anie.201504181

Hell, S. W., Dyba, M., & Jakobs, S. (2004). Concepts for nanoscale resolution in fluorescence microscopy. *Curr Opin Neurobiol, 14*(5), 599-609. doi: 10.1016/j.conb.2004.08.015

Hell, S. W., & Wichmann, J. (1994). Breaking the Diffraction Resolution Limit by Stimulated-Emission - Stimulated-Emission-Depletion Fluorescence Microscopy. *Optics Letters, 19*(11), 780-782.

Hess, S. T., Girirajan, T. P. K., & Mason, M. D. (2006). Ultra-high resolution imaging by fluorescence photoactivation localization microscopy. *Biophysical Journal, 91*(11), 4258-4272. doi: 10.1529/biophysj.106.091116

Huang, B., Bates, M., & Zhuang, X. (2009). Super-resolution fluorescence microscopy. *Annu Rev Biochem, 78*, 993-1016. doi: 10.1146/annurev.biochem.77.061906.092014

Hummer, G., Fricke, F., & Heilemann, M. (2016). Model-independent counting of molecules in single-molecule localization microscopy. *Mol Biol Cell, 27*(22), 3637-3644. doi: 10.1091/mbc.E16-07-0525

Jungmann, R., Avendano, M. S., Dai, M., Woehrstein, J. B., Agasti, S. S., Feiger, Z., . . . Yin, P. (2016). Quantitative super-resolution imaging with qPAINT. *Nat Methods, 13*(5), 439-442. doi: 10.1038/nmeth.3804

Karathanasis, C., Medler, J., Fricke, F., Smith, S., Malkusch, S., Widera, D., . . . Heilemann, M. (2020). Single-molecule imaging reveals the oligomeric state of functional TNFalpha-induced plasma membrane TNFR1 clusters in cells. *Sci Signal, 13*(614). doi: 10.1126/scisignal.aax5647

Klar, T. A., & Hell, S. W. (1999). Subdiffraction resolution in far-field fluorescence microscopy. *Optics Letters, 24*(14), 954-956.

Krueger, T. D., Tang, L., Zhu, L., Breen, I. L., Wachter, R. M., & Fang, C. (2020). Dual Illumination Enhances Transformation of an Engineered Green-to-Red Photoconvertible Fluorescent Protein. *Angew Chem Int Ed Engl, 59*(4), 1644-1652. doi: 10.1002/anie.201911379

Laplante, C., Huang, F., Tebbs, I. R., Bewersdorf, J., & Pollard, T. D. (2016). Molecular organization of cytokinesis nodes and contractile rings by super-resolution fluorescence microscopy of live fission yeast. *Proc Natl Acad Sci U S A*. doi: 10.1073/pnas.1608252113

Lee, S. H., Shin, J. Y., Lee, A., & Bustamante, C. (2012). Counting single photoactivatable fluorescent molecules by photoactivated localization microscopy (PALM). *Proc Natl Acad Sci U S A, 109*(43), 17436-17441. doi: 10.1073/pnas.1215175109

Lemmer, P., Gunkel, M., Baddeley, D., Kaufmann, R., Urich, A., Weiland, Y., . . . Cremer, C. (2008). SPDM: light microscopy with single-molecule resolution at the nanoscale. *Applied Physics B, 93*(1), 1-12. doi: 10.1007/s00340-008-3152-x

Lin, R., Clowsley, A. H., Jayasinghe, I. D., Baddeley, D., & Soeller, C. (2017). Algorithmic corrections for localization microscopy with sCMOS cameras - characterisation of a computationally efficient localization approach. *Opt Express, 25*(10), 11701-11716. doi: 10.1364/OE.25.011701

Lin, Y., Long, J. J., Huang, F., Duim, W. C., Kirschbaum, S., Zhang, Y., . . . Bewersdorf, J. (2015). Quantifying and optimizing single-molecule switching nanoscopy at high speeds. *PLoS One, 10*(5), e0128135. doi: 10.1371/journal.pone.0128135

Lippincott-Schwartz, J., & Patterson, G. H. (2009). Photoactivatable fluorescent proteins for diffraction-limited and super-resolution imaging. *Trends in cell biology, 19*(11), 555-565.

Liu, J., Zheng, Q., Deng, Y., Cheng, C. S., Kallenbach, N. R., & Lu, M. (2006). A seven-helix coiled coil. *Proc Natl Acad Sci U S A, 103*(42), 15457-15462. doi: 10.1073/pnas.0604871103

Los, G., Darzins, A., Karassina, N., Zimprich, C., Learish, R., McDougall, M., . . . Vidugiris, G. (2005). HaloTag™ Interchangeable labeling technology for cell imaging and protein capture. *Cell Notes, 11*, 2-6.

Malashkevich, V. N., Kammerer, R. A., Efimov, V. P., Schulthess, T., & Engel, J. (1996). The crystal structure of a five-stranded coiled coil in COMP: a prototype ion channel? *Science, 274*(5288), 761-765. doi: 10.1126/science.274.5288.761

McKinney, S. A., Murphy, C. S., Hazelwood, K. L., Davidson, M. W., & Looger, L. L. (2009). A bright and photostable photoconvertible fluorescent protein. *Nat Methods, 6*(2), 131-133. doi: 10.1038/nmeth.1296

Mclean, A. J., Mcgarvey, D. J., Truscott, T. G., Lambert, C. R., & Land, E. J. (1990). Effect of Oxygen-Enhanced Intersystem Crossing on the Observed Efficiency of Formation of Singlet Oxygen. *Journal of the Chemical Society-Faraday Transactions, 86*(18), 3075-3080. doi: DOI 10.1039/ft9908603075

Nakamura, Y., Arai, A., Takebe, Y., & Masuda, M. (2011). A chemical compound for controlled expression of nmt1-driven gene in the fission yeast Schizosaccharomyces pombe. *Analytical biochemistry, 412*(2), 159-164.

Nienhaus, K., & Nienhaus, G. U. (2014). Fluorescent proteins for live-cell imaging with super-resolution. *Chemical Society Reviews, 43*(4), 1088-1106.

Nienhaus, K., Nienhaus, G. U., Wiedenmann, J., & Nar, H. (2005). Structural basis for photo-induced protein cleavage and green-to-red conversion of fluorescent protein EosFP. *Proc Natl Acad Sci U S A, 102*(26), 9156-9159. doi: 10.1073/pnas.0501874102

Nieuwenhuizen, R. P., Bates, M., Szymborska, A., Lidke, K. A., Rieger, B., & Stallinga, S. (2015). Quantitative localization microscopy: effects of photophysics and labeling stoichiometry. *PLoS One, 10*(5), e0127989. doi: 10.1371/journal.pone.0127989

Nieuwenhuizen, R. P., Lidke, K. A., Bates, M., Puig, D. L., Grunwald, D., Stallinga, S., & Rieger, B. (2013). Measuring image resolution in optical nanoscopy. *Nat Methods, 10*(6), 557-562. doi: 10.1038/nmeth.2448

O'Shea, E. K., Klemm, J. D., Kim, P. S., & Alber, T. (1991). X-ray structure of the GCN4 leucine zipper, a two-stranded, parallel coiled coil. *Science, 254*(5031), 539-544. doi: 10.1126/science.1948029

Ogihara, N. L., Weiss, M. S., Degrado, W. F., & Eisenberg, D. (1997). The crystal structure of the designed trimeric coiled coil coil-VaLd: implications for engineering crystals and supramolecular assemblies. *Protein Sci, 6*(1), 80-88. doi: 10.1002/pro.5560060109

Paez-Segala, M. G., Sun, M. G., Shtengel, G., Viswanathan, S., Baird, M. A., Macklin, J. J., . . . Looger, L. L. (2015). Fixation-resistant photoactivatable fluorescent proteins for CLEM. *Nat Methods, 12*(3), 215-218, 214 p following 218. doi: 10.1038/nmeth.3225

Puchner, E. M., Walter, J. M., Kasper, R., Huang, B., & Lim, W. A. (2013). Counting molecules in single organelles with superresolution microscopy allows tracking of the endosome maturation trajectory. *Proc Natl Acad Sci U S A, 110*(40), 16015-16020. doi: 10.1073/pnas.1309676110

Rollins, G. C., Shin, J. Y., Bustamante, C., & Presse, S. (2015). Stochastic approach to the molecular counting problem in superresolution microscopy. *Proc Natl Acad Sci U S A, 112*(2), E110-118. doi: 10.1073/pnas.1408071112

Rust, M. J., Bates, M., & Zhuang, X. (2006). Sub-diffraction-limit imaging by stochastic optical reconstruction microscopy (STORM). *Nat Methods, 3*(10), 793-795. doi: 10.1038/nmeth929

Schindelin, J., Arganda-Carreras, I., Frise, E., Kaynig, V., Longair, M., Pietzsch, T., . . . Cardona, A. (2012). Fiji: an open-source platform for biological-image analysis. *Nat Methods, 9*(7), 676-682. doi: 10.1038/nmeth.2019

Sengupta, P., Jovanovic-Talisman, T., Skoko, D., Renz, M., Veatch, S. L., & Lippincott-Schwartz, J. (2011). Probing protein heterogeneity in the plasma membrane using PALM and pair correlation analysis. *Nat Methods, 8*(11), 969-975. doi: 10.1038/nmeth.1704

Shroff, H., Galbraith, C. G., Galbraith, J. A., White, H., Gillette, J., Olenych, S., . . . Betzig, E. (2007). Dual-color superresolution imaging of genetically expressed probes within individual adhesion complexes. *Proceedings of the National Academy of Sciences of the United States of America, 104*(51), 20308-20313. doi: 10.1073/pnas.0710517105

Sigal, Y. M., Zhou, R., & Zhuang, X. (2018). Visualizing and discovering cellular structures with super-resolution microscopy. *Science, 361*(6405), 880-887.

Solovyev, I. D., Gavshina, A. V., & Savitsky, A. P. (2019). Novel Phototransformable Fluorescent Protein SAASoti with Unique Photochemical Properties. *Int J Mol Sci, 20*(14). doi: 10.3390/ijms20143399

Stagge, F., Mitronova, G. Y., Belov, V. N., Wurm, C. A., & Jakobs, S. (2013). SNAP-, CLIP- and Halo-tag labelling of budding yeast cells. *PLoS One, 8*(10), e78745. doi: 10.1371/journal.pone.0078745

Sun, L., Young, L. N., Zhang, X., Boudko, S. P., Fokine, A., Zbornik, E., . . . Fane, B. A. (2014). Icosahedral bacteriophage PhiX174 forms a tail for DNA transport during infection. *Nature, 505*(7483), 432-435. doi: 10.1038/nature12816

Thedie, D., Berardozzi, R., Adam, V., & Bourgeois, D. (2017). Photoswitching of Green mEos2 by Intense 561 nm Light Perturbs Efficient Green-to-Red Photoconversion in Localization Microscopy. *J Phys Chem Lett, 8*(18), 4424-4430. doi: 10.1021/acs.jpclett.7b01701

Thevathasan, J. V., Kahnwald, M., Cieslinski, K., Hoess, P., Peneti, S. K., Reitberger, M., . . . Ries, J. (2019). Nuclear pores as versatile reference standards for quantitative superresolution microscopy. *Nat Methods, 16*(10), 1045-1053. doi: 10.1038/s41592-019-0574-9

Turkowyd, B., Balinovic, A., Virant, D., Carnero, H. G. G., Caldana, F., Endesfelder, M., . . . Endesfelder, U. (2017). A General Mechanism of Photoconversion of Green-to-Red Fluorescent Proteins Based on Blue and Infrared Light Reduces Phototoxicity in Live-Cell Single-Molecule Imaging. *Angewandte Chemie-International Edition, 56*(38), 11634-11639. doi: 10.1002/anie.201702870

Wang, S., Moffitt, J. R., Dempsey, G. T., Xie, X. S., & Zhuang, X. (2014). Characterization and development of photoactivatable fluorescent proteins for single-molecule-based superresolution imaging. *Proc Natl Acad Sci U S A, 111*(23), 8452-8457. doi: 10.1073/pnas.1406593111

Wiedenmann, J., Ivanchenko, S., Oswald, F., Schmitt, F., Rocker, C., Salih, A., . . . Nienhaus, G. U. (2004). EosFP, a fluorescent marker protein with UV-inducible green-to-red fluorescence conversion. *Proc Natl Acad Sci U S A, 101*(45), 15905-15910. doi: 10.1073/pnas.0403668101

Wu, J. Q., & Pollard, T. D. (2005). Counting cytokinesis proteins globally and locally in fission yeast. *Science, 310*(5746), 310-314. doi: 10.1126/science.1113230

Xu, K., Zhong, G., & Zhuang, X. (2013). Actin, spectrin, and associated proteins form a periodic cytoskeletal structure in axons. *Science, 339*(6118), 452-456.

Xu, X. W., Ester, M., Kriegel, H. P., & Sander, J. (1998). A distribution-based clustering algorithm for mining in large spatial databases. *14th International Conference on Data Engineering, Proceedings*, 324-331. doi: Doi 10.1109/Icde.1998.655795

Zaccai, N. R., Chi, B., Thomson, A. R., Boyle, A. L., Bartlett, G. J., Bruning, M., . . . Woolfson, D. N. (2011). A de novo peptide hexamer with a mutable channel. *Nat Chem Biol, 7*(12), 935-941. doi: 10.1038/nchembio.692

Zanacchi, F. C., Manzo, C., Alvarez, A. S., Derr, N. D., Garcia-Parajo, M. F., & Lakadamyali, M. (2017). A DNA origami platform for quantifying protein copy number in super-resolution. *Nat Methods, 14*(8), 789-792. doi: 10.1038/nmeth.4342

Zhang, M., Chang, H., Zhang, Y., Yu, J., Wu, L., Ji, W., . . . Xu, T. (2012). Rational design of true monomeric and bright photoactivatable fluorescent proteins. *Nat Methods, 9*(7), 727-729. doi: 10.1038/nmeth.2021

Zhang, Y., Lara-Tejero, M., Bewersdorf, J., & Galan, J. E. (2017). Visualization and characterization of individual type III protein secretion machines in live bacteria. *Proc Natl Acad Sci U S A, 114*(23), 6098-6103. doi: 10.1073/pnas.1705823114

Zhang, Y., Shen, H., Liu, H., Feng, H., Liu, Y., Zhu, X., & Liu, X. (2017). Arp2/3 complex controls T cell homeostasis by maintaining surface TCR levels via regulating TCR(+) endosome trafficking. *Sci Rep, 7*(1), 8952. doi: 10.1038/s41598-017-08357-4

Zimmerli, C. E., Allegretti, M., Rantos, V., Goetz, S. K., Obarska-Kosinska, A., Zagoriy, I., . . . Beck, M. (2020). Nuclear pores constrict upon energy depletion. *bioRxiv*. doi: 10.1101/2020.07.30.228585